

A NOVEL OXIMETER

By

Paul Irvin Rodmell

SUBMITTED IN PARTIAL FULFILLMENT OF THE
REQUIREMENTS FOR THE DEGREE OF
DOCTOR OF PHILOSOPHY
AT
UNIVERSITY OF NOTTINGHAM
NOTTINGHAM, ENGLAND
SEPTEMBER 2005

© Copyright by Paul Irvin Rodmell, 2005

UNIVERSITY OF NOTTINGHAM
DEPARTMENT OF
ELECTRICAL AND ELECTRONIC ENGINEERING

The undersigned hereby certify that they have read and recommend to the Faculty of Faculty of Engineering for acceptance a thesis entitled “**A Novel Oximeter**” by **Paul Irvin Rodmell** in partial fulfillment of the requirements for the degree of **Doctor of Philosophy**.

Dated: September 2005

External Examiner: _____
Dr Deric Jones

Research Supervisor: _____
Dr John Crowe

Examining Committee: _____
Dr Steve Morgan

UNIVERSITY OF NOTTINGHAM

Date: **September 2005**

Author: **Paul Irvin Rodmell**

Title: **A Novel Oximeter**

Department: **Electrical and Electronic Engineering**

Degree: **Ph.D.**

Year: **2005**

Permission is herewith granted to University of Nottingham to circulate and to have copied for non-commercial purposes, at its discretion, the above title upon the request of individuals or institutions.

Signature of Author

THE AUTHOR RESERVES OTHER PUBLICATION RIGHTS, AND NEITHER THE THESIS NOR EXTENSIVE EXTRACTS FROM IT MAY BE PRINTED OR OTHERWISE REPRODUCED WITHOUT THE AUTHOR'S WRITTEN PERMISSION.

THE AUTHOR ATTESTS THAT PERMISSION HAS BEEN OBTAINED FOR THE USE OF ANY COPYRIGHTED MATERIAL APPEARING IN THIS THESIS (OTHER THAN BRIEF EXCERPTS REQUIRING ONLY PROPER ACKNOWLEDGEMENT IN SCHOLARLY WRITING) AND THAT ALL SUCH USE IS CLEARLY ACKNOWLEDGED.

Jules.

Table of Contents

Table of Contents	v
List of Figures	viii
Abstract	xii
ACKNOWLEDGEMENTS	xiv
1 Introduction	1
1.1 Oximetry	1
1.1.1 Pulse Oximetry	4
1.1.2 Recent Developments	5
1.1.3 Summary	7
1.2 Introduction to Lambert-Beer Law based oximetry	8
1.2.1 Pulse oximetry	12
1.3 Oximetry from reflectance spectra	15
1.3.1 Introduction	15
1.3.2 Research by Lubbers et al	17
1.3.3 The attenuation v absorption transform	17
1.3.4 The effect of composite media	19
1.3.5 The Kubelka-Munk transform	19
1.3.6 Parabolic approximation to the transform	22
1.3.7 The effect of wavelength on the attenuation v absorption transform	22
1.4 Conclusion	24
2 Spectrophotometry in scattering media	25
2.1 Introduction	25
2.1.1 Absorption alone	26

2.1.2	Scattering alone	27
2.1.3	Scattering plus an absorber	30
2.2	Models used previously	33
2.3	Photon diffusion theory	35
2.4	The Power Law fit	36
2.4.1	Derivatives and Moments	38
2.5	Ratio of the first and second derivatives	43
2.5.1	Solving the differential equation	45
2.6	Comparing Models	47
2.6.1	Error and Parameter plots Lambert Beer plus offset	48
2.6.2	Error and Parameter plots Photon Diffusion Theory	50
2.6.3	Power Law fit	52
2.7	Conclusion	55
3	Oximetry using Power Law Transform	56
3.1	Introduction	56
3.1.1	The attenuation surface	57
3.1.2	The extinction spectra	57
3.1.3	Creating the attenuation spectra for a given oxygen saturation	59
3.1.4	Extracting the oxygen saturation from the spectra	60
3.2	Applying the method to the Power Law transform	65
3.2.1	Range and accuracy of fit	66
3.3	Extension to Three Species of Haemoglobin	70
3.3.1	Range and accuracy of fit using 3 species	72
3.3.2	Discussion	75
4	Exponential Model	76
4.1	A more general result	76
4.1.1	Error and Parameter plots general form	77
4.2	Adding a Linear Term	80
4.3	Scattering Variation with Wavelength	83
4.4	Model Results	83
4.4.1	Testing the Exponential transform with 3 species	85
4.5	Noise and Quantization Errors	88
4.5.1	The effects of Noise	88
4.5.2	The Effects of Quantisation	89
4.5.3	Bandwidth	90
4.5.4	Wavelength Interval	91
4.6	Conclusion	92

5	Experimental Confirmation	94
5.1	Introduction	94
5.2	Results using an Ocean Optics USB 2000	94
5.2.1	Early in vivo data	95
5.2.2	discussion	97
5.3	Hyperspectra Camera	97
5.3.1	Hyper-spectral cameras for in vivo work	99
5.4	Experimental configuration	103
5.5	The Provision scanning Hyper visual imaging camera	105
5.6	Results from Lab on 28/11/03 at AstraZeneca	108
5.6.1	Results and Discussion	116
5.7	Az Trial	117
5.8	Results and Discusion	121
6	Mathematics Underpinning the model	122
6.1	Introduction	122
6.2	Simplest case	122
6.3	The effect of the shape of the TPSF	126
6.4	The accuracy of the fitting equation	128
6.4.1	Discussion	133
6.5	An alternative approach to the dependency of A on μ_a	134
6.5.1	Fitting the power series	135
6.6	Conclusion	138
7	Discussion and Future Work	140
7.1	finding the Transform	140
7.2	The Hyper-spectral Camera	142
7.3	Further Work	143
	Bibliography	145

List of Figures

1.1	This Curve shows the relationship between SO_2 and the partial pressure of oxygen in the blood of a normal healthy adult, the partial pressure is the important parameter, however it cannot be measured, by non-invasive means.	3
1.2	Hemoglobin Extinction Curves	8
1.3	The pulsatile signal (exaggerated) from a pulse oximeter showing I' (dc+ac) and I (dc)	13
1.4	The transform from absorption to attenuation showing the required transform and the Lambert-Beer + offset approximation	18
1.5	(a) the fitting error and (b) the fitting parameters using the $a\mu_a + c$ approximation	23
2.1	The Scattering process 2D representation of the many paths. The illumination enters the sample centre left.	27
2.2	TPSF 10^8 photons incident on a 10mm thick sample having an effective scattering coefficient $\mu'_s(\lambda) = 1.25mm^{-1}$ ($\mu'_s(\lambda) = \mu_s(\lambda) \cdot (1 - g(\lambda))$)	28
2.3	light passes through a scattering media $\mu'_s = 1.25mm^{-1}$, then through an absorber $\mu_a = 0.03mm^{-1}$ resulting in the TPSF (far right)	30
2.4	Attenuation surface from Monte Carlo data 10^8 photons incident on a 10mm thick sample with μ_a in the range $0-5 mm^{-1}$ and μ'_s in the range $0 - 3.3 mm^{-1}$	32

2.5	Comparison of three approximations with Monte Carlo data, in transmission, with all transmitted photons detected for a slab of thickness 1cm	34
2.6	Attenuation and its first two derivatives wrt μ_a	37
2.7	Comparing the mean of the TPSF with $\frac{dA}{d\mu_a}$ using a Monte Carlo simulation of 10^8 photons incident on a 10mm sample	40
2.8	Comparing the Variance of the TPSF with $-\frac{d^2A}{d\mu_a^2}$ using a Monte Carlo simulation of 10^8 photons incident on a 10mm sample	42
2.9	(a) percentage error in fitting (error increases with μ'_s) and (b) fitting parameters, Lambert Beer plus offset fit using a Monte Carlo simulation. mm^{-1}	49
2.10	Fitting parameters, Photon Diffusion Theory fit using a Monte Carlo simulation 10^8 photons incident on a 10mm thick sample of tissue for 18 values from μ'_s 0.0743 to 1.6817mm^{-1}	51
2.11	Fitting parameters, Power Law fit using a Monte Carlo simulation 10^8 photons incident on a 10mm thick sample of tissue for 18 values from μ'_s 0.0743 to 1.6817mm^{-1}	53
2.12	Fitting parameters (expanded scale), Power Law fit using a Monte Carlo simulation.	54
3.1	The Attenuation Surface used to test oxygen saturation recovery $\mu_a = 0.01 - 0.3 \text{ mm}^{-1}$,	
3.2	The Attenuation Spectra, for 11 percentages of oxygen saturation, using the Surface Model	59
3.3	Extracting SO_2 using $a\mu_a + c$ top left - the modelled measured spectrum, top right the required transform (blue) and the Lambert-Ber Plus offset fir (red), bottom left - the transform, bottom right - the recovered spectra $\text{SO}_2 = 88\%$	64
3.4	Error in fit over the absorbtion range μ_a 0 - 0.3 mm^{-1} v scattering coefficient μ_s 0.0743 - 1.6817 mm^{-1}	66
3.5	Fitting parameters v scattering coefficient	67

3.6	Error in recovered SO ₂ v SO ₂ set-point	68
3.7	Fitting parameters v s SO ₂ set-point	69
3.8	Error in recovered SO ₂ and S _{CO} as SO ₂ is increased to 100 % while S _{CO} is decreased from 0 to 100 %	73
3.9	Fitting parameters v sSO ₂ set-point	74
4.1	The Error and fitting parameters for the fitting equation Attenuation = $ae^{-b\mu_a} - a_2e^{-b_2\mu}$ for $\mu_a = 0 - 6\text{mm}^{-1}$	78
4.2	The Error and fitting parameters for the fitting equation Attenuation = $ae^{-b\mu_a} - a_2e^{-b_2\mu}$ for $\mu_a = 0 - 0.33\text{mm}^{-1}$	79
4.3	Errors and parameters, for $\mu_a = 0 - 6\text{mm}^{-1}$ Attenuation = $ae^{-b\mu_a} - a_2e^{-b_2\mu_a} + c\mu_a + d$ ($\mu_a \text{ mm}^{-1}$ and $\mu'_a \text{ mm}^{-1}$) note the values of parameter a and d are di- vided by the scattering coefficient to demonstrate there dependance on scattering.	81
4.4	Errors and parameters, for $\mu_a = 0 - 0.33\text{mm}^{-1}$ Attenuation = $ae^{-b\mu_a} - a_2e^{-b_2\mu_a} + c\mu_a +$ ($\mu_a \text{ mm}^{-1}$ and $\mu'_a \text{ mm}^{-1}$) note the values of parameter a and d are di- vided by the scattering coefficient to demonstrate there dependance on scattering.	82
4.5	The Error and fitting parameters for S _{O₂} recovery, using the model, Attenuation = $ae^{-b\mu_a} - a_2e^{-b_2\mu_a} + c\mu_a + d\mu_a\lambda + e\lambda + f$	84
4.6	The Error and fitting parameters with SO ₂ and S _{CO}	86
4.7	Percentage error recovering SO ₂ v signal to noise ratio	88
4.8	Percentage error recovering SO ₂ v Quantisation	89
4.9	Percentage error recovering SO ₂ v Quantisation	91
5.1	Fits obtained from The Left Thumb and A right vein on the back of the Right Hand, λ (nm), $\mu_a \text{ mm}^{-1}$	96
5.2	Traditional Hyper-spectral Cameras	98
5.3	Hyper Stack	100
5.4	The Provision Hyper-spectral camera	102

5.5	The Experimental Configuration	103
5.6	Trial data calibration	104
5.7	The ImSpector - direct sight imaging spectrograph	106
5.8	Vinod's hand image showing regions of interest	110
5.9	Analysis of Vinod's regions of interest Red and Green	111
5.10	Analysis of Vinod's regions of interest Blue and Yellow	112
5.11	Paul's hand image showing regions of interest	113
5.12	Analysis of Paul's hand image regions of interest Red and Green . . .	114
5.13	Analysis of Paul's hand image regions of interest Blue and Yellow . .	115
5.14	Trial Spec	118
5.15	Trial image subject 7 after 8 hours showing region of SO ₂ Map	119
5.16	SO ₂ Map of region of trial image subject 7 after 8 hours	120
6.1	A simple unit Intensity TPSF	123
6.2	A TPSF composed of two blocks	126
6.3	Error in fit with $A = ae^{-b\mu_a} + a_2e^{-b_2\mu_a} + c + \text{dlog}(\mu_a)$, over the absorbtion range μ_a 0 – 0.3 mm ⁻¹ v scattering coefficient μ'_s 0.0743 – 1.6817 mm ⁻¹	129
6.4	Error in fit with $A = ae^{-b\mu_a} + a_2e^{-b_2\mu_a} + a_3e^{-b_3\mu_a} + c + \text{dlog}(\mu_a)$, over the absorbtion range μ_a 0 – 0.3 mm ⁻¹ v scattering coefficient μ_s 0.0743 – 1.6817 mm ⁻¹	
6.5	Error in fit with $A = ae^{-b\mu_a} + a_2e^{-b_2\mu_a} + a_3e^{-b_3\mu_a} + a_4e^{-b_4\mu_a} + c + \text{dlog}(\mu_a)$, over the absorbtion range μ_a 0 – 0.3 mm ⁻¹ v scattering coefficient μ_s 0.0743 – 1.6817 mm ⁻¹	131
6.6	Error in SO ₂ with (a) $A = ae^{-b\mu_a} + a_2e^{-b_2\mu_a} + c + \text{dlog}(\mu_a) + f(\lambda)$ and (b) $A = ae^{-b\mu_a} + a_2e^{-b_2\mu_a} + a_3e^{-b_3\mu_a} + c + \text{dlog}(\mu_a) + f(\lambda)$	132
6.7	Error in fit with (a) 12 term series, and (b) $A = ae^{-b\mu_a} + a_2e^{-b_2\mu_a} + c + \text{dlog}(\mu_a)$, over the absorbtion range μ_a 0 – 0.3 mm ⁻¹ v scattering coefficient μ'_s 0.0743 – 1.6817 mm ⁻¹	137
6.8	Ratio of coefficients for first 6 terms of a 12 term fit (fig 6.6)	138

Abstract

The measurement of oxygen saturation SO_2 is one of the vital signs relied on by the medical profession. Pulse oximeters are widely used in many branches of medicine; and are the most widely used method of assessing oxygen saturation. However they can only be applied to an extremity (usually a finger or toe), need calibration, and are known to be inaccurate under certain conditions.

The object of this research was to develop an oximeter, that does not require a pulsatile signal, (and so can be used anywhere on the body); can be used in either transmission or reflective mode; does not require calibration; and does not suffer from the known problems of pulse oximeters.

The instrument must work with reflected light, and so the first step was to develop a Monte Carlo simulation of the Attenuation spectra, for visible light, from a scattering media (tissue).

A Mathematical model of the attenuation surface had then to be found, and its effect on the absorption spectra of oxyhemoglobin HbO_2 and de-oxyhemoglobin Hb understood. Then the oxygen saturation the ratio of HbO_2 to total haemoglobin could be recovered.

Methods of computing oxygen saturation from the raw reflectance spectra were devised and then tested with single reflection spectra, the results indicate that a low cost instrument could be developed. The technique was applied to images from a hyper-spectral camera, this instrument takes a full spectrum at each pixel of an image, and enabled an oxygen saturation map for large areas of the body to be produced. The technique is being used with AstraZenca Ltd as a bio marker skin for irritation

studies.

ACKNOWLEDGEMENTS

I would like to thank my supervisors Dr John Crowe and Dr John Walker for all their time help and encouragement. I would also like to thank Dr Malcolm Woolfson for his help and interest in the work.

I am grateful to the staff and students of the Department of Electrical and Electronic Engineering for providing such excellent facilities and support.

Finally I would like to thank my internal examiner, Dr Steve Morgan and my external examiner Dr Deric Jones.

Chapter 1

Introduction

1.1 Oximetry

The life of every cell in the human body depends on the supply of oxygen and nutrients, and the removal of carbon dioxide and other waste. These essential services are provided by the circulatory system and include the transport of red blood cells loaded with oxygen from the lungs to the extremities, and return of oxygen depleted red blood cells to be recharged. The load of oxygen carried by the red blood cells to the tissue is a valuable indicator of the likely health of that tissue. The measurement of this is known as oximetry, and is valuable to clinicians working in respiratory medicine, anesthesia, reconstructive surgery and many other fields.

For example: oximetry can be used to evaluate cerebral oxygenation during the various phases of ischaemic stroke [1] to detect nocturnal de-saturation in patients with stable heart failure [2]; and for neonatal monitoring [3]. Reconstructive surgeons are interested in the blood supply to, and the perfusion of oxygen within skin flaps, and tissue grafts [4].

Assessment of the oxygen content of blood can be performed in various ways. The

gold standard is blood gas partial pressure measurement known as co-oximetry, and requires a sample of blood to be taken so that the partial pressures of oxygen and carbon dioxide can be measured via an electro-chemical technique. This technique measures the partial pressure of oxygen which can be converted to oxygen saturation by the appropriate oxygen disassociation curve. Optical techniques, such as pulse oximetry have also been developed, which allow continuous monitoring. These techniques measure oxygen saturation which is related to partial pressure via the oxygen disassociation curve (fig 1.1) and is a good measure of oxygenation, except when the curve is largely flat indicating that a large change in partial pressure will result in only a small change in oxygen saturation. Oxygen saturation, SO_2 is measured as a percentage of haemoglobin carrying oxygen, in the form of oxy- haemoglobin, with respect to the total capacity.

$$SO_2 = \frac{\text{oxyhemoglobin concentration}}{\text{total hemoglobin concentration}} * 100\% \quad (1.1.1)$$

that is:

$$SO_2 = \frac{HbO_2}{HbO_2 + Hb} * 100\% \quad (1.1.2)$$

where:

HbO_2 = Concentration of oxyhemoglobin

Hb = Concentration of deoxyhemoglobin

The arterial blood supply in a healthy subject has an SO_2 of approximately 98% while the venous or return supply has an average of 75% [5]

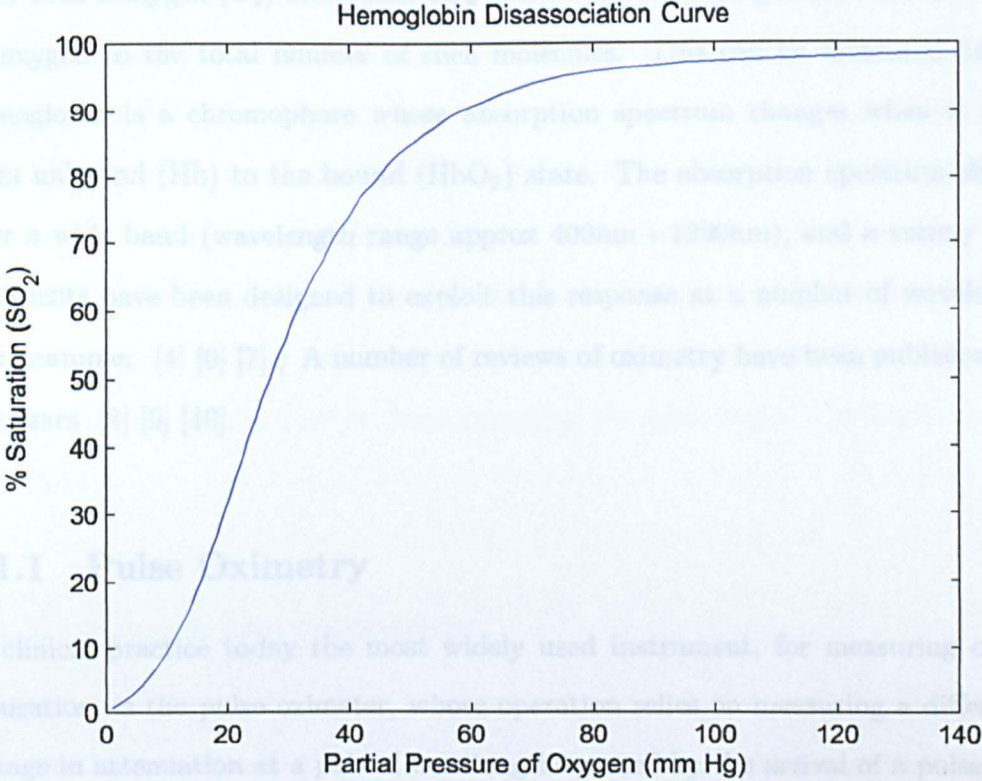


Figure 1.1: This Curve shows the relationship between SO_2 and the partial pressure of oxygen in the blood of a normal healthy adult, the partial pressure is the important parameter, however it cannot be measured, by non-invasive means.

Oxygen is transported by hemoglobin, an iron based compound within the red blood cells which has a high affinity for oxygen. Each haemoglobin molecule can bind with 4 oxygen (O_2) molecules, SO_2 is the ratio of haemoglobin molecules bound to oxygen to the total number of such molecules. This can be measured because hemoglobin is a chromophore whose absorption spectrum changes when it moves from unbound (Hb) to the bound (HbO_2) state. The absorption spectrum changes over a wide band (wavelength range approx 400nm - 1200nm), and a variety of instruments have been designed to exploit this response at a number of wavelengths (for example: [4] [6] [7].) A number of reviews of oximetry have been published over the years [8] [9] [10]

1.1.1 Pulse Oximetry

In clinical practice today the most widely used instrument, for measuring oxygen saturation, is the pulse oximeter, whose operation relies on measuring a differential change in attenuation at a pair of wavelengths caused by the arrival of a pulse at an extremity. The Pulse oximeter's success has been largely due to the use of the pulse, so giving a signal that can be locked on to, and technological advances in electro-optic components, they are relatively cheap to produce and have brought many benefits to clinicians, due to their ease of use. However they are limited to pulsatile flow monitoring, have range and accuracy limitations, and their calibration is largely empirical and varies from manufacturer to manufacturer [11] [12]

Pulse oximetry does not satisfy all clinical requirements, the need for a pulse at an extremity, which is thin enough to allow a transmission based instrument to work,

limits its use in patients whose circulation at the extremities may shut down so that these readings do not reflect core oxygen saturation. Pulse oximeters are known to be less accurate at low saturation values and are used to provide a trend indication only at saturations below about 80%. The Nellcor reflectance probe was validated using piglets [13] [14] and found to be within 5% of co-oximetry over a wide range of SO_2 . Improvements to pulse oximetry, to remove error caused by patient movement and response time are still being developed [15]. However pulse oximeters, which are a clinical and commercial success, still have fundamental limitations, they are clumsy for the patient to wear and so unsuited to long term ambulatory use. They are also plagued with motion artifacts (readings are affected and lost due to patients movement).

1.1.2 Recent Developments

Within the last 10 years a variety of work has been published extending a number of known techniques. Kurth [16] developed a multi-wavelength frequency-domain near-infrared cerebral oximeter, using diffusion theory to approximate the phase shift due to the effect of scattering at three wavelengths. The instrument used 3 laser diodes at wavelengths 754 nm, 785 nm and 816 nm, with a reference wavelength at 780 nm not directed through the sample. The laser light intensities were modulated at 200 MHz. The instrument employs heterodyne frequency-domain technology to monitor phaseshifts at the three measuring wavelengths. The results compare favourably with co-oximetry for the model of the human brain used in the experimental work.

Dougherty et al [6] developed an instrument combining laser Doppler flowmetry and

reflection pulse oximetry, both of which depend on laser light back-scattered from the skin tissue. Simultaneous and continuous measurements of both microvascular blood flow and blood oxygen saturation were obtained from the same measurement site. Oximetry readings from the combined instrument were compared with a pulse oximeter in a limited clinical study, they showed a variability of 4% and a difference of (5 - 10) %.

Boalth et al [17] combined co-oximetry and multi-spectral instrument to produce a calibration free instrument that can be used near to the patient. The measurement of the partial pressure of carbon dioxide $p\text{CO}_2$ is by a multi-wavelength spectral technique. The measurement is made at three wavelengths 4228, 4268 and 4308 nm, plasma has an absorption peak at 4268nm . To measure $p\text{CO}_2$ the blood sample is compressed and de-compressed to modulate the signal.

These recent advances plus new clinical applications, such as mapping SO_2 surfaces using NMR techniques [18], investigating lung function, monitoring the health of organs on the operating tables and other areas of research, demonstrate the need for more flexible, accurate and non-invasive oximetry, to give a better picture of the oxygen supply and more rapid response to changes without impeding the surgeon or being of inconvenience for the patient.

1.1.3 Summary

The above brief review demonstrates the value of SO_2 monitoring in clinical practice and how the pulse oximeter has, largely due to its ease of use, become the instrument of choice. However, continuing work in the field demonstrates that there are still improvements that would bring benefit to patient care. Ideally an instrument that could measure SO_2 non-invasively from **any** tissue surface, that would not need empirical calibration and would provide an accurate measure even in the presence of other haemoglobin derivatives is needed. The subject of this thesis is the development of such an oximeter using the visible spectrum, ideally applicable to long term ambulatory care. The limitations of current instruments leave room for the introduction of novel oximeters, to take their place beside pulse oximeters as diagnostic and monitoring tools.

1.2 Introduction to Lambert-Beer Law based oximetry

In oximetry the constituent absorbers are usually de-oxyhemoglobin, oxyhemoglobin, and carboxyhemoglobin, the spectra of these are shown in figure 1.2.

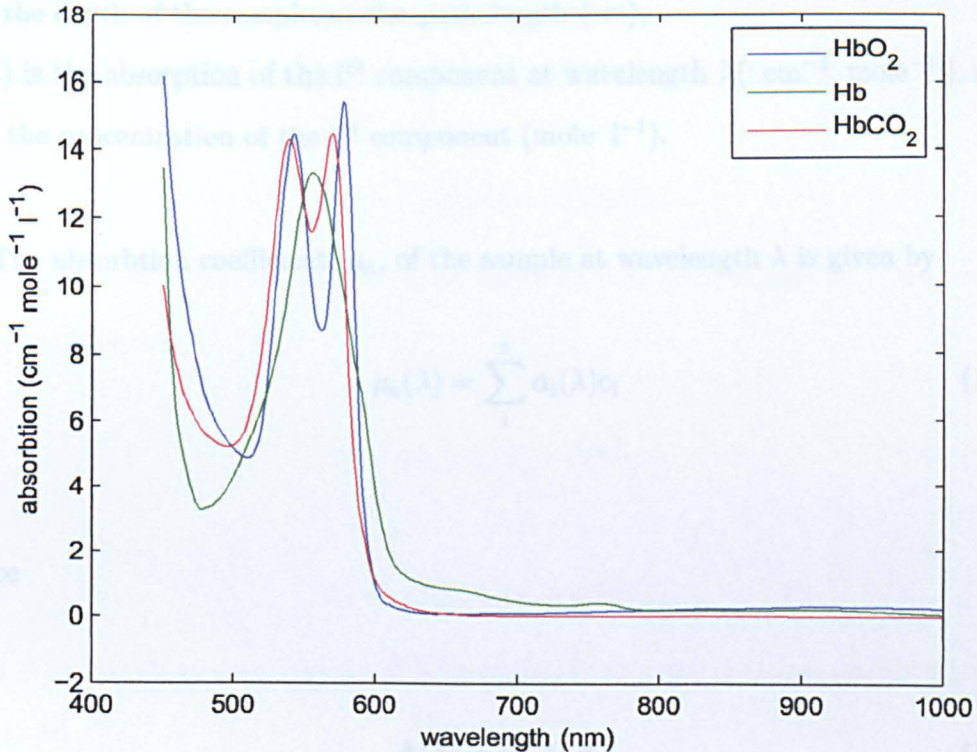


Figure 1.2: Hemoglobin Extinction Curves

If the Lambert-Beer law applies, that is the sample is non-scattering and attenuation is solely due to the absorbers the attenuation A at wavelength λ is given by

$$A = \epsilon \cdot c \cdot d \quad (1.2.4)$$

The required concentrations may be found by inverting ϵ

$$A(\lambda) = \ln \frac{I_0}{I} = \sum_i^n \alpha_i(\lambda) c_i d \quad (1.2.1)$$

where

I_0 is the illumination incident on the sample,

I is the measured illumination at the detector,

d is the depth of the sample, or the path length (cm),

$\alpha_i(\lambda)$ is the absorption of the i^{th} component at wavelength λ ($\text{cm}^{-1} \text{ mole}^{-1}$), and,

c_i is the concentration of the i^{th} component (mole l^{-1}).

The absorption coefficient, μ_a , of the sample at wavelength λ is given by

$$\mu_a(\lambda) = \sum_i^n \alpha_i(\lambda) c_i \quad (1.2.2)$$

hence

$$A(\lambda) = \mu_a(\lambda) \cdot d \quad (1.2.3)$$

To determine the concentrations of n absorbing substances, measurements must be made at n , or more, wavelengths, the resulting set of simultaneous equations can then be represented in matrix notation

$$A = \alpha \cdot c \cdot d \quad (1.2.4)$$

The required concentrations may be found by inverting α

$$c = \alpha^{-1} \cdot \frac{A}{d} \quad (1.2.5)$$

Oxygen Saturation SO_2 is the ratio of oxyhemoglobin and total hemoglobin concentrations. It is dimensionless and must be multiplied by the total concentration of hemoglobin in the sample to obtain the concentration of oxyhemoglobin.

Applying this procedure to oximetry (with only HbO_2 and Hb present).

$$A = (\alpha[HbO_2] + \beta[Hb])d \quad (1.2.6)$$

Attenuation measurements must be made at two wavelengths as there are two absorbing species.

$$A_1 = \alpha[HbO_2]d_1 + \beta[Hb]d_1 \quad (1.2.7)$$

$$A_2 = \chi[HbO_2]d_2 + \delta[Hb]d_2 \quad (1.2.8)$$

Solving for the concentrations of oxygenated, HbO_2 , and deoxygenated haemoglobin, Hb , gives.

$$HbO_2 = \frac{\beta \frac{A_2}{d_2} - \delta \frac{A_1}{d_1}}{\beta\chi - \alpha\delta} \quad (1.2.9)$$

$$Hb = \frac{\chi \frac{A_1}{d_1} - \alpha \frac{A_2}{d_2}}{\beta\chi - \alpha\delta} \quad (1.2.10)$$

where :-

A_1 and A_2 are the attenuation at the two wavelengths with d_1 and d_2 the path lengths at these wavelengths.

Oxygen saturation can be computed from these concentrations:

$$SO_2 = \frac{\beta \frac{A_2}{d_2} - \delta \frac{A_1}{d_1}}{\beta \frac{A_2}{d_2} - \delta \frac{A_1}{d_1} + \chi \frac{A_1}{d_1} - \alpha \frac{A_2}{d_2}} \quad (1.2.11)$$

Or alternatively:

$$SO_2 = \frac{\beta A'_2 - \delta A'_1}{(\beta - \alpha)A'_2 + (\chi - \delta)A'_1} \quad (1.2.12)$$

Where

$$A'_2 = \frac{A_2}{d_2} \quad (1.2.13)$$

$$A'_1 = \frac{A_1}{d_1} \quad (1.2.14)$$

$$SO_2 = \frac{\beta \frac{A_2'}{A_1'} - \delta}{(\beta - \alpha) \frac{A_2'}{A_1'} + (\chi - \delta)} \quad (1.2.15)$$

When there is no scattering, the ratio of the path lengths at the measurement wavelengths $\frac{d_1}{d_2}$ will be unity and hence the term will cancel. This equality of all path lengths only occurs when the Lambert-Beer law applies, that is in media which do not scatter, however this will not be the case when making photometric measurements in tissue which is a scattering media and so the pathlength will change with measurement wavelength and other factors. It is not possible to determine whether a change in measured absorption is due to a change in total absorption or to a change in path length (d) by optical measurement. To measure HbO₂ and Hb the total absorption must be measured but only their ratio is required to determine oxygen saturation, therefore ratio measurements such as oxygen saturation can be made in tissue where any change in path length will affect measurements of all absorbers equally at each wavelength

For three or more absorbers the ratio of each to the total absorption can be computed if measurements are taken at 3 or more wavelengths.

1.2.1 Pulse oximetry

Given the dominance of pulse oximetry it is of benefit to consider the underlying theory. This assumes that the light emerging from the tissue has been attenuated by absorbers such as blood and bone according to the Lambert Beer law model. The emerging light has a relatively large DC component with a small superimposed AC component which is assumed to be due to the changing volume of blood due to the

arrival of the pulse. Haemoglobin is the main absorber in tissue so the absorption falls when the blood volume decreases and rises when it increases. It is further assumed that the pulsatile signal is due solely to changes in arterial blood volume.

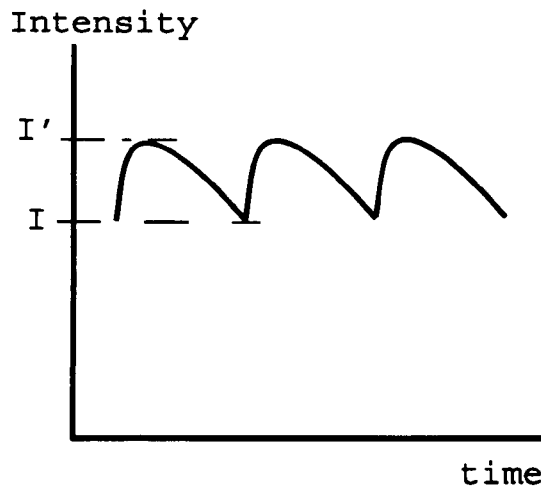


Figure 1.3: The pulsatile signal (exaggerated) from a pulse oximeter showing I' ($dc+ac$) and I (dc)

A change in the attenuation due to a pulse is given by:

$$A_{\text{pulse}} = \ln \frac{I'}{I} \quad (1.2.16)$$

Pulse oximeters do not measure this ratio directly but rather use the (AC/DC) ratio as an estimate thus :-

$$AC = I' - I \quad (1.2.17)$$

Hence:

$$A_{\text{pulse}} = \ln \frac{(I + AC)}{I} = \ln \left[1 + \frac{AC}{I} \right] \quad (1.2.18)$$

However since the pulsatile signal is small the AC signal in the NIR is 1- 2 % of I (but not necessarily in the visible [19]) this expression can be approximated (by the use of the series expansion for $\ln(1+x)$) as (AC/I) and as the AC component is small, I is approximately equal to I' giving (AC/I') or the (AC/DC) ratio.

The ratio of the AC/DC measurements at two wavelengths are used to produce:

$$R = \frac{\left(\frac{AC}{DC}\right)_{\lambda_1}}{\left(\frac{AC}{DC}\right)_{\lambda_2}} = \frac{A_1}{A_2} \quad (1.2.19)$$

This ratio is used as an estimate for the ratio of the attenuations of the arterial pulse at each wavelength. Most pulse oximeters use red (660nm) and near-infrared (904nm) light. The equation for oxygen saturation (eqn 1.2.15) then becomes:

$$S = \frac{k_1 - k_2 R}{k_3 R + k_4} \quad (1.2.20)$$

Where the constants (k_n) are related in theory to the specific absorption coefficients. This leads to the familiar known fall in S with R , with the denominator gradually increasing the slope as R increases.

Pulse oximetry relies on measurements at two wavelengths only and computes a differential attenuation between the background and when the pulse is present to calculate oxygen saturation. This theory assumes attenuation is due only to absorption, with the pulsatile signal due to changes in the volume of arterial blood only. These assumptions are clearly incorrect, and is in part why there is a need to calibrate pulse oximeters and why their accuracy is limited to 2-3% in normal use and 5 % at low saturations [14]. For general clinical applications this accuracy is sufficient, although it can be frustrating when pulse oximeters on the same patient give different readings, the absolute value of oxygen saturation is less important than the trend. However as noted in the introduction [18] non-invasive and more rapidly responding oximeters are needed by surgeons. Increase accuracy may lead to new diagnostic tools. It is noted at this point that most other oximeters (including those using infra-red spectrophotometry) also assume a linear relationship between A and μ_a , although the attenuation offset due to scattering is usually included. Such models will be considered in more detail in later chapters.

1.3 Oximetry from reflectance spectra

1.3.1 Introduction

Pulse oximetry is mostly carried out with transmission signals, which involve large absolute attenuations, however the technique does not require absolute measurements

of intensity but rather differential measurements of the change in intensity of the pulsatile component of the absorption. Oximetry using transmission spectra requires measurements which are related to absolute intensity. As a sensitive photometer is required to measure the transmitted light, an attenuator (eg: neutral density filter) is used to measure the incident light, this complicates and may compromise the spectra obtained (neutral density filters have spectral impurities). Transmission spectra are limited to extremities because of high attenuation. In reflectance the reflected light can be 50% of the incident light enabling absolute reflectance spectra to be measured, and to be measured on any exposed surface of the subject. If a reflectance probe or imaging technique can be developed it should show important advantages over transmission methods.

Reflectance pulse oximetry probes have, according to some researchers [20], not proved very accurate or reliable. Reflectance probes which measure a full spectrum were used for much of the experimental work reported, but it was not until hyperspectral imaging cameras became available that the variation of oxygen saturation across the surface of tissue could be mapped. Mansfield et al [21] demonstrated oxygen saturation mapping in rats using a partially detached, rectangular skin flap with an arterial blood supply from one end only, a change in the oxygen saturation gradient is clearly visible 2 hours after the surgery to detach the flap. Hyperspectral imaging to map perfusion in human subjects has also been demonstrated by Zuzak et al, [22] and by Hirsch et al for monitoring the acidity of blood [23].

1.3.2 Research by Lubbers et al

Much of the early work in reflectance photometry as applied to tissue was done by Lubbers and his co-workers. In 1969 Lubbers and Wodick [24] report on the examination of multicomponent systems in biological materials. In this work they make use of a scanning photometer to make the wavelength measurements and they rely on a linear transform, (Lambert Beer with some corrections for inhomogeneity and wavelength variations). Lubbers series of papers seek an improved transform to replace The Lambert-Beer Plus offset approximation.

1.3.3 The attenuation v absorption transform

The required transform can be plotted from the absorption spectrum and the attenuation spectrum (fig 1.4) provided that the oxygen saturation is known. The attenuation spectrum in the figure is the result of a Monte Carlo simulation, for transmission through a 1cm thick slab of homogenous media with a reduced scattering coefficient $\mu'_s = 1.0\text{mm}^{-1}$ oxygen saturation = 100%. The oxygen saturation is computed to be 89% in this example.

1.3.4 The effect of composite media

In 1985 Lubbers and Wodick [25] investigated the effect of rearranging the order of scattering media and absorbers in artificial composite media. They used 6 sets of 8 cavities each, placed side by side to simulate an absorbing media. The 8 cavities in each set were filled with an absorbing media in decreasing depths so the first cavity

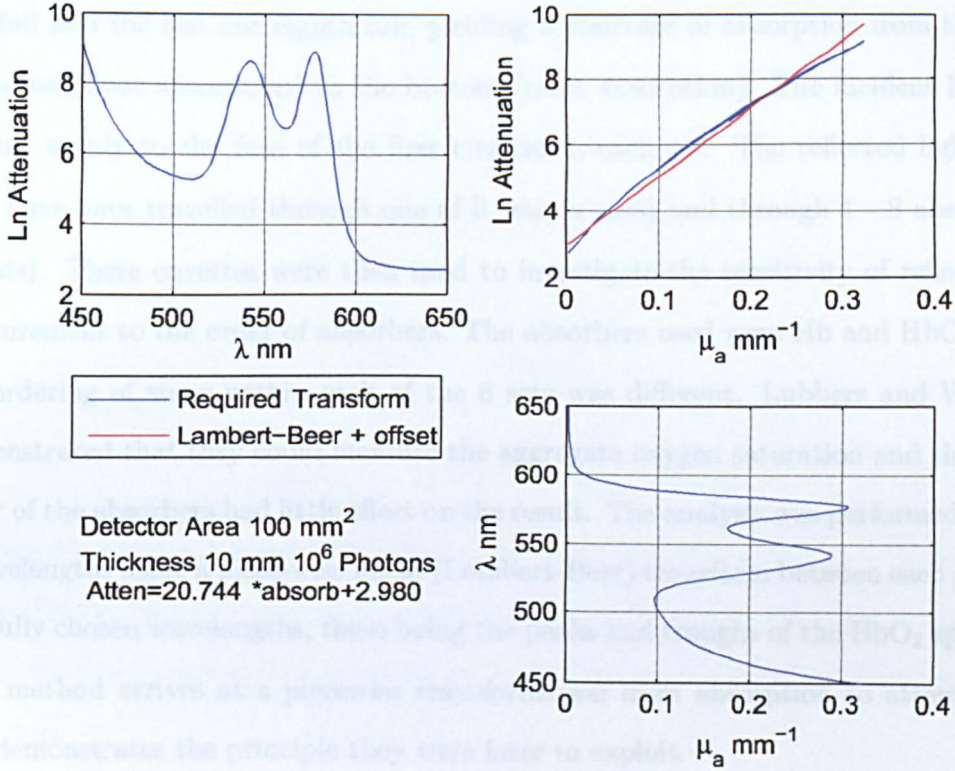


Figure 1.4: The transform from absorption to attenuation showing the required transform and the Lambert-Beer + offset approximation

In 1998 Hoffmann, Lubbers and Heist demonstrated transform derived from Kubelka-Munk theory of reflectance from a semi-infinite scattering slab of media. [26]

The reflectance $R_{\infty}(\lambda)$ of a semi-infinite plane scattering slab can be expressed by Louyakis and Sigan 1995 [27]

1.3.4 The effect of composite media

In 1975 Lubbers and Wodick [25] investigated the effect of rearranging the order of scattering media and absorbers in artificial composite media. They used 6 sets of 8 cuvettes each, placed side by side to simulate an absorbing media. The 8 cuvettes in each set were filled with an absorbing media in decreasing depths so the first cuvette was full and the last one eighth full, yielding a staircase of absorption from the top of the set (least absorption) to the bottom (most absorption). The incident light is applied evenly to the face of the first cuvette in each set. The reflected light will then have travelled through one of 6 sets (x axis) and through 1 - 8 absorbers (y axis). These cuvettes were then used to investigate the sensitivity of reflectance measurement to the order of absorbers. The absorbers used were Hb and HbO₂, but the ordering of these within each of the 6 sets was different. Lubbers and Wodick demonstrated that they could measure the aggregate oxygen saturation and that the order of the absorbers had little effect on the result. The analysis was performed using 5 wavelengths using a piece-wise linear (Lambert-Beer) transform between each pair of carefully chosen wavelengths, these being the peaks and troughs of the HbO₂ spectra. This method arrives at a piecewise transformation from absorption to attenuation and demonstrates the principle they were later to exploit.

1.3.5 The Kubelka-Munk transform

In 1998 Hoffmann, Lubbers and Heise demonstrated transform derived from Kubelka-Munk theory of reflectance from a semi-infinite scattering slab of media. [26]

The reflectance $R_{\infty}(\lambda)$ of a semi-infinite plane scattering slab can be expressed by Loaylka and Riggs 1995 [27]

$$2a(\lambda) + s(\lambda) = s(\lambda)\cosh(\gamma_R(\lambda)) \quad (1.3.1)$$

Where

$$\gamma_R(\lambda) = -\ln R_{\infty}(\lambda) \quad (1.3.2)$$

$a(\lambda)$ is the absorption coefficient

$s(\lambda)$ is the scattering coefficient

This follows directly from Kubelka-Munk theory ie:

$$\frac{k(\lambda)}{s(\lambda)} = \frac{(1 - R_{\infty}(\lambda))^2}{2R_{\infty}(\lambda)} \quad (1.3.3)$$

$$\frac{1}{2}\left(\frac{1}{R_{\infty}(\lambda)} + 1\right) - 1 = \cosh(\gamma_R(\lambda)) - 1 \quad (1.3.4)$$

Here $k(\lambda) = 2a(\lambda)$ is twice the absorption coefficient $a(\lambda)$ and $s(\lambda)$ is the scattering coefficient, both are wavelength dependent and will also be dependent on position within the tissue unless it is assumed to be homogeneous. $\gamma_R(\lambda)$ is the reflectance spectrum.

Hence the reflectance spectrum is:

$$\frac{2a(\lambda)}{s(\lambda)} \quad (1.3.5)$$

Over the optical spectrum a simple approximation for the variation of scattering with wavelength is used, the scattering is assumed to decrease with wavelength from

a value, and with a slope obtained by fitting, from the shortest wavelength in the range. The extinction spectra are then 'transformed' to match the results of linearising the measured spectrum. It is noted that this will introduce errors as scattering is a function of attenuation, wavelength, thickness and other parameters, but is a reasonable assumption if the scattering is assumed only to vary with wavelength.

$$s(\lambda) = c_0 - c_1(\lambda) \quad (1.3.6)$$

Multi-component analysis for Lambert Beer law media with c_i concentrations with e_i extinction coefficients is performed by solving :

$$a(\lambda) = \sum_i (c_i e_i(\lambda)) \quad (1.3.7)$$

The transform derived from Kubelka-Munk theory is used to linearise the measured samples, so that the transform extinction coefficients can be used with least squares solution to find the ratio of the concentrations. It should be noted that relative normalised spectra are used to reduce errors in the least squares solution methodology.

$$\sum_i (c_i e_i(\lambda)) = s(\lambda) \cosh(y_R(\lambda)) \quad (1.3.8)$$

The researchers present their results computed from spectra measured from a haemoglobin-free perfused guinea pig heart. The absorbers being Cytochrome aa_3 , Cytochrome b, Cytochrome c and Myoglobin the estimate of expected error are between 1% and 6 % depending on the absorber and the concentration. The wavelength correction term applied to scattering made a significant contribution (up to 23%) in

all cases.

1.3.6 Parabolic approximation to the transform

Lubbers also approximates the transform, by curve fitting, with a parabola:

$$A = G + \mu_a d - k(\mu_a d)^2$$

This leads to an improved transformation, however for most of his work he ignores the squared term to reduce computation time accepting the relative small error for the high absorption to scattering ratio of the media he is using. For a comparison of these transforms see section 2.3.

1.3.7 The effect of wavelength on the attenuation v absorption transform

The effect of a typical change with wavelength is shown in figure 1.5, the Lambert-Beer + offset model becomes a compromise between the extremes of the range. This compromise cannot be optimised until the range is known and so in practice should be computed for each transformation and not applied to the extinction coefficients. Finding a good transformation entails ensuring that it models the wavelength change well. The wave length transformation which is applied in fig 1.5 only improves the estimate of oxygen saturation by 0.5 % to 89.5%. In the next chapters a better equation for the transform is developed allowing oxygen saturation accuracy of better than 0.5% with attenuation spectra.

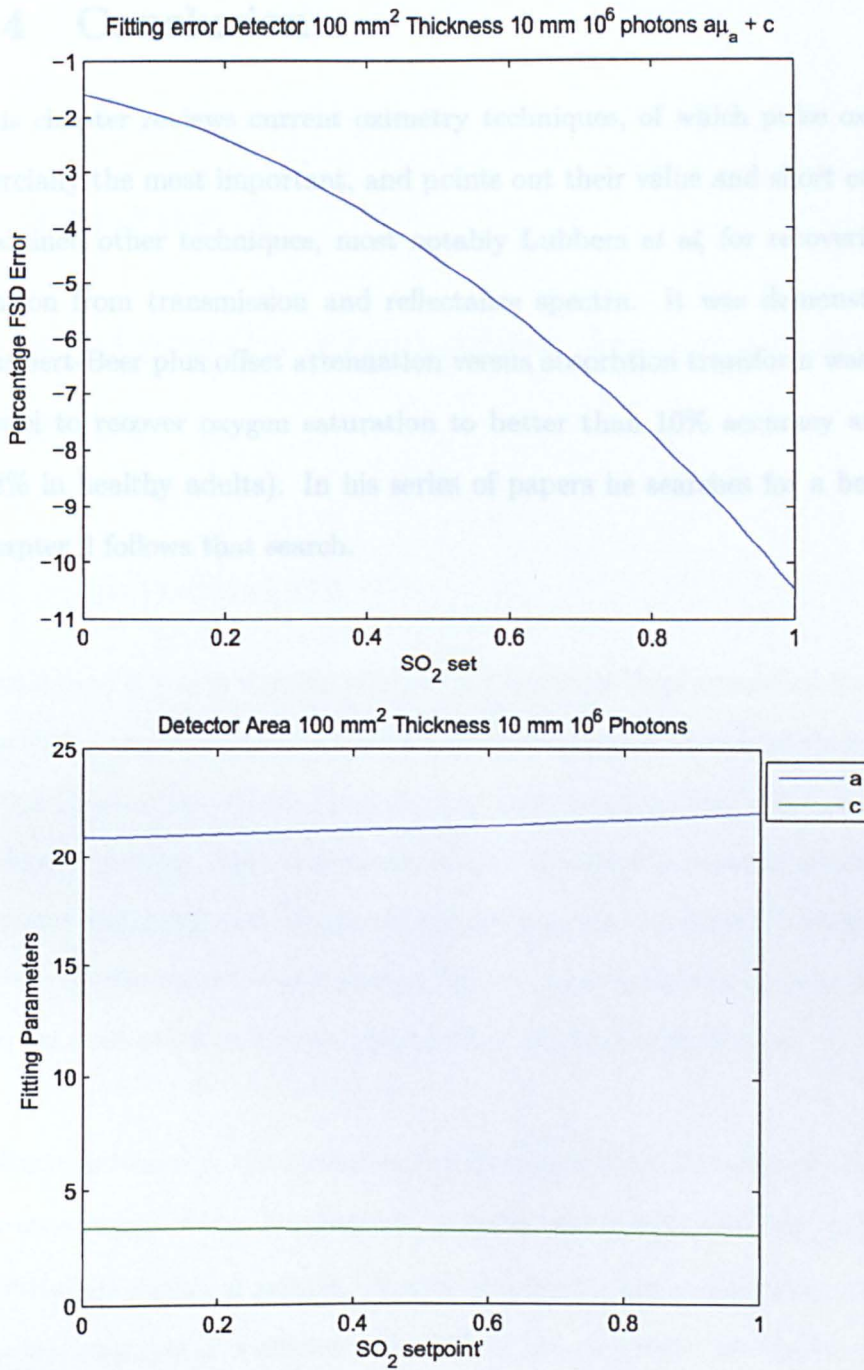


Figure 1.5: (a) the fitting error and (b) the fitting parameters using the $a\mu_a + c$ approximation

1.4 Conclusion

This chapter reviews current oximetry techniques, of which pulse oximetry is commercially the most important, and points out their value and shortcomings. It then examined other techniques, most notably Lubbers *et al*, for recovering oxygen saturation from transmission and reflectance spectra. It was demonstrated that the Lambert-Beer plus offset attenuation versus absorption transform was an inadequate model to recover oxygen saturation to better than 10% accuracy at normal levels (98% in healthy adults). In his series of papers he searches for a better transform. Chapter 2 follows that search.

Chapter 2

Spectrophotometry in scattering media

2.1 Introduction

In chapter 1 it was demonstrated that the Lambert-Beer plus offset attenuation verses absorption transform is only able to recover oxygen saturation to about 10% accuracy. In this Chapter the effect of scattering is introduced, a three dimensional attenuation surface is plotted. This surface shows the relationship between attenuation, absorption and scattering and introduces the complications involved in seeking a transform. Three transforms are tested against Monte Carlo simulations of the attenuation surface for absorption and scattering coefficients, typical for tissue.

Spectrophotometry, the measurement of attenuation (the loss of intensity) against the wavelength of the illumination, is performed to determine the proportions of the constituents within a sample. If each compound has a dissimilar spectral response (specific absorption coefficient) then if all the absorbers are known and there is no scattering of the light, their concentration can be determined. Spectrophotometry is an exact science for linear absorbing media, however with samples which scatter light

such as tissue and food this is not so.

The Lambert-Beer law which defines a linear transform between attenuation and absorption no longer applies in scattering media, under these circumstances conventional multi-component analysis fails. However Spectrophotometry (chapter 1.3.3) can still be performed if a transform (attenuation v absorption) can be applied to the attenuation data to restore the linear relationship.

Within a scattering medium attenuation (A) is no longer a linear function of the absorption coefficient (μ_a) as stated by the Lambert-Beer law. In fact the attenuation will now be a function of,

1. geometry, shape and thickness of sample,
2. illumination and detection schemes,
3. absorption coefficient $\mu_a(\lambda)$,
4. scattering coefficient $\mu_s(\lambda)$,
5. anisotropy (mean cosine of scattering angle) $g(\lambda)$.

2.1.1 Absorption alone

If the Lambert-Beer law applies the attenuation (A) is given by

$$A(\lambda) = \ln \frac{I_0}{I} = \sum_i \alpha_i(\lambda) c_i d = \mu_a d \quad (2.1.1)$$

see chapter 1.2.

2.1.2 Scattering alone

Photons passing through a scattering media, such as tissue, suffer many scattering events and so propagate along many paths of differing lengths, a 2 dimensional representation of this 3 dimensional process can be seen in the figure below

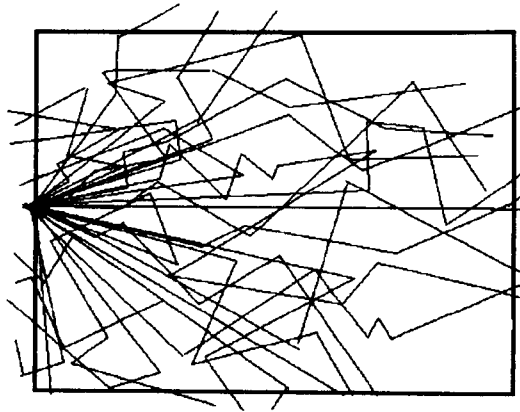


Figure 2.1: The Scattering process 2D representation of the many paths. The illumination enters the sample centre left.

Photons will travel via different paths, due to their random scattering and so take different times to reach the detector. This temporal spread is presented as the Temporal Point Spread Function (TPSF) and shown in figure 2.2. This is the impulse response of the sample, i.e. output from the sample as a function of time in response to an impulse of light being incident on the sample.

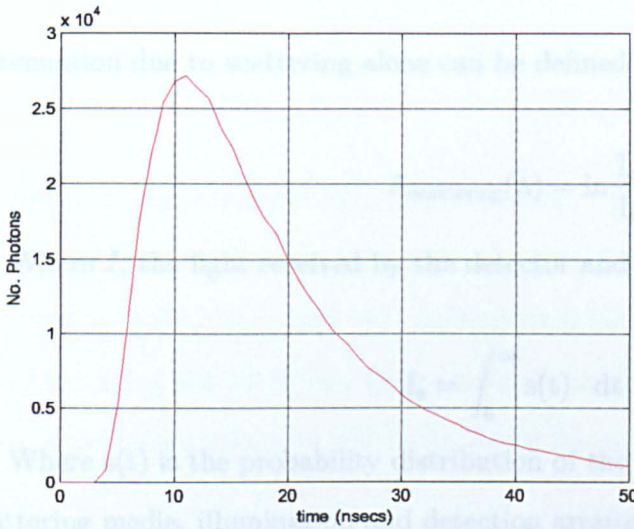


Figure 2.2: TPSF 10^8 photons incident on a 10mm thick sample having an effective scattering coefficient $\mu'_s(\lambda) = 1.25\text{mm}^{-1}$ ($\mu'_s(\lambda) = \mu_s(\lambda) \cdot (1 - g(\lambda))$)

Scattering alone implies that the path length travelled by each photon will be different, for a given sample (with no absorbers) the variety of pathways, and so the path length, is no longer fixed or even known. The Temporal Point Spread Function (TPSF) (fig 2.2) is a probability distribution and characterised by its mean and standard deviation.

Attenuation due to scattering alone can be defined as:-

$$A_{\text{scattering}}(\lambda) = \ln \frac{I_o}{I_s} \quad (2.1.2)$$

Where I_s the light received by the detector and is given by:-

$$I_s = \int_0^{\infty} s(t) \cdot dt \quad (2.1.3)$$

Where $s(t)$ is the probability distribution of the flight time of photons for a given scattering media, illumination and detection arrangement.

2.1.3 Scattering plus an absorber

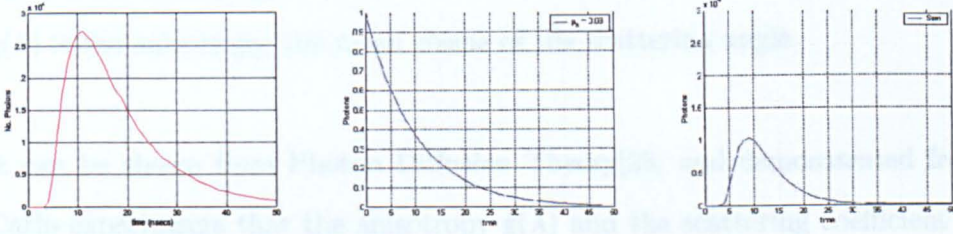


Figure 2.3: light passes through a scattering media $\mu'_s = 1.25\text{mm}^{-1}$, then through an absorber $\mu_a = 0.03\text{mm}^{-1}$ resulting in the TPSF (far right)

Assuming the scattered light passes through the absorber and is absorbed according to the Lambert-Beer law, then as the path length is different for each photon, they will each be attenuated by a different amount. The resulting TPSF will be the result of adding the TPSF due to scattering to the effect of the absorber (i.e. photons with flight times of 20nsecs will be absorbed by the corresponding absorption).

The total attenuation can be computed as follows

$$A_{\text{Total}} = \ln \frac{I_0}{I_s} + \ln \frac{I_s}{I_a} \quad (2.1.4)$$

Where (for fixed geometry, illumination and detector arrangement)

$$I_a = \int s(t) \cdot e^{-\mu_a c t} \cdot dt \quad (2.1.5)$$

$$A(\lambda) = f[\mu_a(\lambda), \mu_s(\lambda), g(\lambda)] \quad (2.1.6)$$

Where

$\mu_a(\lambda)$ is the absorption coefficient

$\mu_s(\lambda)$ is the scattering coefficient

$g(\lambda)$ is the anisotropy, the mean cosine of the scattering angle

It can be shown from Photon Diffusion Theory[28] and demonstrated from Monte Carlo experiments that the anisotropy $g(\lambda)$ and the scattering coefficient $\mu_s(\lambda)$ can be combined as a single coefficient $\mu'_s(\lambda)$:

$$\mu'_s(\lambda) = \mu_s(\lambda)(1 - g(\lambda)) \quad (2.1.7)$$

This assumption allows us to use effective scattering in our equation and thus reduce the number of variables in our model. Substituting :-

$$A = \ln \frac{I_o}{\int_0^\infty s[\mu'_s(\lambda)] \cdot e^{-\mu_a(\lambda)ct} \cdot dt} \quad (2.1.8)$$

Hence provided that the geometry is fixed and that the illumination and detector arrangements don't alter, the attenuation depends solely on the effective scattering and the absorption coefficients. This equation gives rise to an attenuation surface (fig 2.4) which can be plotted from Monte Carlo data.

2.2 Models used previously

A number of attenuation surface models have been used from the simple straight line plus offset model (Lambert's Beer law with a constant to allow for the loss due to scattering alone), the probabilistic models used by Lubbers (section 1.3.5) and the power law model from photon diffusion theory (Lambert Beer + Offset (2.2.1)).

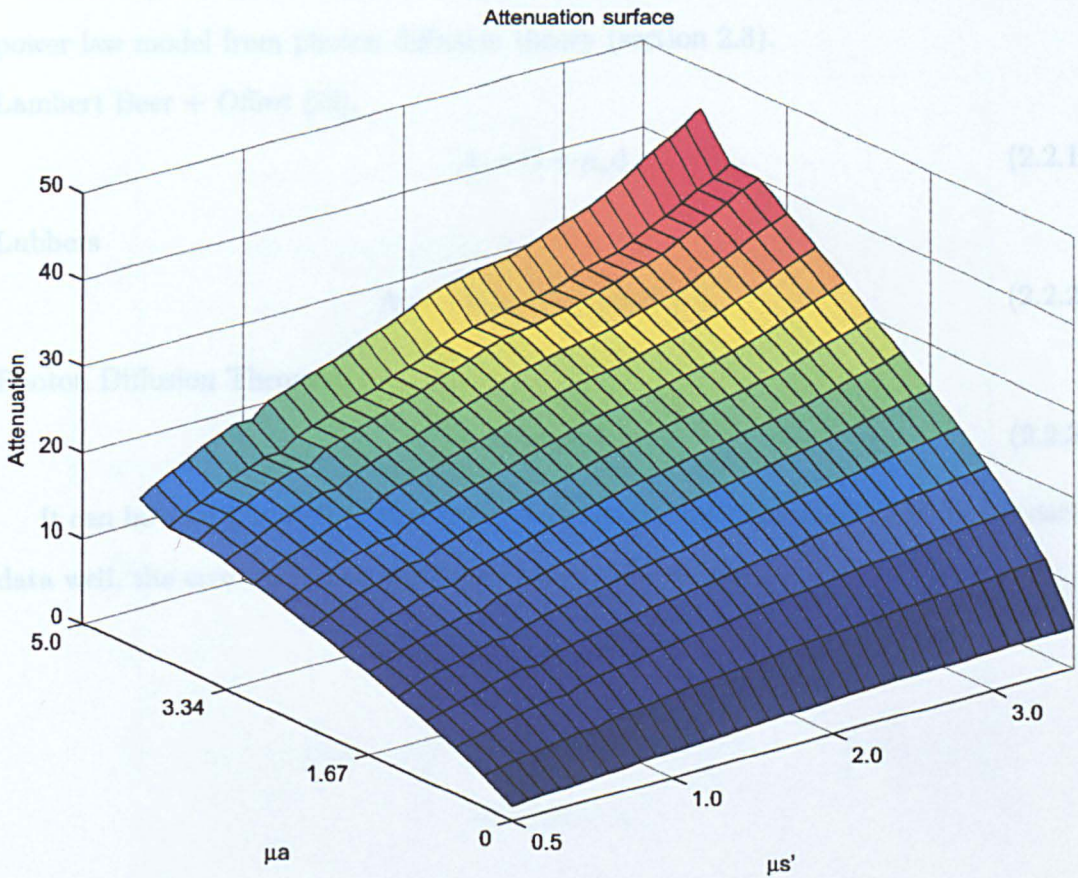


Figure 2.4: Attenuation surface from Monte Carlo data 10^8 photons incident on a 10mm thick sample with μ_a in the range $0-5 \text{ mm}^{-1}$ and μ_s' in the range $0 - 3.3 \text{ mm}^{-1}$

2.2 Models used previously

A number of attenuation surface models have been used from the simple straight line plus offset model (Lambert Beer Law with a constant to allow for the loss due to scattering alone), the parabolic models used by Lubbers (section 1.3.5) and the power law model from photon diffusion theory (section 2.3).

Lambert Beer + Offset [29],

$$A = G + \mu_a d \quad (2.2.1)$$

Lubbers

$$A = -a(\mu_a d)^2 + b\mu_a d + c \quad (2.2.2)$$

Photon Diffusion Theory

$$A = a\mu_a^{\frac{1}{2}} + c \quad (2.2.3)$$

It can be seen (figure 2.5) that none of the approximations match the Monte carlo data well, the errors increase with the amount of scattering.

2.3 Photon diffusion theory

Photon diffusion modeling requires that the photons propagation can be approximated as diffuse (ie $\mu_s \gg \mu_a$). Under this assumption Patterson et al (1989) shows that for a narrow beam of light normally incident to the surface of a semi-infinite scattering medium the diffusion equation can be expressed as [30]:

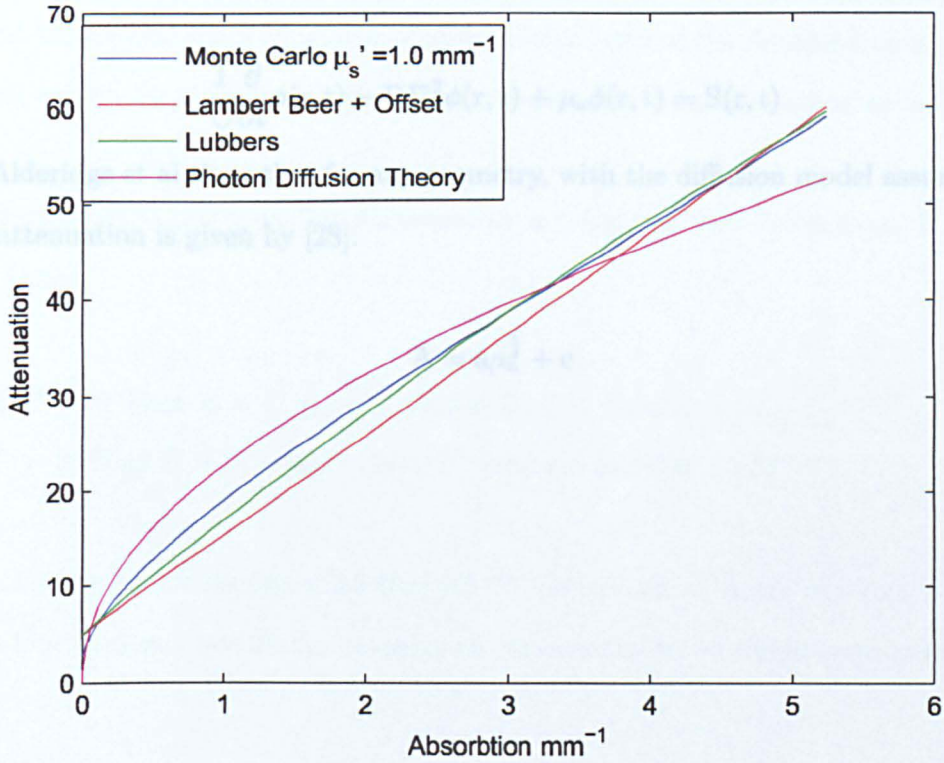


Figure 2.5: Comparison of three approximations with Monte Carlo data, in transmission, with all transmitted photons detected for a slab of thickness 1cm

2.3 Photon diffusion theory

Photon diffusion modelling requires that the photons propagation can be approximated as diffuse (ie $\mu'_s \gg \mu_a$). Under this assumption Patterson et al (1989) shows that for a narrow beam of light normally incident to the surface of a semi-infinite scattering medium the diffusion equation can be expressed as [30].

$$\frac{1}{C} \frac{\partial}{\partial t} \phi(\mathbf{r}, t) - D \nabla^2 \phi(\mathbf{r}, t) + \mu_a \phi(\mathbf{r}, t) = S(\mathbf{r}, t) \quad (2.3.1)$$

Alderidge et al show that for any geometry, with the diffusion model assumptions the attenuation is given by [28].

$$A = a \mu_a^{\frac{1}{2}} + c \quad (2.3.2)$$

2.4 The Power Law fit

In search of a better model we now introduce the moments of the TPSF in order to introduce the work of Kohl et al [31], and our later research.

The Central Moments of the TPSF (which is a statistical function) can be readily calculated and when compared with the derivatives of the Attenuation v μ_a curve match exactly in magnitude differing only in sign (all even derivatives are negative).

Presented below are plots for Attenuation and its first two derivatives, It can be seen that:

If $A'' = 0$ Then $A = G + \mu_a d$ Lambert Beer + Offset

If $A''' = 0$ Then $A = G + \mu_a d - k(\mu_a d)^2$ Lubbers (section 1.3.5)

....

It can be seen from figure 2.5 that all the derivatives of A are non-zero therefore some type of power law fit, for example an exponential series would seem most likely.

2.4.1 Derivatives and Moments

This section derives the relationship between the first and second derivative of A with respect to μ_a and the first and second central moments.

The Attenuation due to scattering is given by:

$$\text{Attenuation and its first 2 derivatives wrt } \mu_a \text{ v } \mu_a \text{ } \mu_s' = 1.0$$

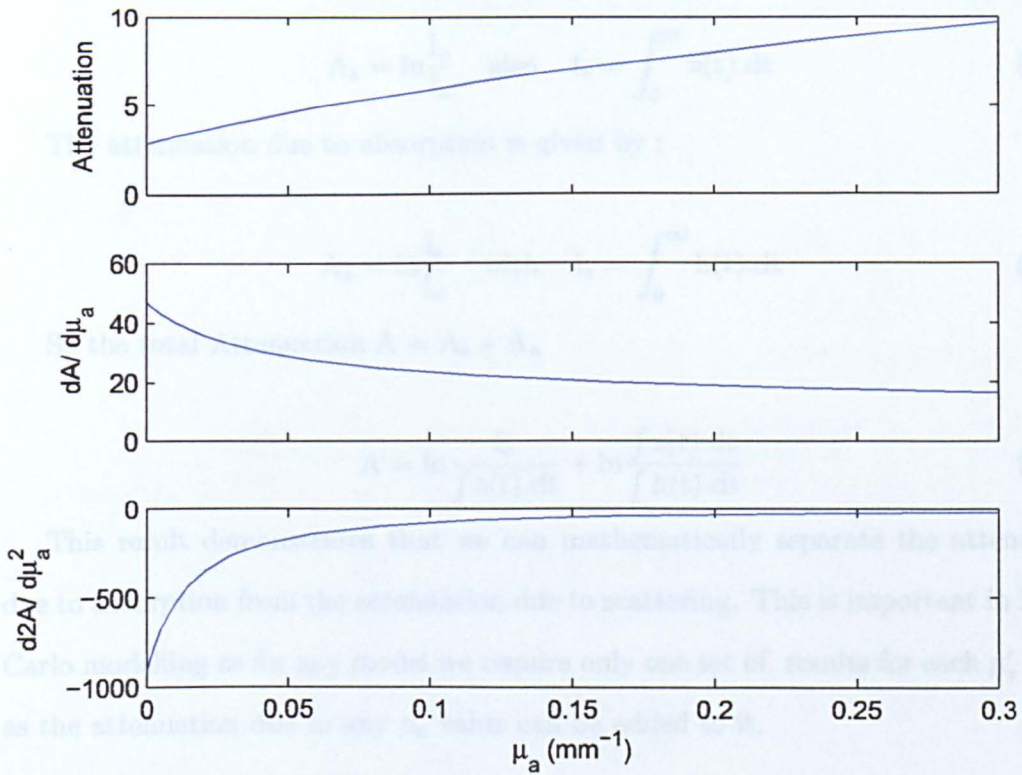


Figure 2.6: Attenuation and its first two derivatives wrt μ_a

In this analysis, the attenuation A depends on $\mu_a(\lambda)$, the geometry of the slabs, the position of both source and detector and characteristics of both source and detector and that the absorption $\mu_a(\lambda)$ is the sum of all absorbing species multiplied by their concentrations.

2.4.1 Derivatives and Moments

This section derives the relationship between the first and second derivative of A with respect to μ_a and the first and second central moments.

The Attenuation due to scattering alone is given by :

$$A_s = \ln \frac{I_o}{I_s} \quad \text{also} \quad I_s = \int_0^{\infty} s(t).dt \quad (2.4.1)$$

The attenuation due to absorption is given by :

$$A_a = \ln \frac{I_s}{I_a} \quad \text{with} \quad I_a = \int_0^{\infty} h(t).dt \quad (2.4.2)$$

So the total Attenuation $A = A_s + A_a$

$$A = \ln \frac{I_o}{\int s(t).dt} + \ln \frac{\int s(t).dt}{\int h(t).dt} \quad (2.4.3)$$

This result demonstrates that we can mathematically separate the attenuation due to absorption from the attenuation due to scattering. This is important in Monte Carlo modelling as for any model we require only one set of, results for each μ'_s value, as the attenuation due to any μ_a value can be added to it.

In this analysis the attenuation A depends on $s(t)$ which will in turn depend on $\mu_s(\lambda)$, the geometry of the shape, the position of both source and detector and characteristics of both source and detector and that the absorption $\mu_a(\lambda)$ is the sum of all absorbing species multiplied by their concentrations.

The first derivative of A with respect to μ_a :

$$A = \ln \frac{I_o}{\int s(t).dt} + \ln \frac{\int s(t).dt}{\int h(t).dt} \quad (2.4.4)$$

$$A = \ln \frac{I_o}{\int s(t).dt} - \ln \frac{\int h(t).dt}{\int s(t).dt} \quad (2.4.5)$$

$$A = \ln \frac{I_o}{\int s(t).dt} - \ln \frac{\int s(t).e^{-\mu_a ct}.dt}{\int s(t).dt} \quad (2.4.6)$$

Therefore:

$$\frac{dA}{d\mu_a} = 0 - \frac{\int s(t).dt}{\int s(t).e^{-\mu_a ct}.dt} \cdot \frac{\int s(t).(-ct)e^{-\mu_a ct}.dt}{\int s(t).dt} \quad (2.4.7)$$

$$\frac{dA}{d\mu_a} = -[-c \cdot \frac{\int s(t).te^{-\mu_a ct}.dt}{\int s(t).e^{-\mu_a ct}.dt}] \quad (2.4.8)$$

$$\frac{dA}{d\mu_a} = c \cdot \frac{\int th(t).dt}{\int h(t).dt} \quad (2.4.9)$$

$$\frac{dA}{d\mu_a} = c \cdot \langle t \rangle \quad (2.4.10)$$

Where $\langle t \rangle$ = the mean of $h(t)$ or its first moment. This result can be demonstrated using a Monte Carlo simulation (fig 2.7) by plotting the difference between the mean and the first derivative for a number of simulations (μ'_s values) and a range of μ_a .

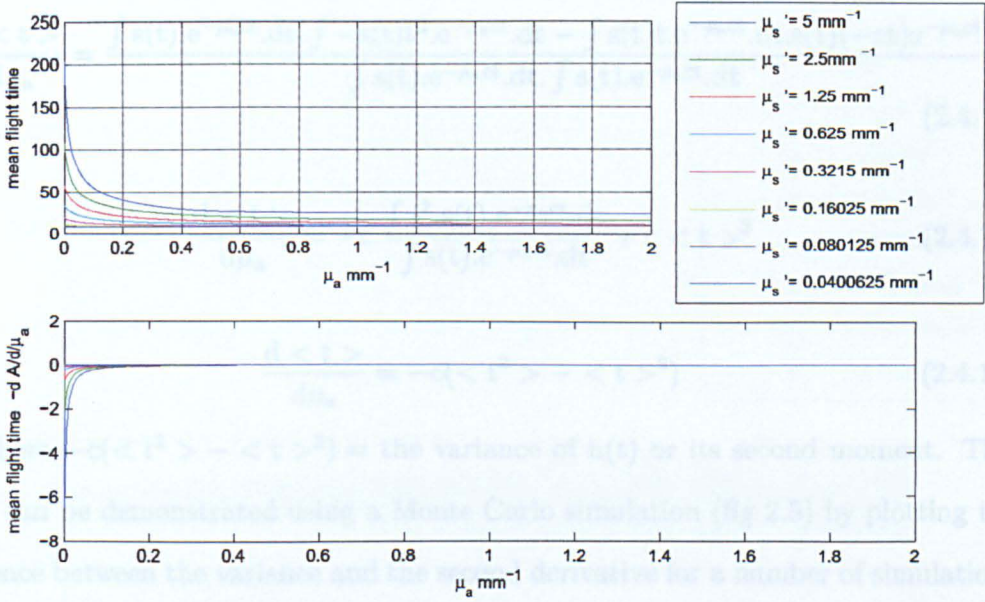


Figure 2.7: Comparing the mean of the TPSF with $\frac{dA}{d\mu_a}$ using a Monte Carlo simulation of 10^8 photons incident on a 10mm sample

These results confirm that:

$$\frac{dA}{d\mu_a} = c \cdot \langle t \rangle = \text{The Mean Pathlength} \quad (2.4.11)$$

Now consider the second derivative of A with respect to μ_a .

$$\langle t \rangle = \frac{\int t \cdot s(t) \cdot e^{-\mu_a c t} \cdot dt}{\int s(t) \cdot e^{-\mu_a c t} \cdot dt} \quad (2.4.12)$$

By the quotient Rule:

$$\frac{d \langle t \rangle}{d\mu_a} = \frac{\int s(t).e^{-\mu_a ct}.dt. \int -s(t)t^2.e^{-\mu_a ct}.dt - \int s(t)t.e^{-\mu_a ct}.dt.s(t)(-ct)e^{-\mu_a ct}}{\int s(t).e^{-\mu_a ct}.dt. \int s(t).e^{-\mu_a ct}.dt} \quad (2.4.13)$$

$$\frac{d \langle t \rangle}{d\mu_a} = -c. \frac{\int t^2.s(t).e^{-\mu_a ct}.dt}{\int s(t).e^{-\mu_a ct}.dt} + c \langle t \rangle^2 \quad (2.4.14)$$

$$\frac{d \langle t \rangle}{d\mu_a} = -c(\langle t^2 \rangle - \langle t \rangle^2) \quad (2.4.15)$$

Where $-c(\langle t^2 \rangle - \langle t \rangle^2) =$ the variance of $h(t)$ or its second moment. This result can be demonstrated using a Monte Carlo simulation (fig 2.5) by plotting the difference between the variance and the second derivative for a number of simulations (μ'_s values) and a range of μ_a .

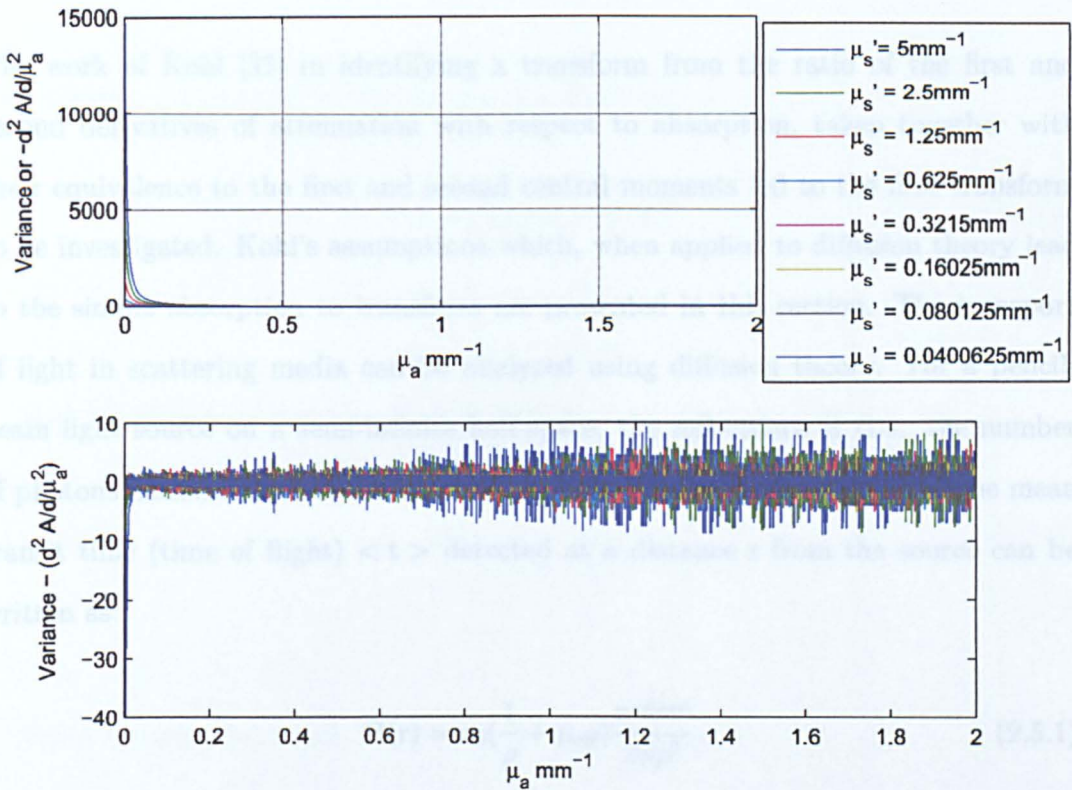


Figure 2.8: Comparing the Variance of the TPSF with $-\frac{d^2 A}{d\mu_a^2}$ using a Monte Carlo simulation of 10^8 photons incident on a 10mm sample

Note that the noise, visible in the difference plot which arises from the statistical nature of the Monte Carlo data is magnified by repeated differentiation. These results confirm that:

$$\frac{d \langle t \rangle}{d\mu_a} = -c \cdot \text{Variance}(t) = 2^{\text{nd}} \text{ Moment} \quad (2.4.16)$$

2.5 Ratio of the first and second derivatives

The work of Kohl [31] in identifying a transform from the ratio of the first and second derivatives of attenuation with respect to absorption, taken together with their equivalence to the first and second central moments led to the first transform to be investigated. Kohl's assumptions which, when applied to diffusion theory lead to the simple absorption to transform are presented in this section. The transport of light in scattering media can be analyzed using diffusion theory. For a pencil-beam light source on a semi-infinite half-space, the reflectance R (i.e., the number of photons backscattered to the surface of the medium per unit area) and the mean transit time (time of flight) $\langle t \rangle$ detected at a distance r from the source can be written as:

$$R(r) = z_0 \left(\frac{1}{\rho} + \mu_{\text{eff}} \right) \frac{e^{-\mu_{\text{eff}} \rho}}{2\pi \rho^2} \quad (2.5.1)$$

$$\langle t \rangle (r) = \frac{\rho^2}{2c[D + \rho \cdot (\mu_a D)^{\frac{1}{2}}]} \quad (2.5.2)$$

Where it is assumed that the pencil beam creates an isotropic photon source at depth z_0 ,

$$\rho = (r^2 + z_0^2)^{\frac{1}{2}} \quad \text{and} \quad z_0 = \frac{1}{\mu'_s} \quad (2.5.3)$$

where the velocity of light in the medium $c = c_0/n$,

c_0 is the velocity of light in a vacuum

and n is the refractive index of the medium.

The effective attenuation coefficient μ_{eff} is defined as,

$$\mu_{\text{eff}} = [3\mu_a(\mu_a + \mu'_s)]^{\frac{1}{2}} \quad (2.5.4)$$

and the diffusion coefficient D is defined as,

$$D = \frac{1}{3(\mu_a + \mu'_s)} \quad (2.5.5)$$

From equation 2.5.1 and 2.5.2 it can be shown that[31]:

$$\frac{\partial A}{\partial \mu_a} = \frac{3}{2 \ln 10} \frac{\rho}{\frac{1}{\rho} + \mu_{\text{eff}}} (2\mu_a + \mu'_s) \quad (2.5.6)$$

$$\frac{\partial \langle t \rangle}{\partial \mu_a} = \frac{-3}{2(\frac{1}{\rho} + \mu_{\text{eff}})^2 c} \left[\frac{\rho}{2} \frac{\mu'_s}{(\mu_a D)^{\frac{1}{2}}} - 1 \right] \quad (2.5.7)$$

The quotient of these two quantities can be simplified using the diffusion approximation which states that scattering dominates absorption $\mu_a \ll \mu'_s$ therefore:

$$\mu_{\text{eff}} \approx (3\mu_a \mu'_s)^{\frac{1}{2}} \quad \text{and} \quad D \approx \frac{1}{3\mu'_s} \quad (2.5.8)$$

Hence:

$$\frac{\frac{\partial A}{\partial \mu_a}}{\frac{\partial \langle t \rangle}{\partial \mu_a}} = \frac{-(1 + \rho \mu_{\text{eff}})c}{\ln 10 \left(\frac{\rho \mu_{\text{eff}}}{2} - \frac{\mu_a}{\mu'_s} \right)} \mu_a \quad (2.5.9)$$

For media with optical properties similar to tissue $\mu'_s = 1 - 2\text{mm}^{-1}$
 $\mu_a = 0.005 - 0.05\text{mm}^{-1}$ and source-detector distances $r = 10 - 40\text{mm}$.

and

$$\frac{\frac{\partial A}{\partial \mu_a}}{\frac{\partial \langle t \rangle}{\partial \mu_a}} = \frac{-2 \left(\frac{1}{\mu_{\text{eff}} + \rho} \right) c}{\ln 10 \rho} \mu_a \quad (2.5.10)$$

Furthermore, for large source-detector distances

$$\rho \gg \frac{1}{\mu_{\text{eff}}} \quad (2.5.11)$$

hence

$$\frac{\frac{\partial A}{\partial \mu_a}}{\frac{\partial \langle t \rangle}{\partial \mu_a}} k = \frac{-2c}{\ln 10} \mu_a \quad (2.5.12)$$

Which is a linear function of μ_a and c only

2.5.1 Solving the differential equation

Kohl's work shows that ratio of the partial derivative of attenuation with respect to the absorption coefficient, and the partial derivative of the mean flight time with

respect to the absorption coefficient, is approximately equal to a constant multiplied by the absorption.

The solution of this equation for attenuation μ_a requires the substitution of then mean flight time for the partial derivative of the mean flight time with respect to the absorption coefficient (equation 2.4.10). This novel step enables the partial differential equation to be written:-

$$\frac{d \langle t \rangle}{d\mu_a} = \frac{d^2 \mu_a}{d\mu_a^2} \quad (2.5.13)$$

Hence:

$$\frac{\frac{dA}{d\mu_a}}{\frac{d^2 A}{d\mu_a^2}} = k\mu_a \quad (2.5.14)$$

This is a differential equation which has the general solution:

$$A = a\mu_a^b + c \quad (2.5.15)$$

Which is the form of equation 2.3.2 and reduces to the Lambert-Beer law when $b = 1.0$ and the constant of integration c is zero, and the diffusion approximation when $b = 0.5$.

These results confirm the result in the previous section, however μ_a^b is less restrictive than $\mu_a^{\frac{1}{2}}$ and applies provided that $\mu_s' \ll \mu_a$.

The limited scattering range in which Kolh's approximation applies suggests that a poor fit could be expected outside this range, this effect can be clearly seen at low absorptions, however at high absorptions, this errors are damped by the dominant absorption term. The effect is further reinforced by the fitting algorithm which will always strive for zero error at the mid point and balance the mean square error, a measure of the area of the difference, either side of this point.

2.6 Comparing Models

A set of 18 Monte Carlo runs in Logarithmic increments of μ_s' from 0.0743 to 1.6817 mm^{-1} , each for 10,000,000 photons, was prepared. The absorption was incremented in 38 logarithmic steps of μ_a from 0.000014 to 5.242880 mm^{-1} and the Attenuation computed for each step. A non-linear search in combination with a matrix transpose (for linear parameters) was used to fit the equation under test to each of the Attenuation v μ_a curves. The error was then computed and plotted as a percentage against μ_a for each μ_s' value. A second plot of the parameters of the test equation v μ_a demonstrates the sensitivity of the parameters to changes in the Attenuation Surface.

2.6.1 Error and Parameter plots Lambert Beer plus offset

The error increases with scattering which is to be expected, reaching 40% at the maximum μ'_s . The slope (a) increases with μ'_s as would be expected, scattering increases the attenuation, The offset, parameter (c) mimics the loss due to scattering alone and must be a factor of any solution. Figure 2.9 shows the fitting error and parameter values using a Monte Carlo simulation of 10^8 photons incident on a 10mm thick sample of tissue for 18 values of μ'_s 0.0743 to 1.6817mm^{-1} .

2.6.2 Error and Parameter plots Photon Diffusion Theory

The error is highest when μ'_s is low, although the results in Figure 2.9(a) suggest that the error is also highest when μ'_s is high. This is because the error is highest when μ'_s is low, although the results in Figure 2.9(a) suggest that the error is also highest when μ'_s is high.

Figure 2.9(a) shows the percentage error in fitting (error increases with μ'_s) and (b) fitting parameters, Lambert Beer plus offset fit using a Monte Carlo simulation. mm^{-1}

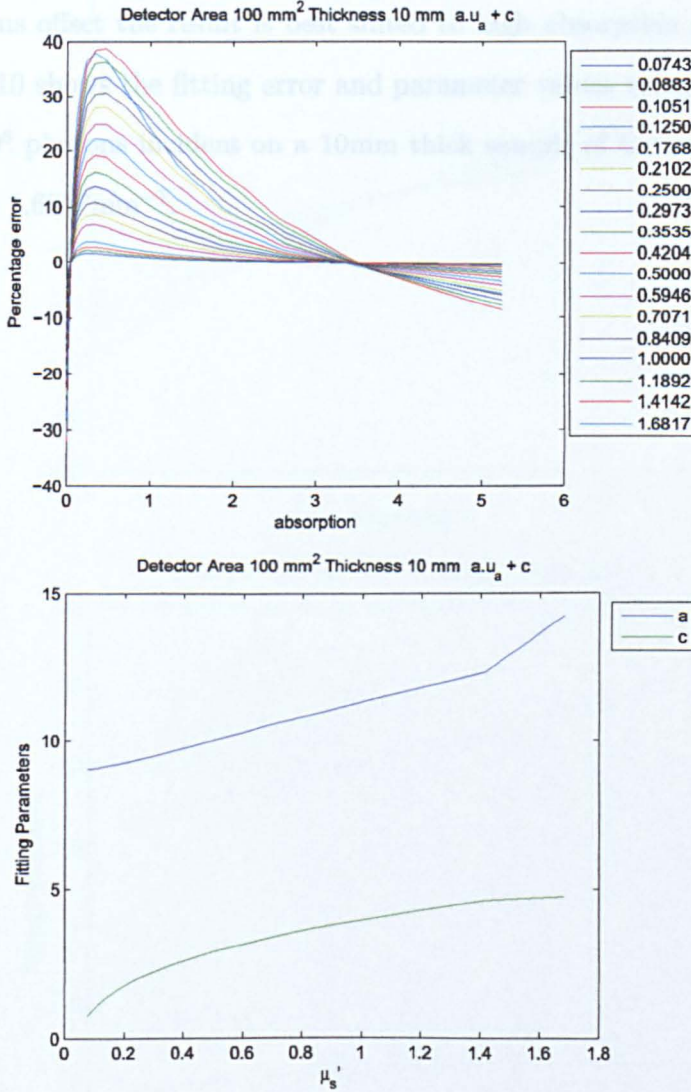


Figure 2.9: (a) percentage error in fitting (error increases with μ'_s) and (b) fitting parameters, Lambert Beer plus offset fit using a Monte Carlo simulation. mm^{-1}

2.6.2 Error and Parameter plots Photon Diffusion Theory

The error is highest when μ_a is low, although the result is better than Lambert Beer plus offset the result is best suited to high absorption and scattering regions. Figure 2.10 shows the fitting error and parameter values using a Monte Carlo simulation of 10^8 photons incident on a 10mm thick sample of tissue for 18 values from μ'_s 0.0743 to 1.6817mm^{-1} .

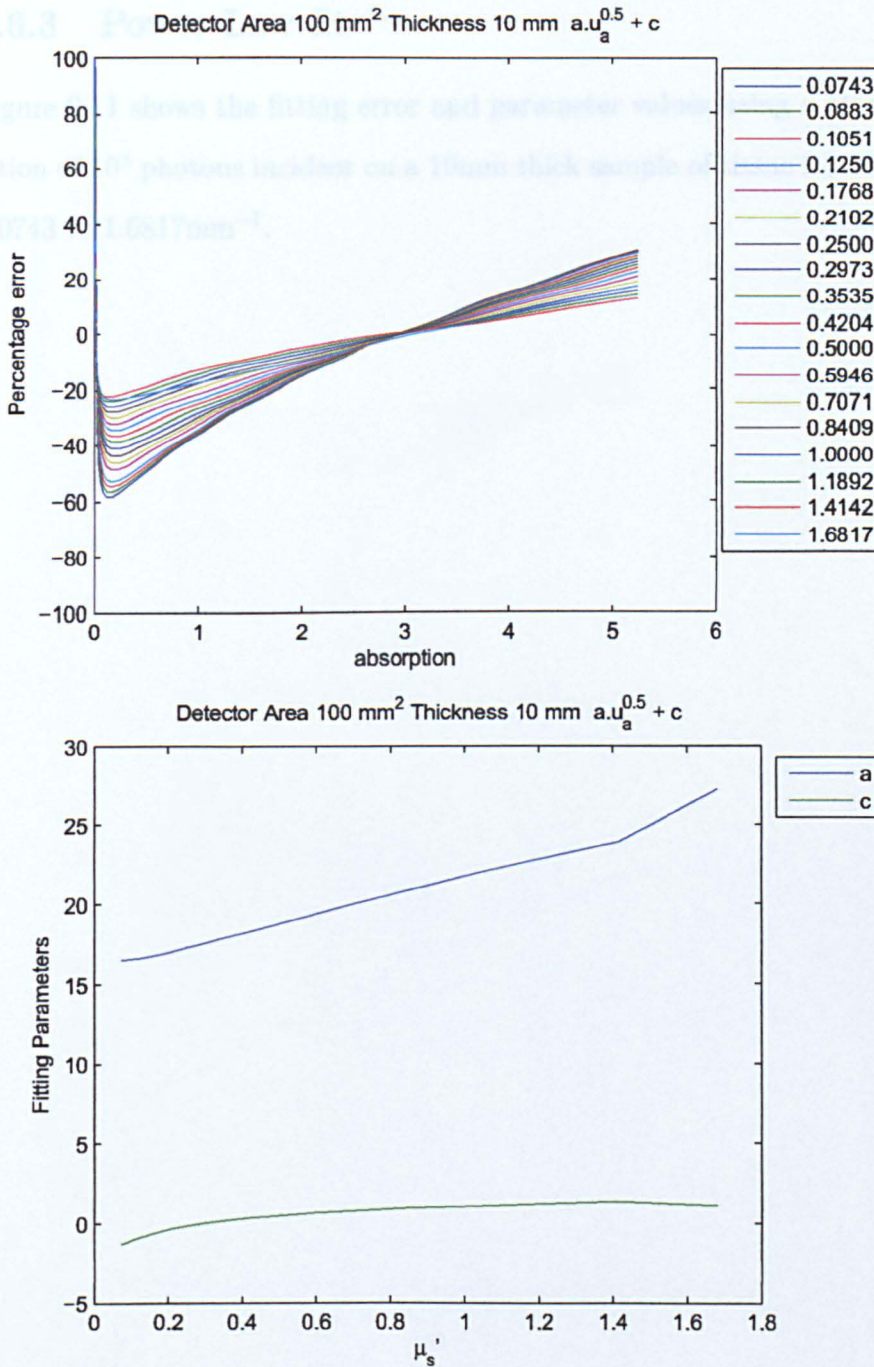


Figure 2.10: Fitting parameters, Photon Diffusion Theory fit using a Monte Carlo simulation 10^8 photons incident on a 10mm thick sample of tissue for 18 values from μ'_s 0.0743 to 1.6817mm^{-1}

2.6.3 Power Law fit

Figure 2.11 shows the fitting error and parameter values using a Monte Carlo simulation of 10^8 photons incident on a 10mm thick sample of tissue for 18 values from μ'_s 0.0743 to 1.6817mm^{-1} .

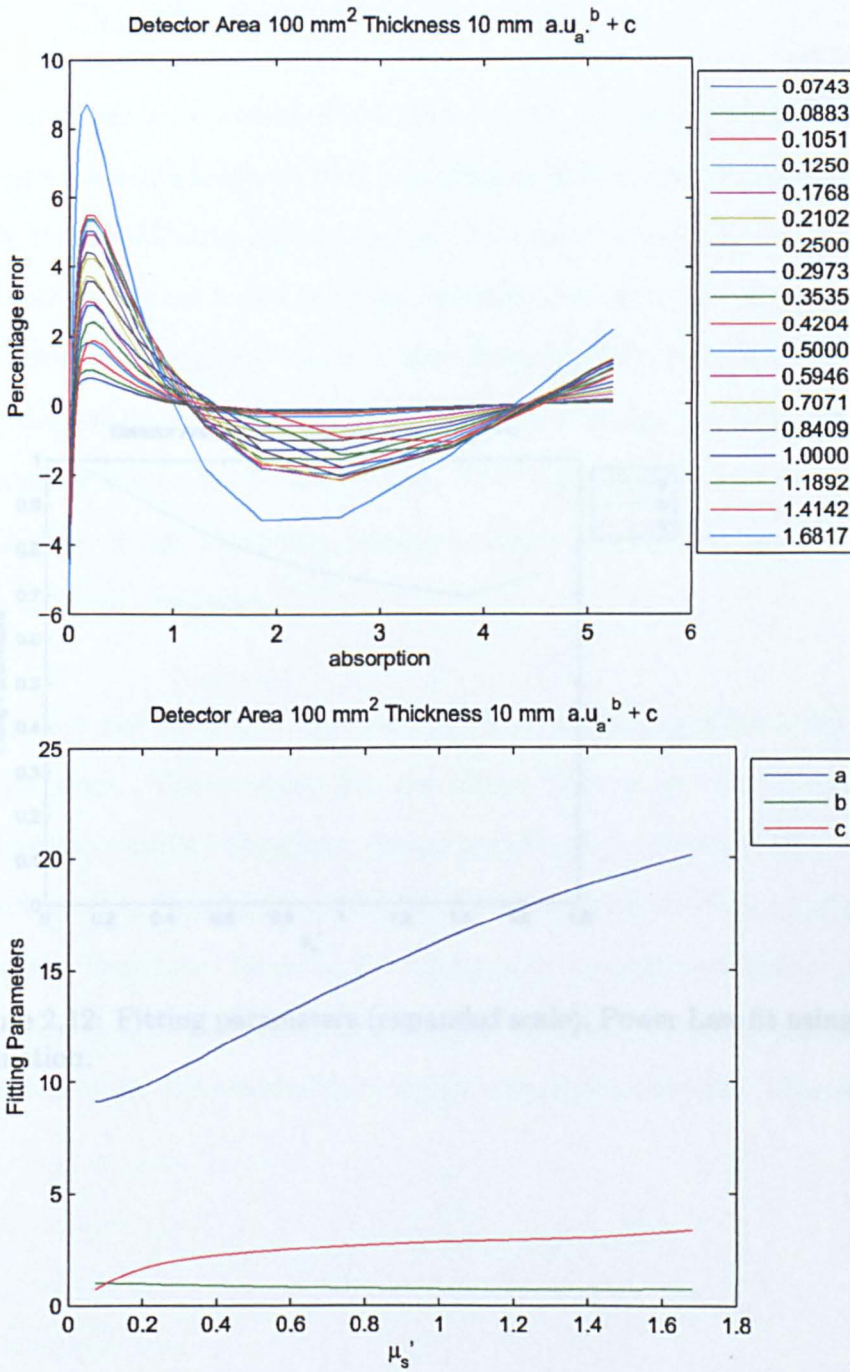


Figure 2.11: Fitting parameters, Power Law fit using a Monte Carlo simulation 10^8 photons incident on a 10mm thick sample of tissue for 18 values from μ'_s 0.0743 to 1.6817mm^{-1} .

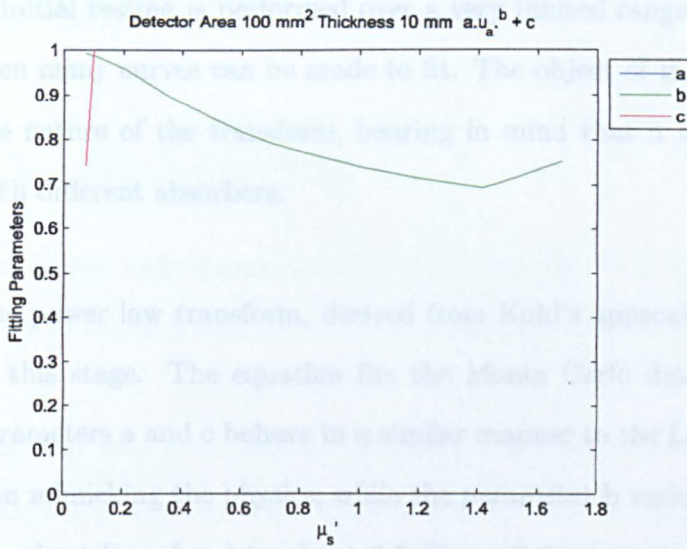
2.7 Conclusion

The error has a maximum of 6% (figure 2.11), at low absorptions compared with a fitting error using Lambert Beer plus offset of 40% at low absorptions (figure 2.9) and 60 % for the diffusion approximation. This test fits are over a much wider range of absorptions the are found in tissue, however they serve to demonstrate the shape of the fitting curve and are useful in identifying the best candidate for detailed testing.

If initial tests are promising, a detailed range of absorption and scattering then a fit can be made to it. The degree of detail was to understand the nature of the transform, bearing in mind that it could be used in other media with different absorbers.

The power law transform, derived from Kohl's approximation is the best candidate at this stage. The equation fits the Monte Carlo data with this least error. The parameters a and c behave in a similar manner to the Lambert Beer plus offset equation (Lambert Beer Law) to about 2.7 (figure 2.7: expanded parameter plot). The error

Figure 2.12: Fitting parameters (expanded scale), Power Law fit using a Monte Carlo simulation.



2.7 Conclusion

The error has a maximum of 9% (figure 2.11), at low absorptions compared with a fitting error using Lambert Beer plus offset of 40% at low absorptions (figure 2.9) and 60 % for the diffusion approximation. This test fits are over a much wider range of absorptions the are found in tissue, however they serve to demonstrate the shape of the fitting curve and are useful in identifying the best candidate for detailed testing. If initial testing is performed over a very limited range of absorption and scattering then many curves can be made to fit. The object of this exercise was to understand the nature of the transform, bearing in mind that it could be used in other media with different absorbers.

The power law transform, derived from Kohl's approximation is the best candidate at this stage. The equation fits the Monte Carlo data with this least error. The parameters a and c behave in a similar manner to the Lambert Beer plus offset equation mimicking the physics, while the parameter b varies from 1.0 with no scattering (Lambert Beer Law) to about 0.7 (figure 2.12 expanded parameter plot). The error is the lowest achieved so far, low enough to proceed with more detailed work over the expected range of absorption and oxygen saturation recovery (Chapter 3).

Chapter 3

Oximetry using Power Law Transform

3.1 Introduction

The power Law transform, chapter 2, was shown to have an error of $\pm 4\%$ in the range of interest, and a so is a good candidate for oxygen saturation recovery.

The next step is to generate a model of the attenuation surface (figure 3.1) to test oximetry using the power law transform. The surface is defined by a set of Monte Carlo simulations (section 3.1.1). To test the accuracy of oxygen saturation recovery the following sets of data are required:

- 1.The attenuation surface (figure 3.1)
- 2.The extinction spectra for Hb and HbO₂ (figure 3.1)
- 3.The assumed relationship between wavelength and scattering

Attenuation increase = $d\lambda + d_0$

3.1.1 The attenuation surface

To test the power law transform for oximetry, a set of Monte Carlo results were used to model the attenuation surface of tissue $\mu'_s = 1.0\text{mm}^{-1} \pm 20\%$ and $\mu_a = 0 - 0.3\text{mm}^{-1}$. This attenuation surface is shown in figure 3.1

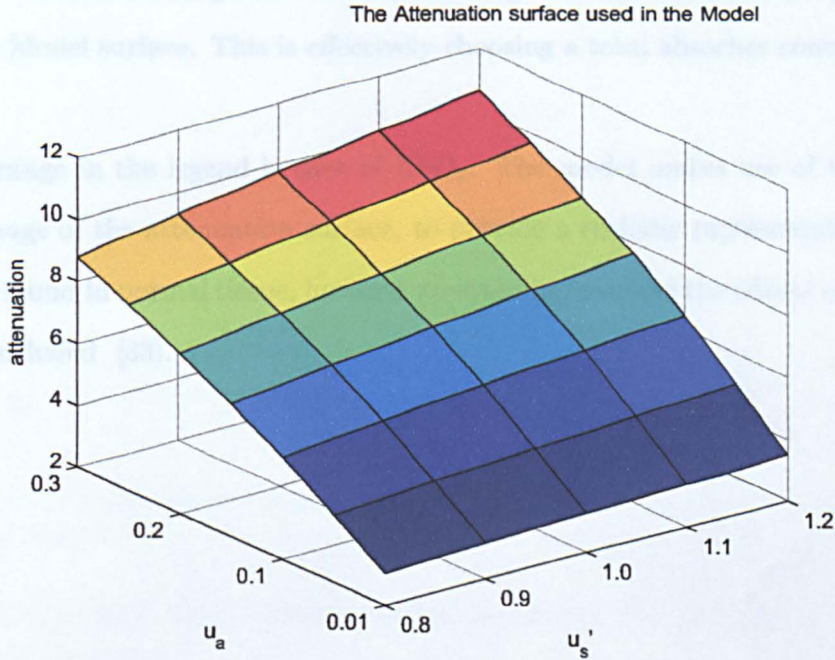


Figure 3.1: The Attenuation Surface used to test oxygen saturation recovery $\mu_a = 0.01 - 0.3 \text{ mm}^{-1}$ $\mu'_s = 0.8 - 1.2 \text{ mm}^{-1}$

3.1.2 The extinction spectra

The extinction spectra for Haemoglobin were compiled from standard results Oregon Medical Laser [32]. see figure 1.2

Figure 3.2 shows the resulting Attenuation spectra when a mixture of HbO_2 and

Hb (figure 1.2) is transformed by the Attenuation surface model (figure 3.1). That is each point on the absorption curve for the 11 chosen SO_2 values (0-100%), is transformed using the data in fig 3.1 by interpolation to give the Attenuation spectra in fig 3.2. The extinction curves are scaled so that the sum of any two points does not produce an absorption μ_a greater than 0.3 ensuring that the Attenuation Spectra are within the Model surface. This is effectively choosing a total absorber concentration.

The percentage in the legend is that of HbO_2 . The model makes use of the widest possible range of the attenuation surface, to provide a realistic representation of the worst case found in normal tissue, however no attempt to model the effects of melamin has been included [33].

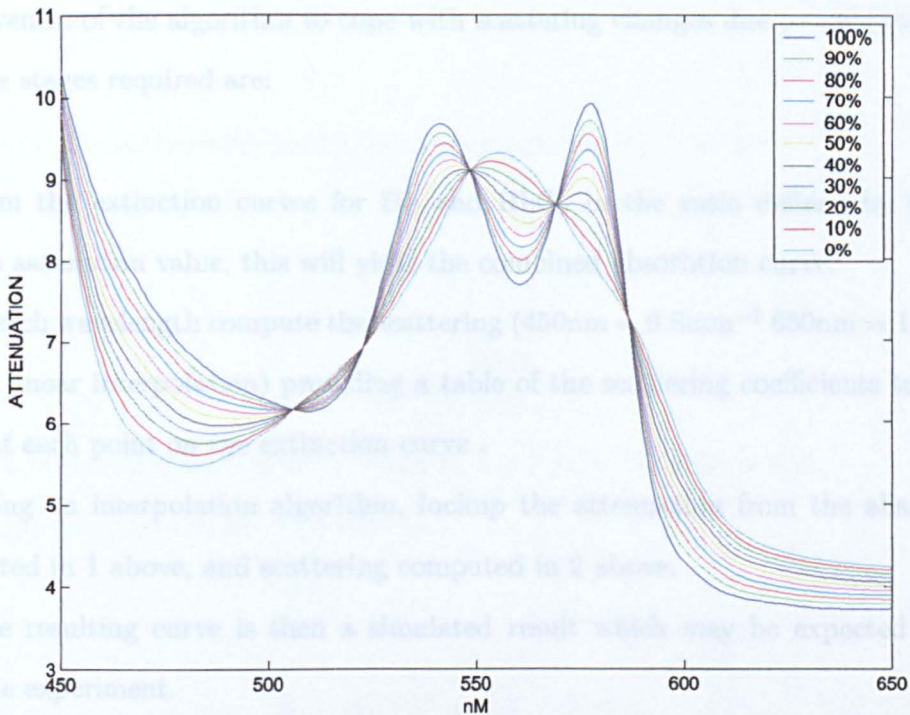


Figure 3.2: The Attenuation Spectra, for 11 percentages of oxygen saturation, using the Surface Model

3.1.3 Creating the attenuation spectra for a given oxygen saturation

The next step is to create a theoretical attenuation spectra from the Monte Carlo data, the wavelength factor, the extinction coefficients and a test oxygen saturation value. The simulation was designed to cover as much of the attenuation surface as possible, by ensuring the 100% oxygen saturation had a peak absorption of $0.3 \mu_a$, this effectively chooses the total haemoglobin to be that which has a peak absorption of $0.3 \mu_a$. The variation of scattering due to wavelength is assumed to be -20 % at 450nm and +20% at 650nm, this is a larger variation than reported [34], however using $\mu'_s = 1.0 \text{ mm}^{-1} \pm 20\%$ is more however this should serve to demonstrate the

effectiveness of the algorithm to cope with scattering changes due to wavelength.

The stages required are:

1. Sum the extinction curves for Hb and HbO₂ in the ratio defined by the test oxygen saturation value, this will yield the combined absorption curve.
2. for each wavelength compute the scattering (450nm = 0.8mm⁻¹ 650nm = 1.2mm⁻¹ with a linear interpolation) providing a table of the scattering coefficients to be applied at each point on the extinction curve .
3. Using an interpolation algorithm, lookup the attenuation from the absorption, computed in 1 above, and scattering computed in 2 above.
4. The resulting curve is then a simulated result which may be expected from a suitable experiment.

The simulated result is then used to test the transform and fitting procedure, if both are perfect the oxygen saturation should be recovered with no error.

3.1.4 Extracting the oxygen saturation from the spectra

When the simulated attenuation curve has been obtained we use the surface modelling formula to extract the SO₂ value and then compare it with the value modelled. First we calculate the total absorption in terms of SO₂ the oxygen saturation and T the total haemoglobin and hence the attenuation in the same terms

The total absorption μ_a is:

$$\mu_a = \alpha \text{HbO}_2(\lambda) + \beta \text{Hb}(\lambda) \quad (3.1.1)$$

Where:

$HbO_2(\lambda)$ is the extinction spectra for oxyhemoglobin $cm^{-1} \text{ mole}^{-1}$

$Hb(\lambda)$ is the extinction spectra for deoxyhemoglobin $cm^{-1} \text{ mole}^{-1}$

$$SO_2 = \frac{HbO_2}{T} \quad (3.1.2)$$

where T is the total haemoglobin which is $T = HbO_2 + Hb$ mole and

SO_2 is the oxygen saturation (0-100 %).

$$\mu_a = \alpha SO_2 T + \beta(T - HbO_2) \quad (3.1.3)$$

$$\mu_a = \alpha SO_2 T + \beta(T - ST) \quad (3.1.4)$$

$$\mu_a = [(\alpha - \beta)S + \beta] T \quad (3.1.5)$$

So the Attenuation for the Lambert-Beer plus offset transform is:

$$\mu_a = [(\alpha - \beta)S + \beta] T \quad (3.1.6)$$

The method can be demonstrated using figure 3.3. The attenuation spectra is top left, the extinction spectra for SO_2 bottom right, the fitted transform in the case $a\mu_a + c$ is top right. The fitting equation is:

$$A = aT((\text{HbO}_2(\lambda) - \text{Hb}(\lambda))\frac{S}{100} + \text{Hb}(\lambda)) + c \quad (3.1.7)$$

Where:

$\text{HbO}_2(\lambda)$ is the extinction spectra for oxyhemoglobin

$\text{Hb}(\lambda)$ is the extinction spectra for deoxyhemoglobin

$\text{HbO}_2(\lambda) - \text{Hb}(\lambda)$ is the difference of the two spectra

S is the oxygen saturation (0-100 %).

a is the mean path length

c is the loss due to scattering

T is the total haemoglobin

The fit is performed with a non-linear search algorithm that uses the simplex search method [35]. This is a direct search method that does not use numerical or analytic gradients. For n unknown parameters, of the fitting equation, the simplex in n -dimensional space is characterized by the $n+1$ distinct vectors that are its vertices. In two-space, a simplex is a triangle; in three-space, it is a pyramid. At each step of the search, a new point in or near the current simplex is generated. The function value at the new point is compared with the function's values at the vertices of the simplex and, usually, one of the vertices is replaced by the new point, giving a new simplex. This step is repeated until the diameter of the simplex is less than the specified tolerance.

In this simple case there is only one non-linear parameter, the oxygen saturation S . Once this has been estimated the linear parameters are found by matrix inversion. The simplex search requires an estimate for each search parameter in this case $S = 50\%$. Iterations continue until a preset least square error is attained or a maximum number of cycles of iteration is reached. The method has been used for all the transform equations in this work. The method can be used with any transform and extended to 3 or more absorbing species (see later sections).

In figure 3.3 the top right hand plot is the transform from the absorption spectrum (lower right) to the attenuation spectrum (top left). The blue transform is required to map absorption to attenuation with no errors. The red line is the actual transform fitted by the non-linear search, this best fit results in an oxygen saturation error of about 12 % and is the worst case presented simply to demonstrate the method. Note only the simulation and the archived transform are normally presented to keep the graphics uncluttered.

3.2 Applying the method to the Power Law transform

Equation 3.1 can be modified to implement the Power Law transform:

$$A = a \left[\frac{S}{100} (\mu_{a,SO_2}(\lambda) - \mu_{a,H_2O}(\lambda) + D) + c \right] \quad (3.2)$$

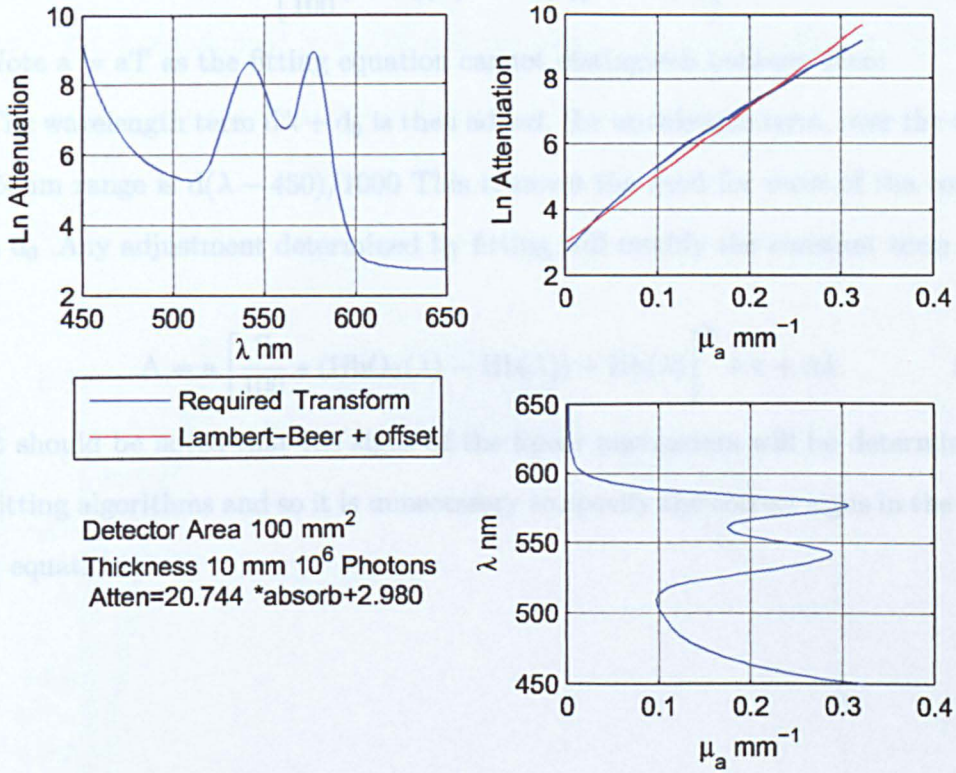


Figure 3.3: Extracting SO₂ using $a\mu_a + c$ top left - the modelled measured spectrum, top right the required transform (blue) and the Lambert-Beer Plus offset fit (red), bottom left - the transform, bottom right - the recovered spectra SO₂ = 88%

3.2 Applying the method to the Power Law transform

Equation 3.1 can be modified to implement the Power Law transform thus:

$$A = a \left[\frac{S}{100} (\text{HbO}_2(\lambda) - \text{Hb}(\lambda)) + \text{Hb}(\lambda) \right]^b + c \quad (3.2.1)$$

Note $a = aT$ as the fitting equation cannot distinguish between them

The wavelength term $d\lambda + d_0$ is then added, the wavelength term, over the 450nm to 650nm range is $d(\lambda - 450)/1000$ This removes the need for most of the constant term d_0 .Any adjustment determined by fitting will modify the constant term c .

$$A = a \left[\frac{S}{100} * (\text{HbO}_2(\lambda) - \text{Hb}(\lambda)) + \text{Hb}(\lambda) \right]^b + c + d\lambda \quad (3.2.2)$$

It should be noted that the signs of the linear parameters will be determined by the fitting algorithms and so it is unnecessary to specify the correct signs in the transform equations.

3.2.1 Range and accuracy of fit

This section shows the results obtained using the transform on a range of modelled spectra from 0 - 100% SO₂. The fitting error of the transform to the Monte Carlo data is shown in figure 3.4, Figure 3.5 shows the range of fitting parameters for a wide range of scattering coefficients. The error in the accuracy of recovered oxygen saturation is demonstrated in fig 3.6 and the plots of parameter values in figure 3.7.

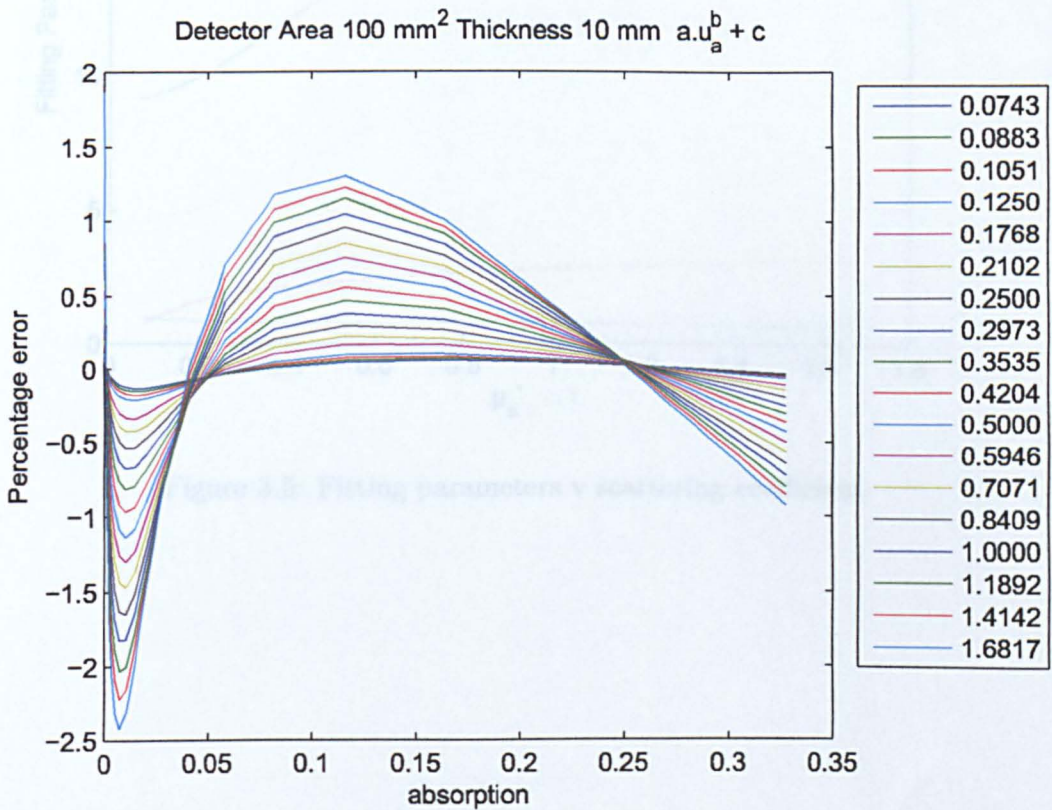


Figure 3.4: Error in fit over the absorption range μ_a 0 - 0.3 mm⁻¹ v scattering coefficient μ_s 0.0743 - 1.6817 mm⁻¹

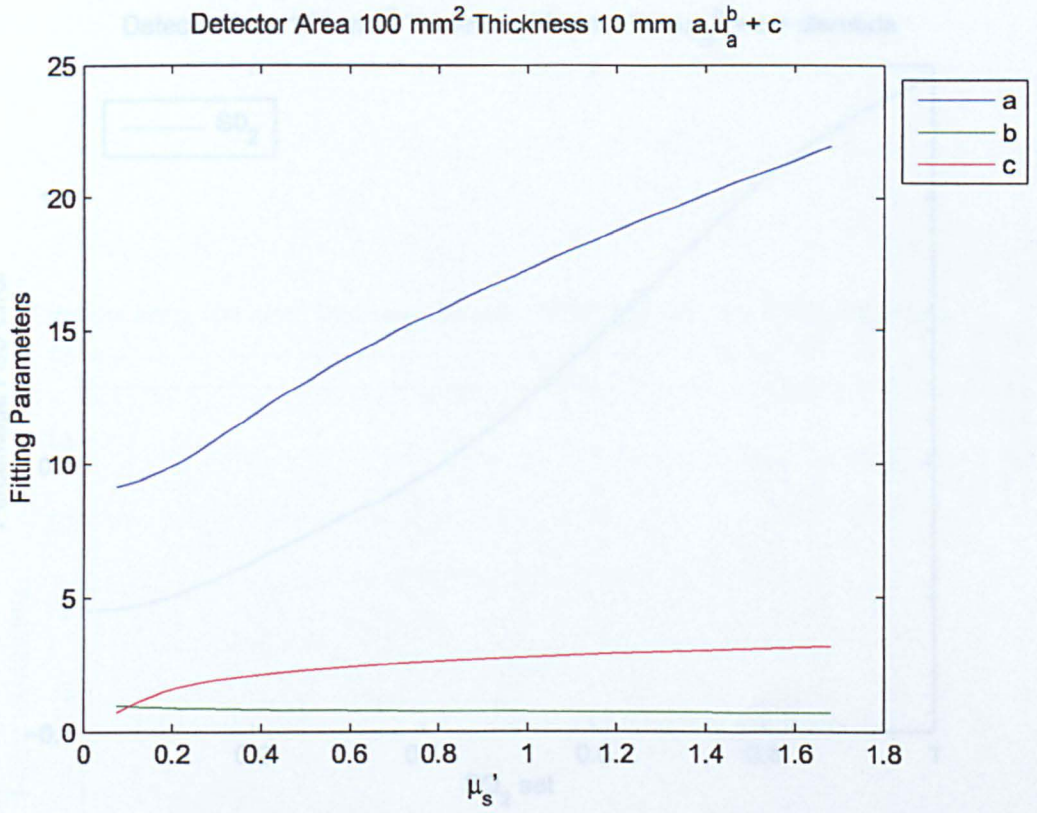


Figure 3.5: Fitting parameters v scattering coefficient

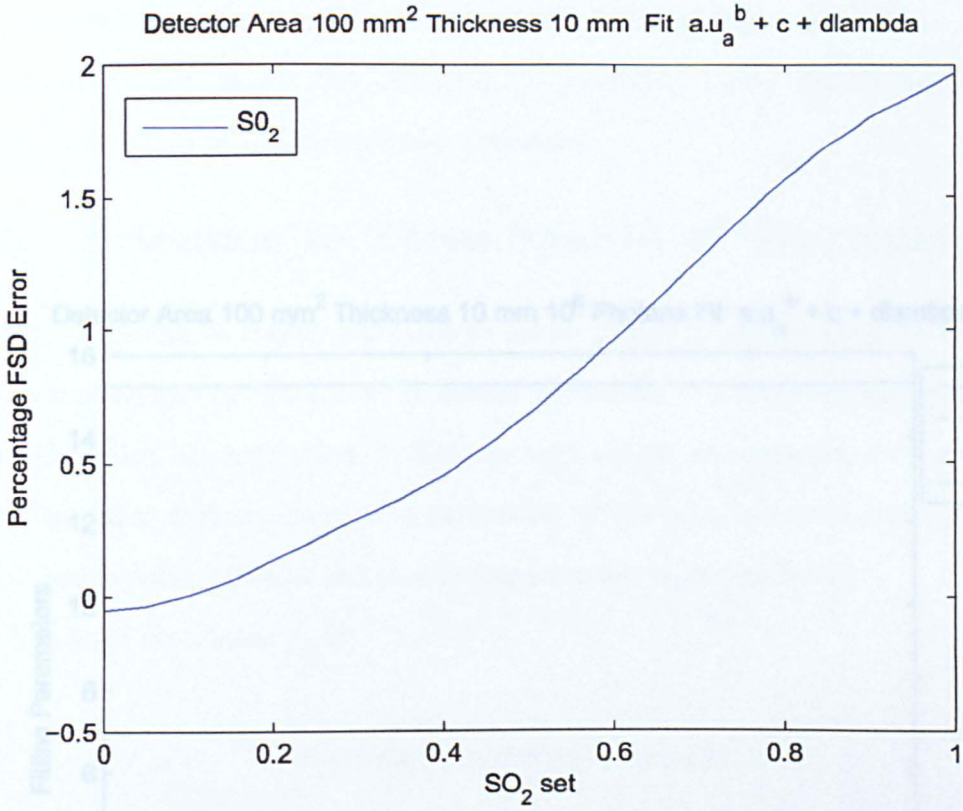


Figure 3.6: Error in recovered SO₂ v SO₂ set-point

Figure 3.7: Fitting parameters v SO₂ set-point

The error in recovered SO_2 is better than might be expected given the error in the transform and there is little change in the parameter values over the range of SO_2 which is desirable as it shows a stable transform.

3.3 Extension to Three Species of Haemoglobin

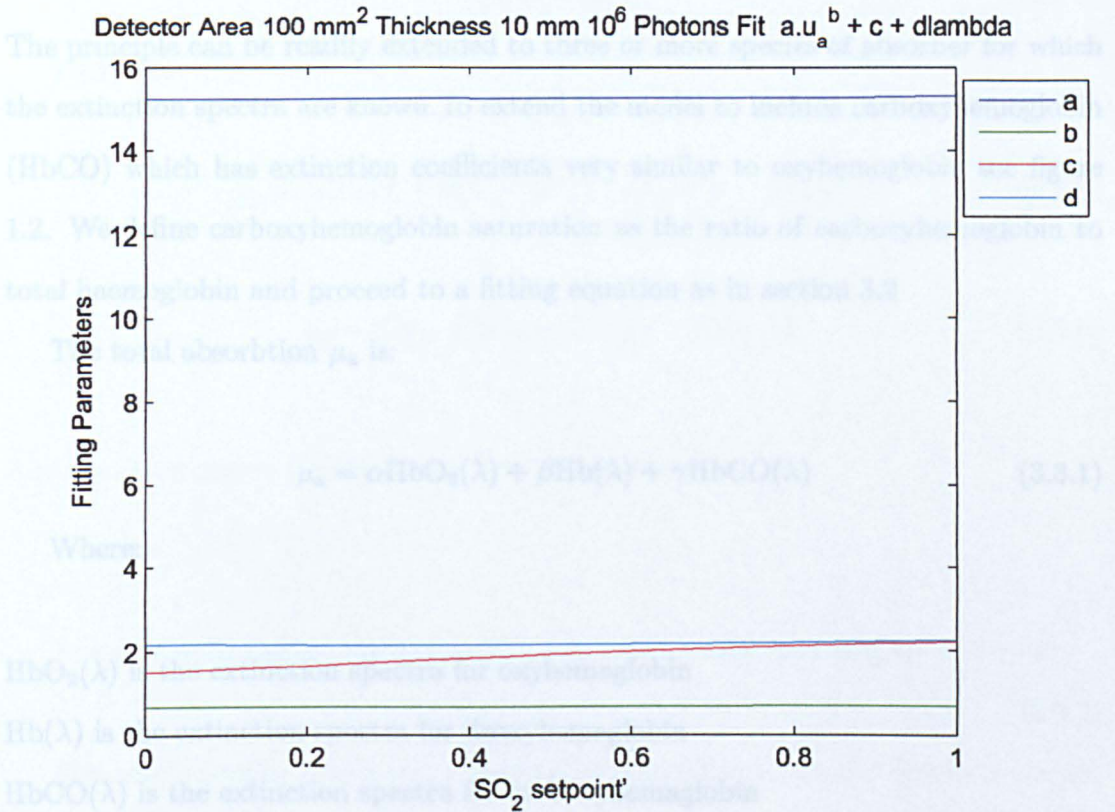


Figure 3.7: Fitting parameters v s SO_2 set-point

$$SO_2 = \frac{HbO_2}{T} \quad (3.3.2)$$

where T is the total haemoglobin which is $T = HbO_2 + Hb + HbCO$

The error in recovered SO_2 is better than might be expected given the error in the transform and there is little change in the parameter values over the range of SO_2 which is desirable as it shows a stable transform.

3.3 Extension to Three Species of Haemoglobin

The principle can be readily extended to three or more species of absorber for which the extinction spectra are known. To extend the model to include carboxyhemoglobin (HbCO) which has extinction coefficients very similar to oxyhemoglobin see figure 1.2. We define carboxyhemoglobin saturation as the ratio of carboxyhemoglobin to total haemoglobin and proceed to a fitting equation as in section 3.2

The total absorbtion μ_a is:

$$\mu_a = \alpha HbO_2(\lambda) + \beta Hb(\lambda) + \gamma HbCO(\lambda) \quad (3.3.1)$$

Where:

$HbO_2(\lambda)$ is the extinction spectra for oxyhemaglobin

$Hb(\lambda)$ is the extinction spectra for deoxyhemaglobin

$HbCO(\lambda)$ is the extinction spectra for carboxyhemaglobin

$$SO_2 = \frac{HbO_2}{T} \quad (3.3.2)$$

where T is the total haemoglobin which is $T = HbO_2 + Hb + HbCO$

$$\mu_a = \alpha \text{SO}_2 \text{T} + \beta (\text{T} - \text{SO}_2 \text{T} - \text{HbCO}) + \gamma (\text{HbCO}) \quad (3.3.3)$$

Now

$$S_{\text{CO}} = \frac{\text{HbCO}}{\text{T}} \quad (3.3.4)$$

Therefore

$$\mu_a = \alpha \text{SO}_2 \text{T} + \beta (\text{T} - \text{SO}_2 \text{T} - S_{\text{CO}} \text{T}) + \gamma (S_{\text{CO}} \text{T}) \quad (3.3.5)$$

$$\mu_a = [(\alpha - \beta) \text{SO}_2 + \beta + (\gamma - \beta) S_{\text{CO}}] \text{T} \quad (3.3.6)$$

And the Attenuation for the Power Law transform is:

$$A = a [\text{SO}_2 (\text{HbO}_2(\lambda) - \text{Hb}(\lambda)) + S_{\text{CO}} (\text{HbCO}(\lambda) - \text{Hb}(\lambda)) + \text{Hb}(\lambda)]^b + c + d\lambda \quad (3.3.7)$$

This can be readily tested over a range of SO_2 and S_{CO} values the results presented are for the range:

$\text{SO}_2 = 0$ to 100% while $\text{HbCO} = 100$ to 0%.

The extinction spectra for HbO_2 and HbCO are close see figure 1.2 and so this set provides the worst errors.

3.3.1 Range and accuracy of fit using 3 species

The error in the accuracy of recovered oxygen saturation and carbon monoxide saturation S_{CO} are demonstrated in figure 3.8 and the plots of parameter values in figure 3.8.

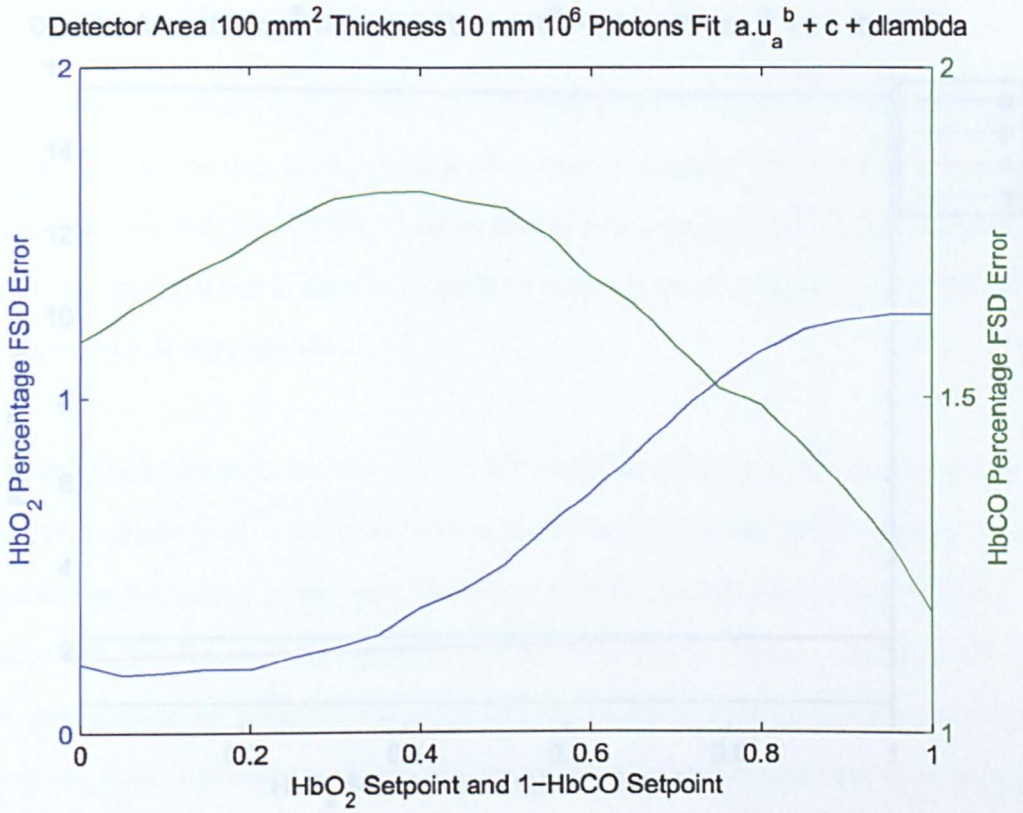


Figure 3.8: Error in recovered S_{O_2} and S_{CO} as S_{O_2} is increased to 100 % while S_{CO} is decreased from 0 to 100 %

3.3.2 Detector Area 100 mm² Thickness 10 mm 10⁶ Photons Fit $a.u_a^b + c + d\lambda$

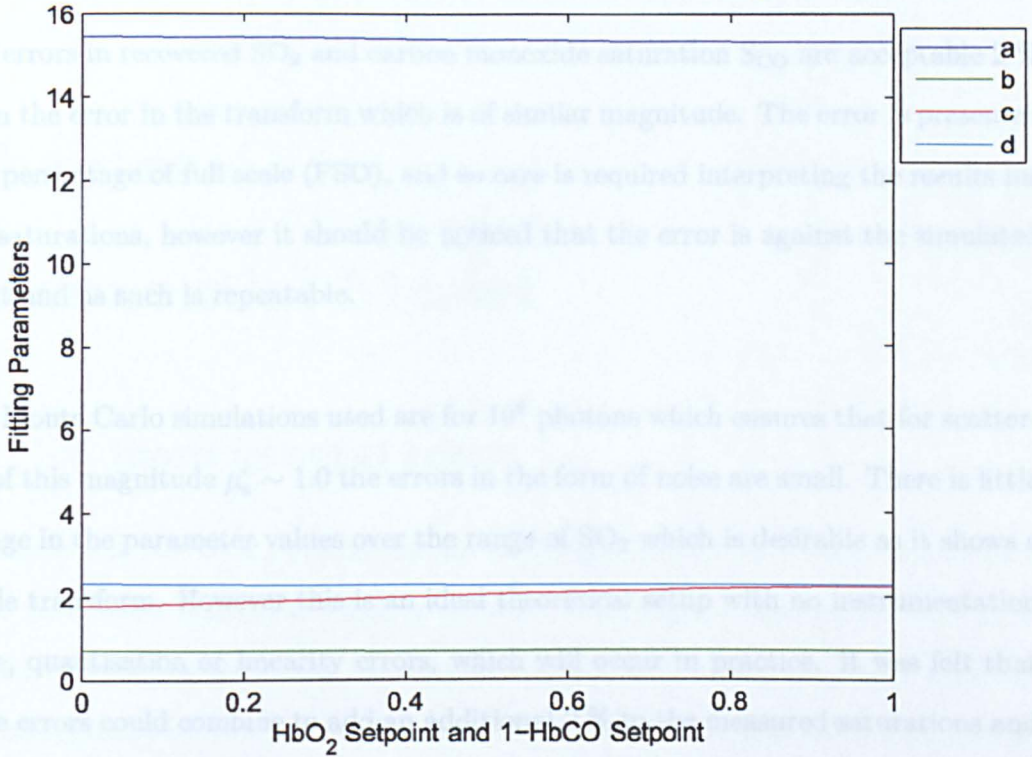


Figure 3.9: Fitting parameters v sSO₂ set-point

3.3.2 Discussion

The errors in recovered SO_2 and carbon monoxide saturation S_{CO} are acceptable 2 % given the error in the transform which is of similar magnitude. The error is presented as a percentage of full scale (FSD), and so care is required interpreting the results for low saturations, however it should be noticed that the error is against the simulated input and as such is repeatable.

The Monte Carlo simulations used are for 10^8 photons which ensures that for scattering of this magnitude $\mu'_s \sim 1.0$ the errors in the form of noise are small. There is little change in the parameter values over the range of SO_2 which is desirable as it shows a stable transform. However this is an ideal theoretical setup with no instrumentation noise, quantisation or linearity errors, which will occur in practice. It was felt that these errors could combine to add an additional 2 % to the measured saturations and therefore an more accurate transform was desirable.

A more accurate transform will also be required if the technique is to be used with other absorbers with a lower range of absorptions. The power law transform parameters do not readily map the scattering which could be offered by a more accurate transform. A long term objective would be to correct the measured attenuation for scattering to enable smaller concentrations of other absorbers to be identified.

The search for this transform is the subject of the next chapters, the techniques presented in this chapter have been used to test all the other transforms which have been developed and have proved excellent tools.

Chapter 4

Exponential Model

4.1 A more general result

In chapter 3 it was demonstrated that for spectrophotometry in a scattering medium to be accurate, a transform which is accurate in all regions especially at low μ_a is needed. The power law model matches the Monte Carlo results $\pm 1-2.5\%$, resulting in a maximum error of 2% SO_2 . This is a considerable improvement on the Lambert Beer with offset model, maximum error of 11% SO_2 .

The search for a transform, which fits the Monte Carlo data to 0.5% or better was undertaken to improve the accuracy of a practical instrument, and improve the modelling of the shape of the Monte Carlo data, an improvement that may be needed when attempting to map the scattering coefficient and hence correct the measured attenuation for scattering to enable smaller concentrations of other absorbers to be identified.

The search for this improved model proceeded as a theoretical study, in parallel with an heuristic search.

The mean flight time (first differential of Attenuation wrt μ_a) has an exponential form, which when integrated will lead to a model of the form:

$$\text{Attenuation} = ae^{-b\mu_a} + c \quad (4.1.1)$$

This model was not an improvement on the power law model, but led to the next model which formed the basis of all models used in this thesis and was eventually theoretically justified (see chapter 6).

$$\text{Attenuation} = ae^{-b\mu_a} - a_2e^{-b_2\mu_a} + c \quad (4.1.2)$$

This equation is used and developed in the rest of this thesis.

4.1.1 Error and Parameter plots general form

This equation fits with just over 5% error at $\mu_a = 0$ and is $\pm 2\%$ through most of the range of absorption $\mu_a = 0 - 6$.

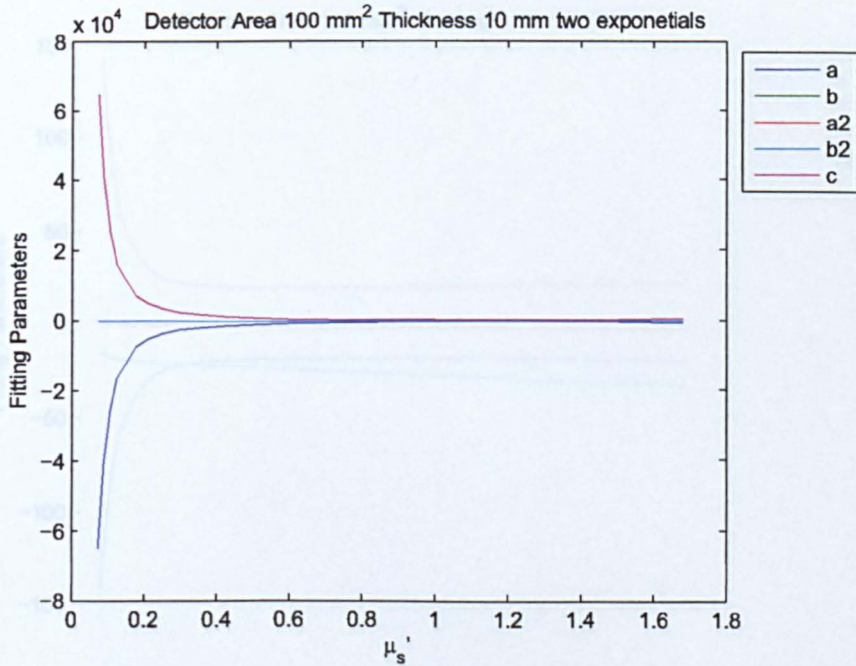
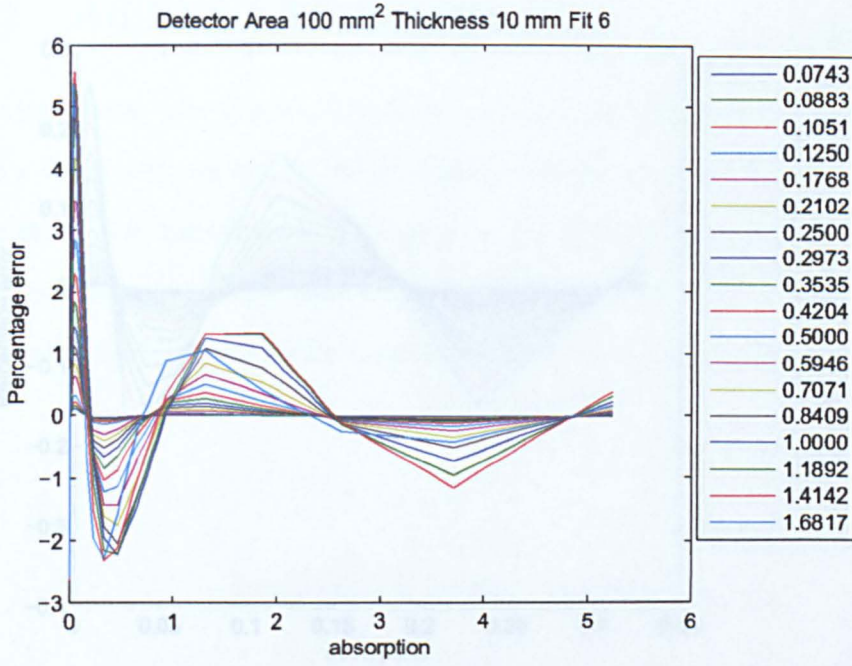


Figure 4.1: The Error and fitting parameters for the fitting equation $\text{Attenuation} = ae^{-b\mu_a} - a_2e^{-b_2\mu_a} + c$, for $\mu_a = 0 - 6\text{mm}^{-1}$

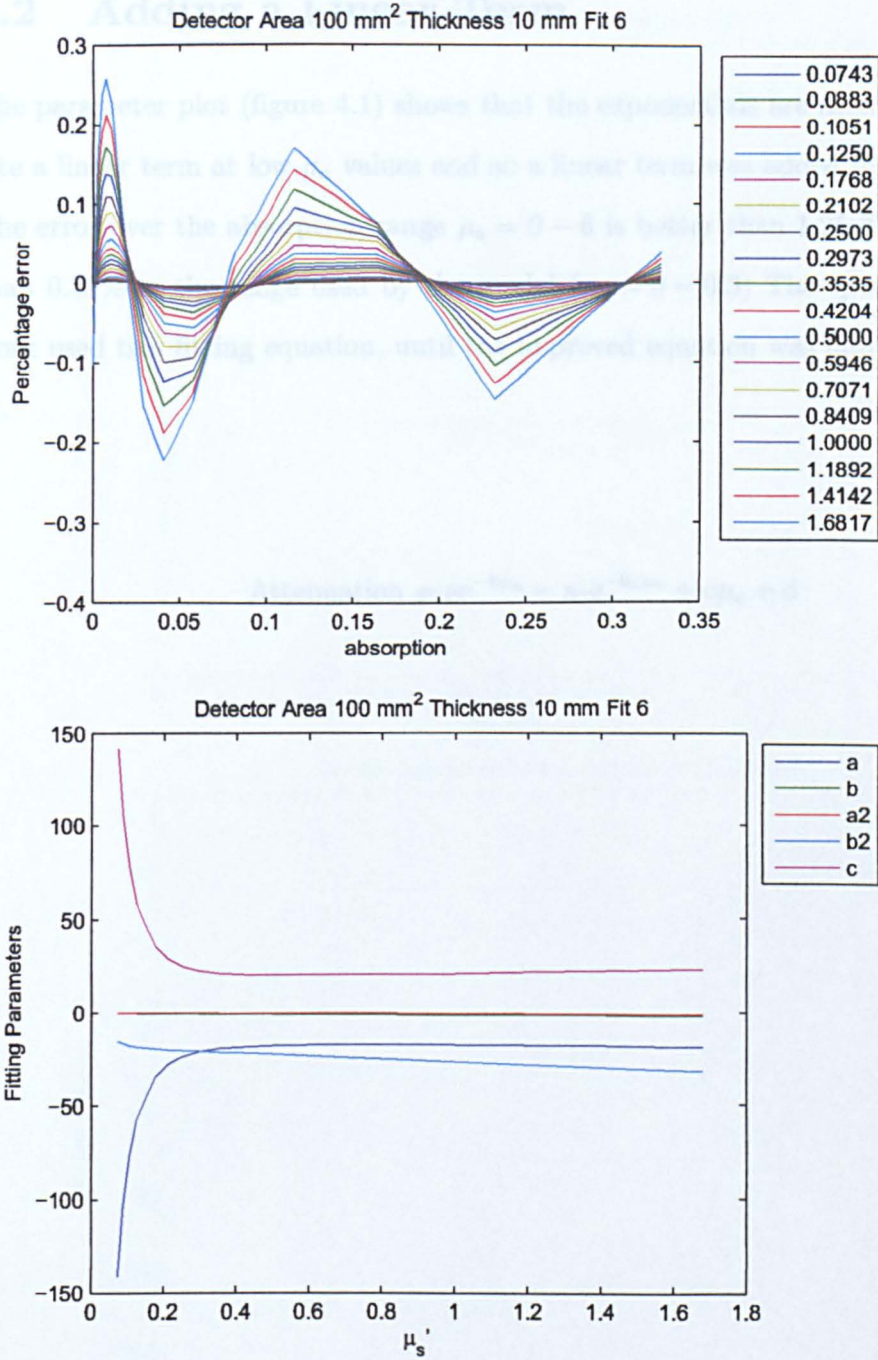


Figure 4.2: The Error and fitting parameters for the fitting equation $\text{Attenuation} = ae^{-b\mu_a} - a_2e^{-b_2\mu_a} + c$, for $\mu_a = 0 - 0.33\text{mm}^{-1}$

4.2 Adding a Linear Term

The parameter plot (figure 4.1) shows that the exponentials are attempting to emulate a linear term at low μ_a values and so a linear term was added to the transform. The error over the absorption range $\mu_a = 0 - 6$ is better than 1.25 %, and is better than 0.25% in the range used by the model ($\mu_a = 0 - 0.3$) The spectrophotometry work used this fitting equation, until the improved equation was developed (chapter 6).

$$\text{Attenuation} = ae^{-b\mu_a} - a_2e^{-b_2\mu_a} + c\mu_a + d \quad (4.2.1)$$

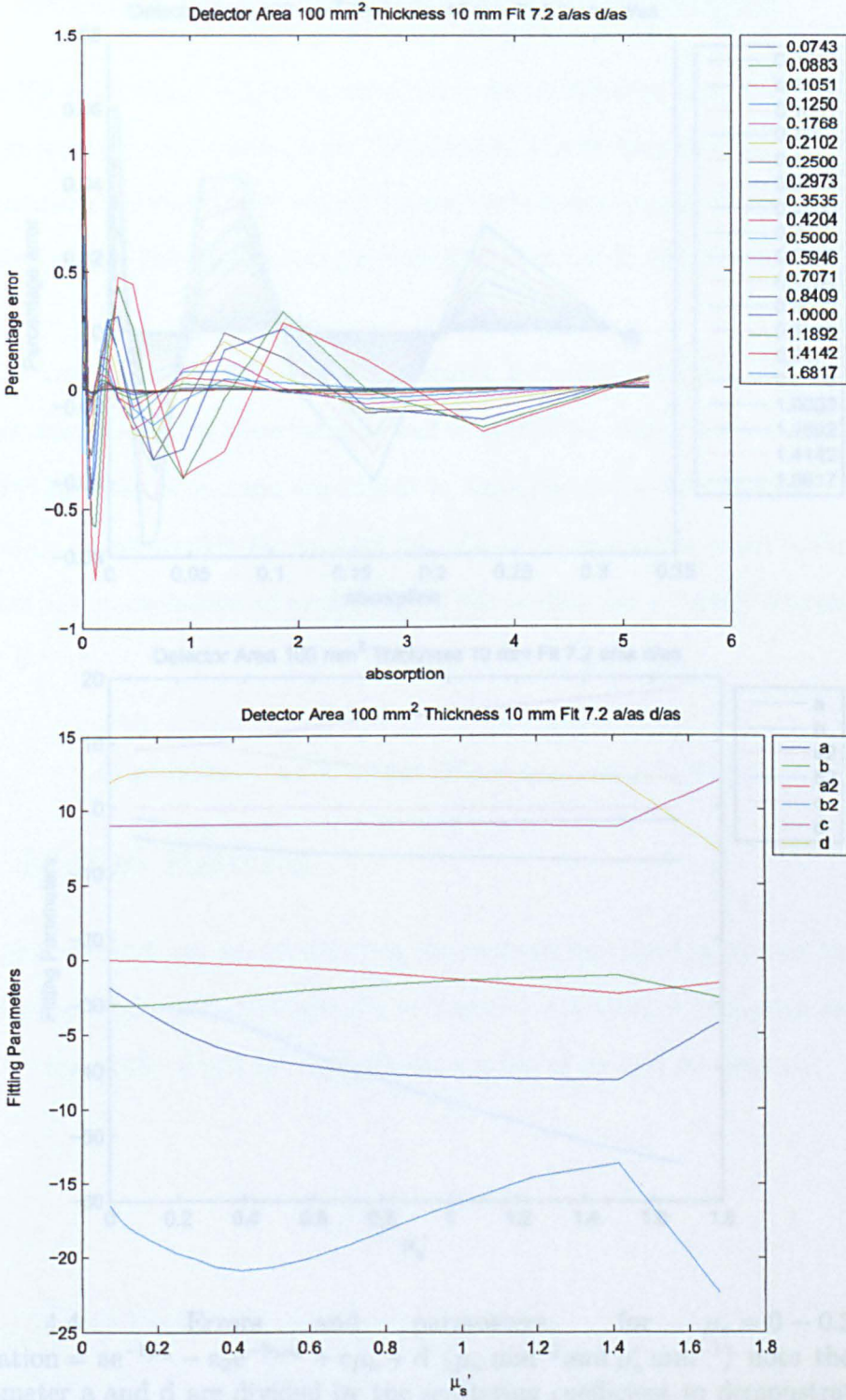


Figure 4.3: Errors and parameters, for $\mu_a = 0 - 6\text{mm}^{-1}$ Attenuation = $ae^{-b\mu_a} - a_2e^{-b_2\mu_a} + c\mu_a + d$ ($\mu_a \text{ mm}^{-1}$ and $\mu'_s \text{ mm}^{-1}$) note the values of parameter a and d are divided by the scattering coefficient to demonstrate there dependance on scattering.

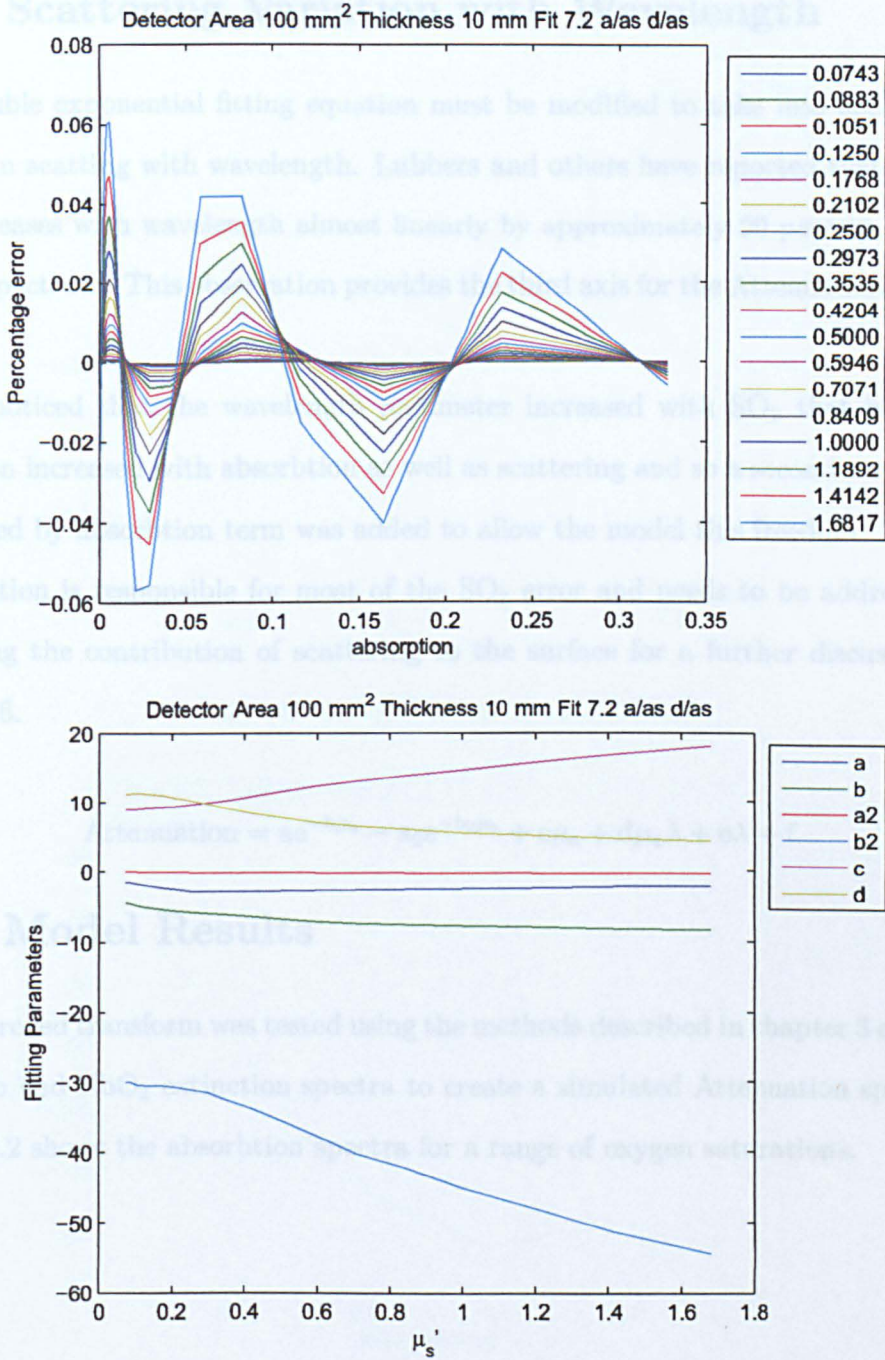


Figure 4.4: Errors and parameters, for $\mu_a = 0 - 0.33\text{mm}^{-1}$ Attenuation = $ae^{-b\mu_a} - a_2e^{-b_2\mu_a} + c\mu_a + d$ ($\mu_a \text{ mm}^{-1}$ and $\mu'_s \text{ mm}^{-1}$) note the values of parameter a and d are divided by the scattering coefficient to demonstrate there dependence on scattering.

4.3 Scattering Variation with Wavelength

The double exponential fitting equation must be modified to take into account the change in scattering with wavelength. Lubbers and others have reported that scattering decreases with wavelength almost linearly by approximately 20 percent over the visible spectrum. This observation provides the third axis for the Attenuation surface.

It was noticed that the wavelength parameter increased with SO_2 that is the attenuation increased with absorption as well as scattering and so a second wavelength multiplied by absorption term was added to allow the model this freedom. This approximation is responsible for most of the SO_2 error and needs to be addressed by modelling the contribution of scattering to the surface for a further discussion see chapter 6.

$$\text{Attenuation} = ae^{-b\mu_a} - a_2e^{-b_2\mu_a} + c\mu_a + d\mu_a\lambda + e\lambda + f \quad (4.3.1)$$

4.4 Model Results

The improved transform was tested using the methods described in chapter 3 equation using Hb and HbO_2 extinction spectra to create a simulated Attenuation spectrum. Figure 4.2 shows the absorption spectra for a range of oxygen saturations.

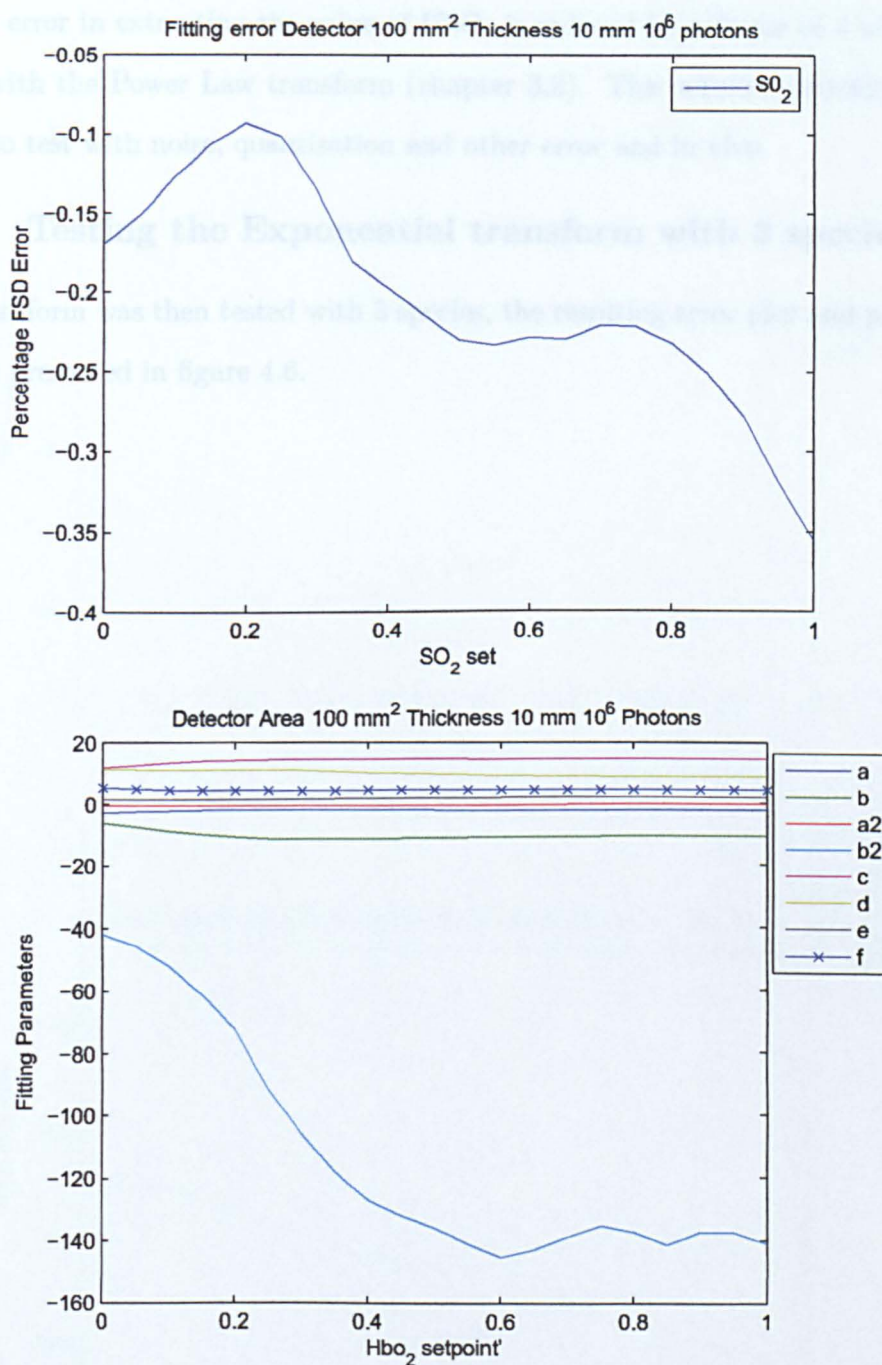


Figure 4.5: The Error and fitting parameters for So_2 recovery, using the model, $Attenuation = ae^{-b\mu_a} - a_2e^{-b_2\mu_a} + c\mu_a + d\mu_a\lambda + e\lambda + f$

The error in extracting the value of HbO_2 is reduced by a factor of 4 when compared with the Power Law transform (chapter 3.2). This solution provides a good model to test with noise, quantization and other error and in vivo.

4.4.1 Testing the Exponential transform with 3 species

The transform was then tested with 3 species, the resulting error plot and parameter plot are presented in figure 4.6.

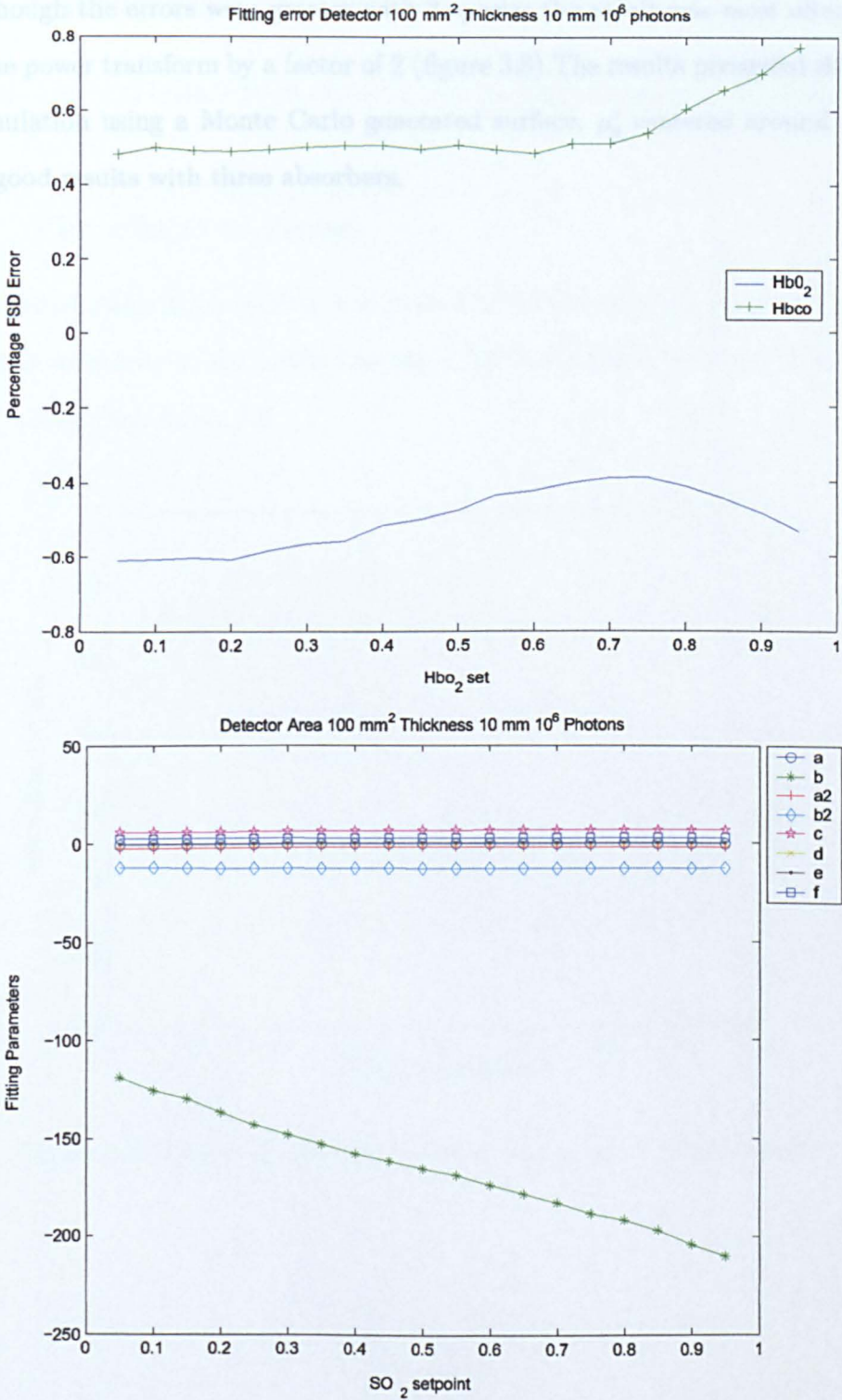


Figure 4.6: The Error and fitting parameters with SO₂ and S_{CO}

Although the errors were greater with 3 species the result was most often better than the power transform by a factor of 2 (figure 3.8). The results presented show that the simulation using a Monte Carlo generated surface, μ'_s centered around 1.0, produced good results with three absorbers.

4.5 Noise and Quantization Errors

Detector noise and quantization errors in the spectrophotometer both introduce errors.

4.5.1 The effects of Noise

The modelled attenuation spectra was passed to a Poisson noise generator, in order to test the sensitivity of the method to noise. The technique proved to be insensitive as can be seen from figure 4.6

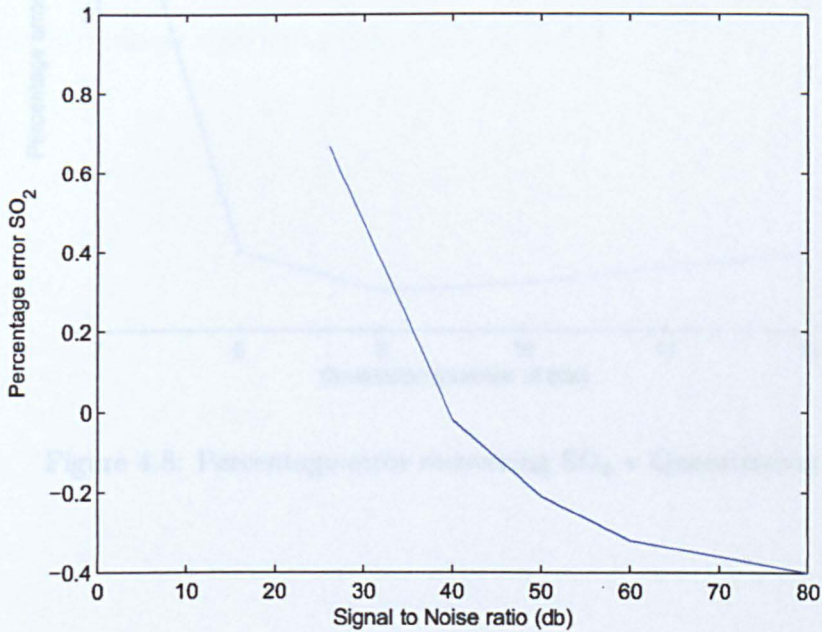


Figure 4.7: Percentage error recovering SO₂ v signal to noise ratio

4.5.2 The Effects of Quantisation

A measured attenuation spectra (chapter 5.1) was subjected to quantisation in order to test the sensitivity of the method to the resolution of the measuring system. The technique proved to be insensitive as can be seen from figure 4.7

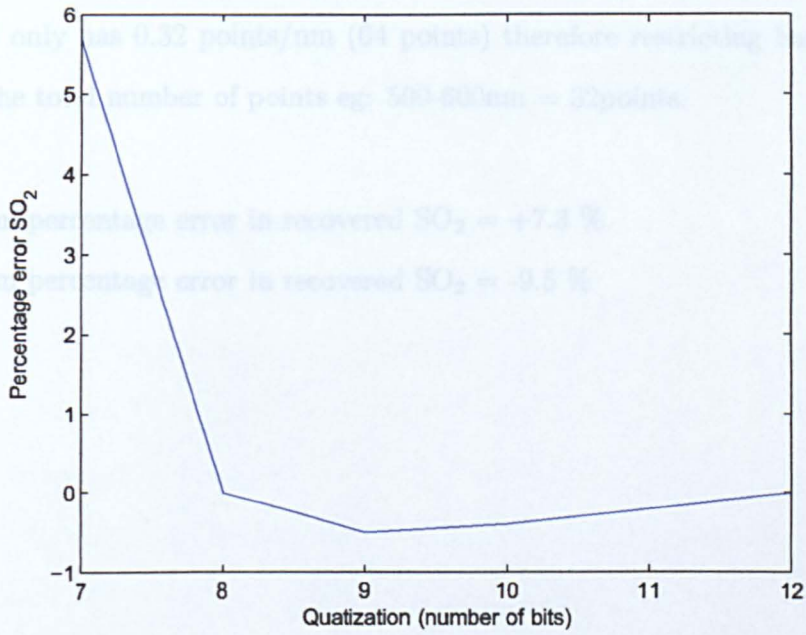


Figure 4.8: Percentage error recovering SO₂ v Quantisation

4.5.3 Bandwidth

When testing the method with restricted band width, it was found necessary to balance the restriction at the higher wavelengths with an equal restriction at lower wavelengths in order to obtain a reasonable fit. It should be born in mind that the measured attenuation spectra used is the same as for the quantisation tests in section 4.5.2 and only has 0.32 points/nm (64 points) therefore restricting bandwidth also reduces the total number of points eg: 500-600nm = 32points.

480-620nm percentage error in recovered SO_2 = +7.3 %

500-600nm percentage error in recovered SO_2 = -9.5 %

4.5.4 Wavelength Interval

Reducing the number of points, by removing the even number points to increase the interval to 0.64 (32 points) and again to 1.28 points/nm 16 points, the results are shown in figure 4.8 for 16,10 and 8 bit quantisation.

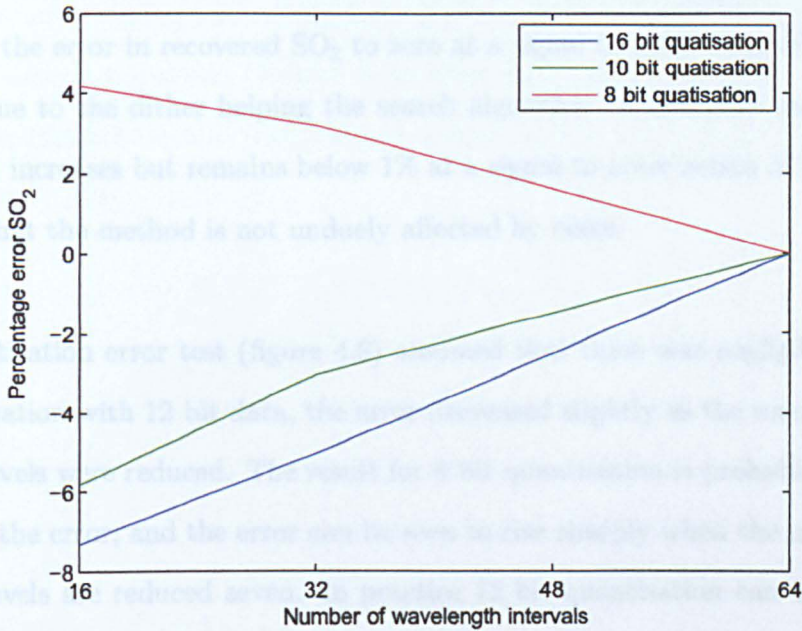


Figure 4.9: Percentage error recovering SO₂ v Quantisation

4.6 Conclusion

The recovery of SO_2 , accuracy 0.4 % and the recovery of SO_2 and SCO demonstrate that the exponential transform is a worthy candidate for further testing.

The introduction noise to the modelled attenuation spectrum (figure 4.7) is initially to reduce the error in recovered SO_2 to zero at a signal to noise ratio of 40db, which may be due to the dither helping the search algorithm to minimise the error. The error then increases but remains below 1% at a signal to noise ratio of 26db demonstrating that the method is not unduely affected by noise.

The quantisation error test (figure 4.8) assumed that there was negligible error due to quantisation with 12 bit data, the error decreased slightly as the number of quantisation levels were reduced. The result for 8 bit quantisation is probably the change in sign of the error, and the error can be seen to rise sharply when the number quantisation levels are reduced seven. In practice 12 bit quantisation can be considered the minimum, however signal levels may be below full scale, this test demonstrates the need to maintain signal levels above the 8 bit quantisation level.

Significant errors were found (section 4.5.3) when the measured attenuation bandwidth was reduced, the reasons for this will lie in the reduction of information, the range of absorption covered by the reduced bandwidth data will adversely affect the search algorithms ability to pick the correct transform, leading to errors in recovered SO_2 .

The number of wavelength intervals also adversely affects SO_2 recovery, figure 4.9 shows the effect for 3 levels of quantisation. Reducing the number of intervals does not decrease the bandwidth but significantly increases the error for all 3 quantisations.

These results demonstrate the bandwidth and wavelength interval required for experimental work, and provide guide lines for the signal levels required and the noise level that can be tolerated. Chapter 5 presents SO_2 measurements in vivo and SO_2 maps using this exponential transform to analyze images from a hyper-spectral camera.

Chapter 5

Experimental Confirmation

5.1 Introduction

To confirm the theoretical work experimentally, a spectrometer and probe (section 5.2), of a hyper-spectral imaging system (section 5.3) is required to measure the reflectance spectra of the tissue under examination. The raw reflectance signal must then be calibrated against the reflectance signal from a 99 % reflectance standard and then analysed using the method demonstrated in chapter 4.

5.2 Results using an Ocean Optics USB 2000

Initial experimental work was carried out using an ocean optics USB 2000 [36], this miniature instrument has a pre-selected grating and was purchased pre-calibrated to provide a 400 - 700 nm spectral range to a resolution and accuracy better than 0.5 nm, at full signal the instrument offers a signal to noise ratio better than 250:1. The USB 2000 was used with an Ocean Optics R200-7 reflection probe which consists of a tight bundle of 7 200 μm diameter optical fibers in a stainless steel ferrule. There are 6 illumination fibers around 1 read fiber. This arrangement ensures that the distance between illumination fibre and read fiber is 1 fibre diameter or 200 μm .

5.2.1 Early in vivo data

Results are presented in fig 5.1 for two reflectance spectra take from (a) the author's left thumb and (b) and are just above a vien on the back of the authors right hand.

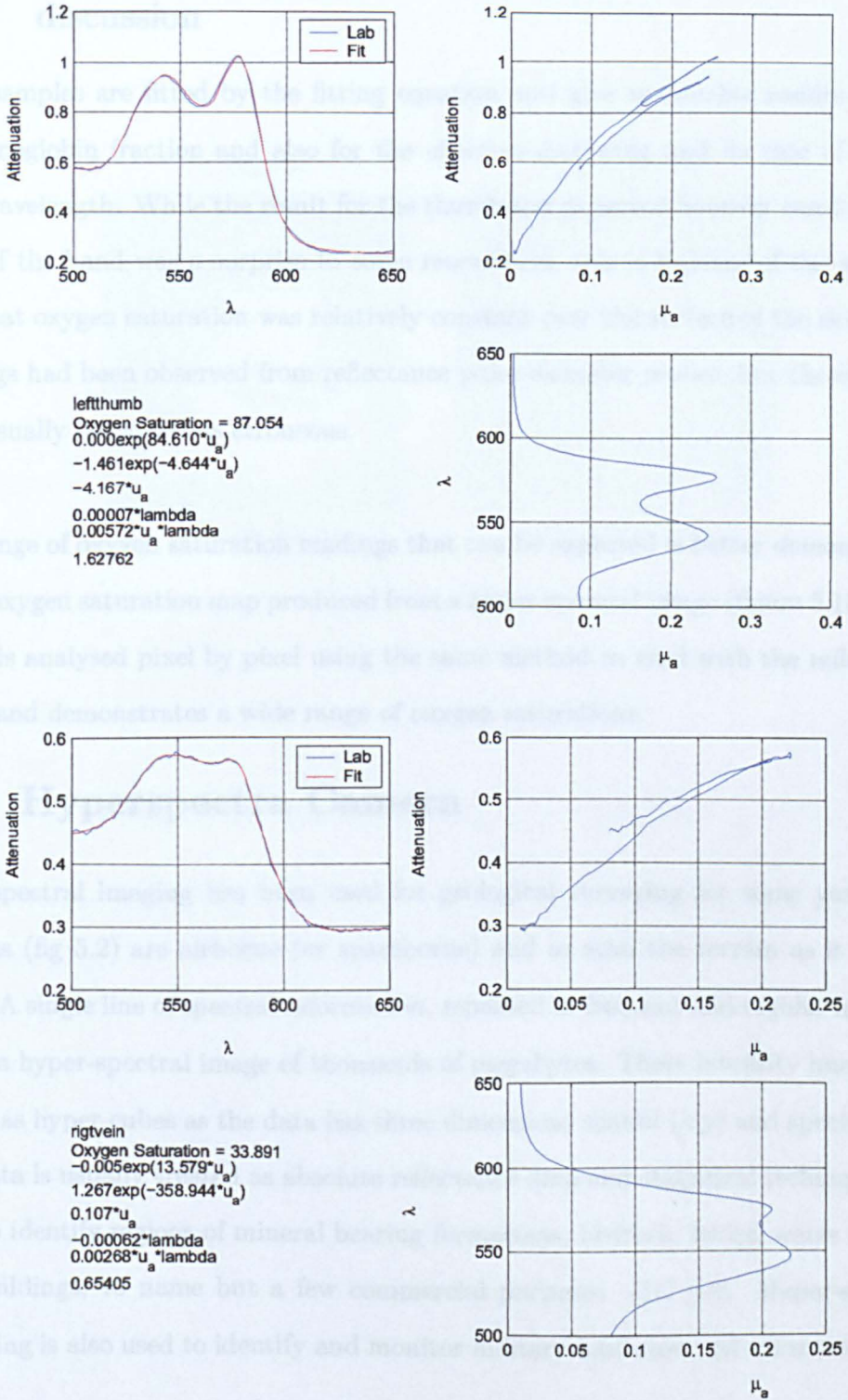


Figure 5.1: Fits obtained from The Left Thumb and A right vein on the back of the Right Hand, λ (nm), μ_a mm^{-1}

5.2.2 discussion

Both samples are fitted by the fitting equation and give reasonable results for the oxyhemoglobin fraction and also for the effective scattering and its rate of change with wavelength. While the result for the thumb was expected however result for the back of the hand was a surprise to some researchers, this is because of the assumption that oxygen saturation was relatively constant over the surface of the skin. Low readings had been observed from reflectance pulse oximeter probes, but these results were usually discarded as erroneous.

The range of oxygen saturation readings that can be expected is better demonstrated by an oxygen saturation map produced from a hyper-spectral image (figure 5.15). The image is analysed pixel by pixel using the same method as used with the reflectance probe and demonstrates a wide range of oxygen saturations.

5.3 Hyperspectra Camera

Hyperspectral imaging has been used for geological surveying for some years, the cameras (fig 5.2) are airborne (or spaceborne) and so scan the terrain as it is over flown. A single line of spectral information, repeated at frequent and regular intervals builds a hyper-spectral image of thousands of megabytes. These intensity images are known as hyper cubes as the data has three dimensions spatial (x,y) and spectral (λ). The data is usually treated as absolute reflectance data and statistical techniques are used to identify regions of mineral bearing formations, bedrock, faults, water courses and buildings, to name but a few commercial purposes [37] [38]. Hyper-spectral imaging is also used to identify and monitor military hardware and other resources.

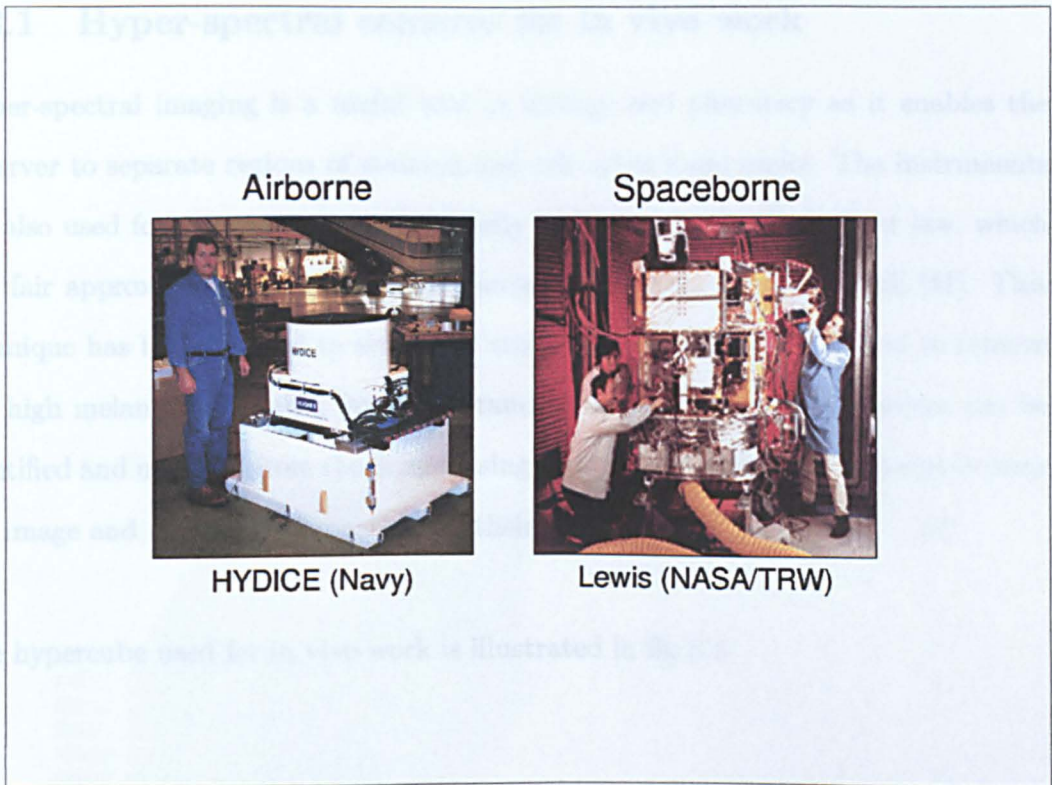


Figure 5.2: Traditional Hyper-spectral Cameras

The spaceborne instruments can be used to monitor cloud and other weather related formations [39].

5.3.1 Hyper-spectral cameras for in vivo work

Hyper-spectral imaging is a useful tool in biology and pharmacy as it enables the observer to separate regions of staining and cell types more easily. The instruments are also used for spectrophotometry usually assuming the Lambert Beer law, which is a fair approximation in the typical microscope transmission setup [40] [41]. This technique has been applied to sickle cell studies in which there is a need to remove the high melanin absorption from reflectance spectra. The melanin spectra can be identified and unmixed from the image, using statistical techniques, this helps to clear the image and allows other spectra and their distribution to be studied. [42]

The hypercube used for in vivo work is illustrated in fig 5.3.

Two types of instrument use in fact not recorded a full spectrum and makes use of mechanical scanning recording a line of the image with its spectrum for each scan, building up a 2D image over time as the scan progresses; this is a straight adaptation of the slit-scan technique [42]. The other uses variable band crystal filters through which a white-light image is taken. The filter scans through a range of wavelengths building up a spectrum line [43]. Both instruments suffer from motion artifacts, the scanning instrument is therefore somewhat more complex than the other and so is preferred for this work. The hyperspectral instrument is scanning the light

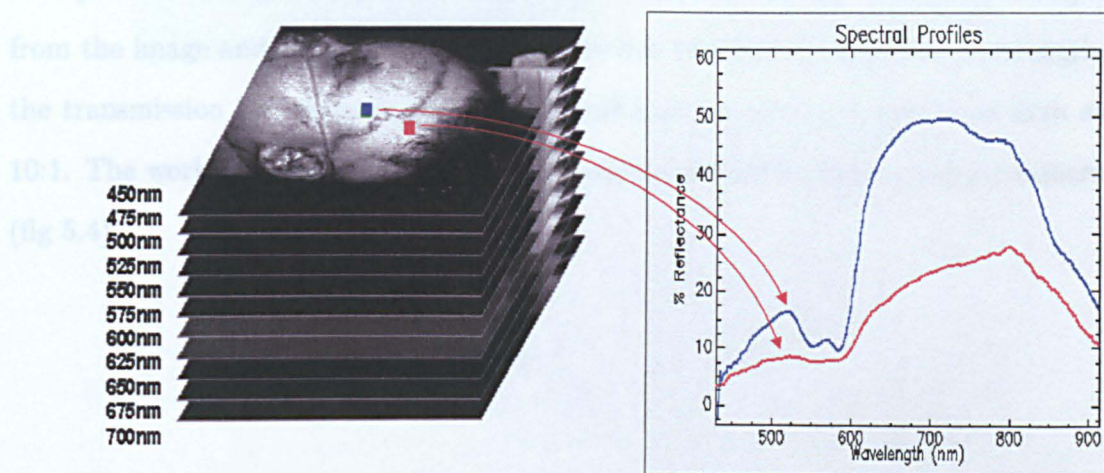


Figure 5.3: Hyper Stack
[43]

Two types of instrument are in use one recorded a full spectrum and makes use of mechanical scanning recording a line of the image with its spectrum for each scan, building up a 2D image over time as the scan progresses, this is a straight adaptation of the airborne instrument [43] [44]. The other uses tunable liquid crystal filters through which a complete image is taken, the filter scans through a range of wavelengths building a spectrum over time. [45] Both instruments suffer from motion artifacts, the scanning instrument is the more accurate, sensitive and lower noise and so is preferred for this work. The liquid crystal filters operate by polarizing the light from the image and then make use of interference to select a particular wavelength, the transmission loss depends on the bandwidth of the filter but can be as high as 10:1. The work reported in this chapter was done with a Provision scanning camera (fig 5.4).



- n camera configuration
 - n dynamic range: 12 bit (0 - 4095)
 - n spectral range: 430 - 919nm
 - n spectral resolution: 0.5nm
 - n filter: prism-grating-prism
 - n CCD: 1280x1024 (2/3 inch)

Figure 5.4

Figure 5.4

5.4 Experimental configuration

The camera setup is shown in (fig 5.4). The setup used for this experiment is a tungsten filament lamp, a lens, a prism-grating-prism filter, a lens, and a camera. These lamps have a spectrum which is continuous in the visible and near infrared. Also the camera and objective lenses are both illuminated with tungsten. The range of interest is 430-919nm and spectral resolution is 0.5nm. The changes in intensity in the filter/grating/prism assembly are measured and discussed in see fig 5.6.

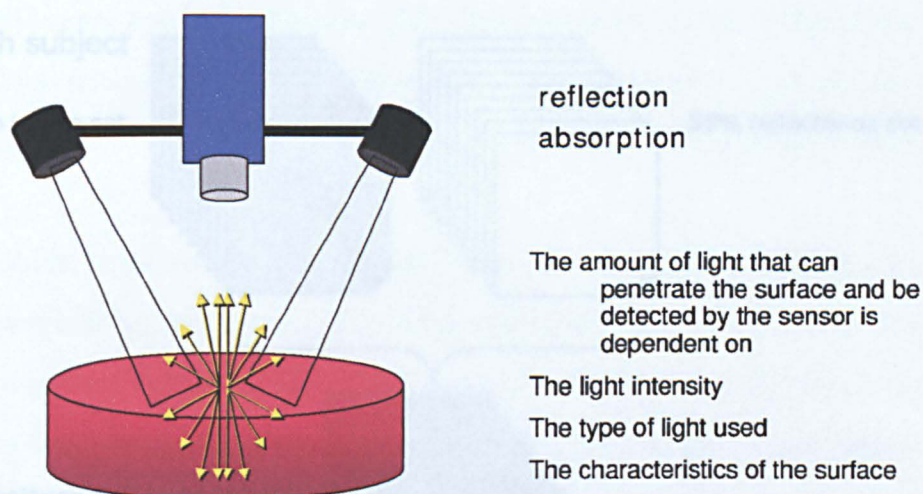


Figure 5.5: The Experimental Configuration

5.4 Experimental configuration

The camera setup is shown in (fig 5.5), the lamps used for the trials conducted to date are tungsten filament spot lights of the type used for home photography and movies. These lamps have a spectrum which is much more intense in the red (600-700nm) also the camera and diffraction grating are more efficient at these wavelengths. The range of interest is 450-650nm and so calibration must be used to remove the effects of changes in intensity in the illumination both spectrally and spatially in the response, see fig 5.6.

5.5 The Provision scanning Hyper visual imaging camera

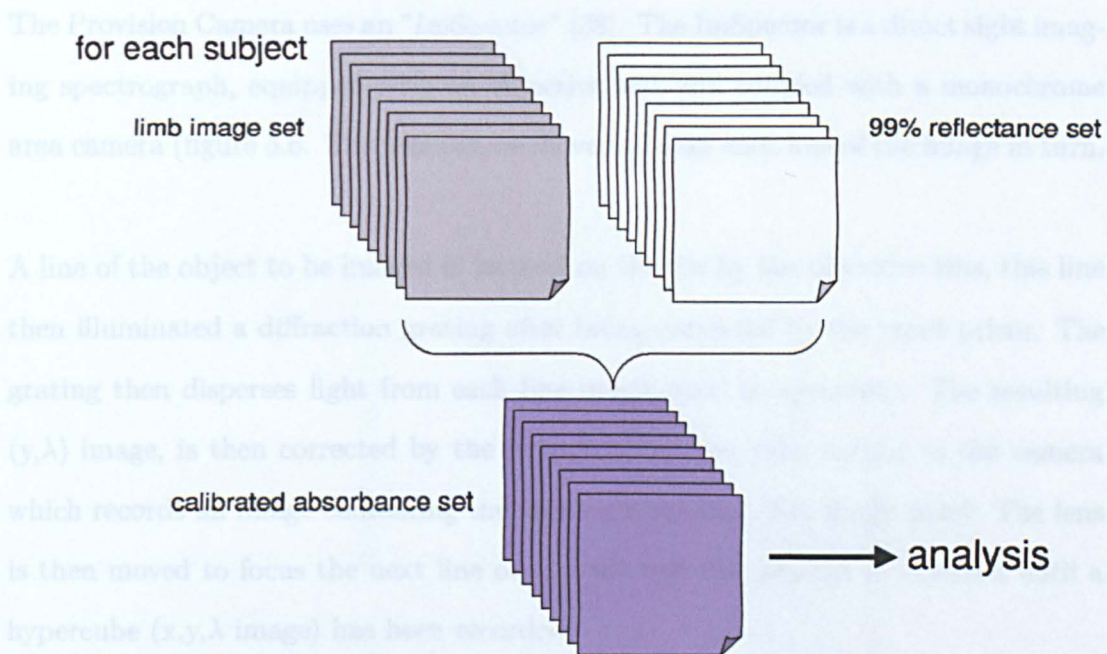


Figure 5.6: Trial data calibration

5.5 The Provision scanning Hyper visual imaging camera

The Provision Camera uses an "ImSpector" [38]. The ImSpector is a direct sight imaging spectrograph, equipped with an objective lens and coupled with a monochrome area camera (figure 5.6). The lens can be moved to scan each line of the image in turn.

A line of the object to be imaged is focused on the slit by the objective lens, this line then illuminates a diffraction grating after being corrected by the input prism. The grating then disperses light from each line image pixel to spectrum. The resulting (y,λ) image, is then corrected by the output prism and then output to the camera which records an image containing the spectrum for each line image pixel. The lens is then moved to focus the next line on the slit and this process is repeated until a hypercube (x,y,λ) image has been recorded.

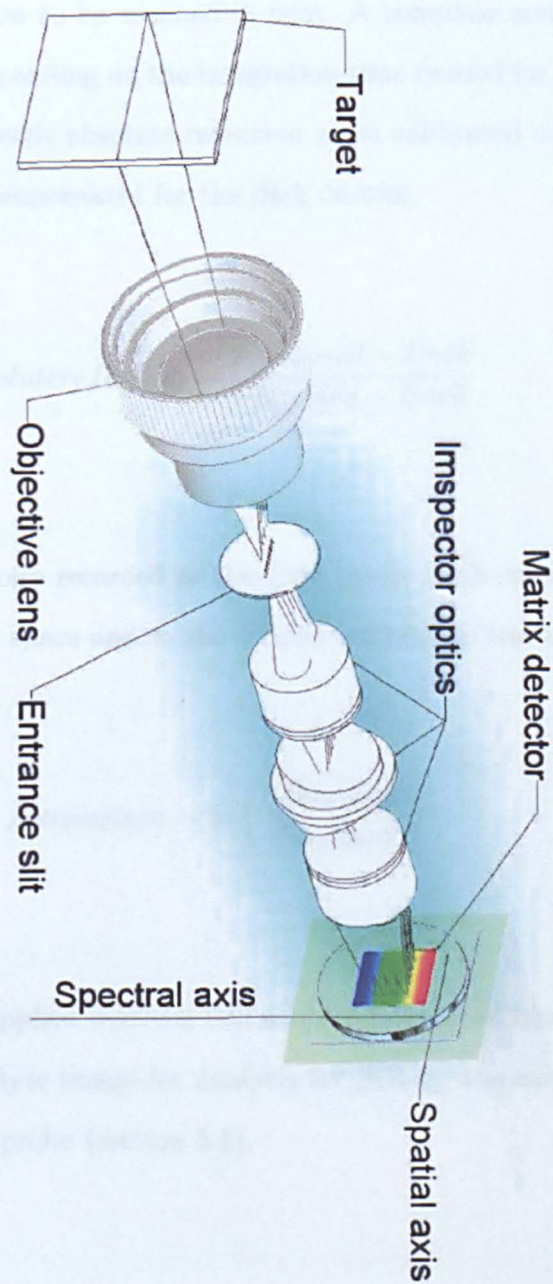


Figure 5.7: The ImSpector - direct sight imaging spectrograph

The 2D image has coordinates of X and λ . A mechanical scanner enables up to 500 lines in the Y direction to be scanned in turn. A complete scan takes approximately 5 - 250 seconds depending on the integration time needed for the illumination used. The instrument records absolute reflection when calibrated with a 98 percent reflection standard and compensated for the dark current.

$$\text{absolute reflection} = \frac{\text{Measured} - \text{Dark}}{\text{Standard} - \text{Dark}}$$

In practice the shot noise recorded as the dark image made no difference to the results in Optical Density space and so the simpler calibration was used.

$$\text{Attenuation} = \ln \left(\frac{\text{Measured}}{\text{Standard}} \right)$$

The ENVI software supplied with the HSI enables Regions of Interest (RoI) to be selected from the 300 MByte image for analysis for SO₂ by the same techniques as used with the reflectance probe (section 5.1).

5.6 Results from Lab on 28/11/03 at AstraZeneca

Presented below are a region of interest and analysis from one of the hand imaging experiments conducted at AstraZeneca using their Hyper Spectral Camera. The mean for the entire region of interest was taken and the scan time was 125 seconds (500 lines with an integration time of 250ms per line).

The instrument was found to have a λ shift which varied with position. This was detected from the illumination image (99% image) as the intensity of this image will change but not its spectra. This was a scanning fault which Provision eventually corrected. The fitting algorithm had to be modified to correct for an estimated λ shift (which could be as high as 4nm).

Presented in figures 5.8 to 5.13 are the regions of interest and analysis of 2 separate hand imaging experiments conducted at AstraZeneca using their Hyper Spectral Camera, by Vinod (AstraZeneca) and Paul (the author).

The setup included a Lee 061 gel Filter (Mist Blue), placed directly before the lens to reduce the high Red content of the illuminators and the high Red sensitivity of the silicon based CCD detector. A polariser was also placed before the lens to reduce the glare.

The images and analysis for the two experiments are reported below:

1. An image of Vinod's hand.
2. An image of Paul's hand.

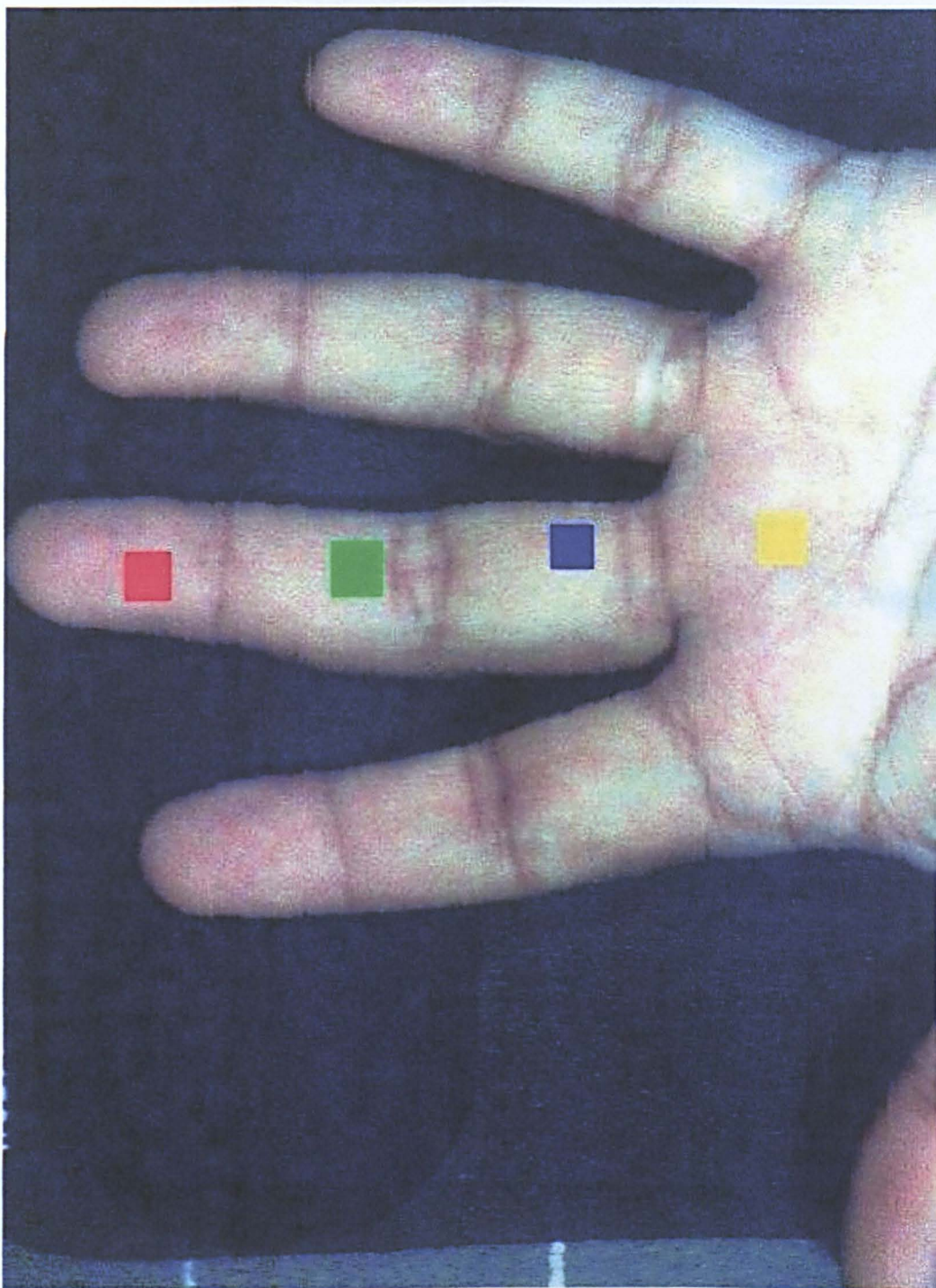


Figure 5.8: Vinod's hand image showing regions of interest

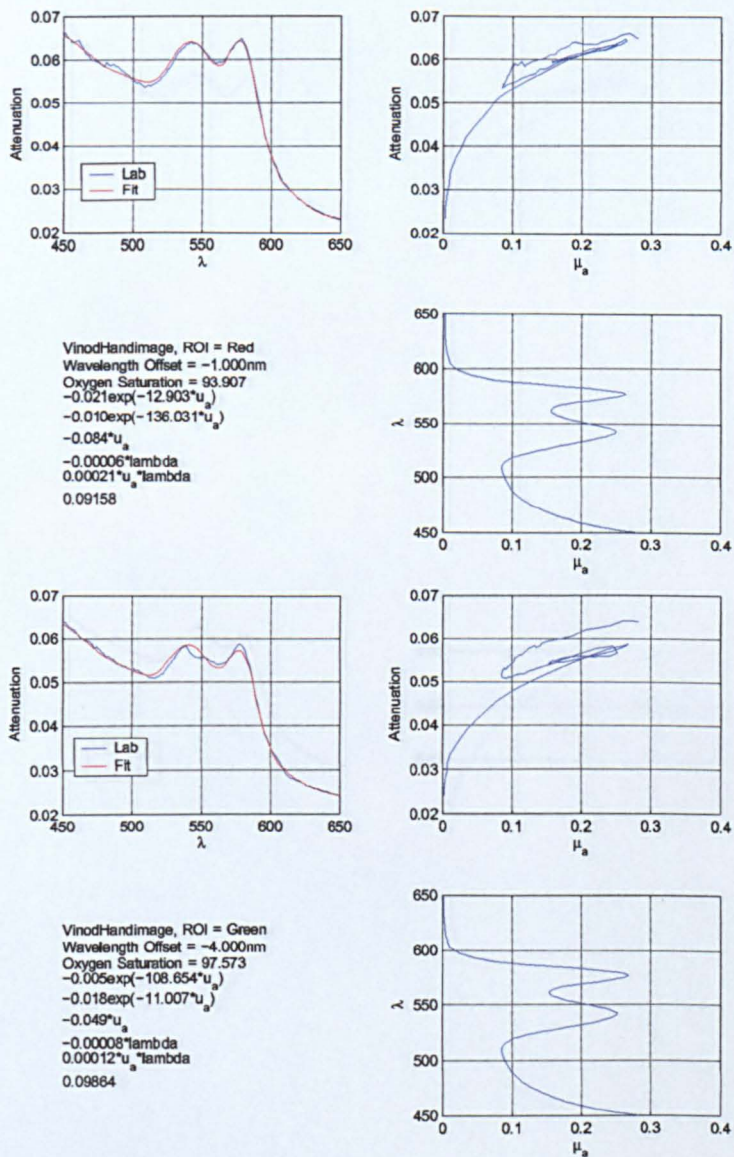


Figure 5.9: Analysis of Vinod's regions of interest Red and Green

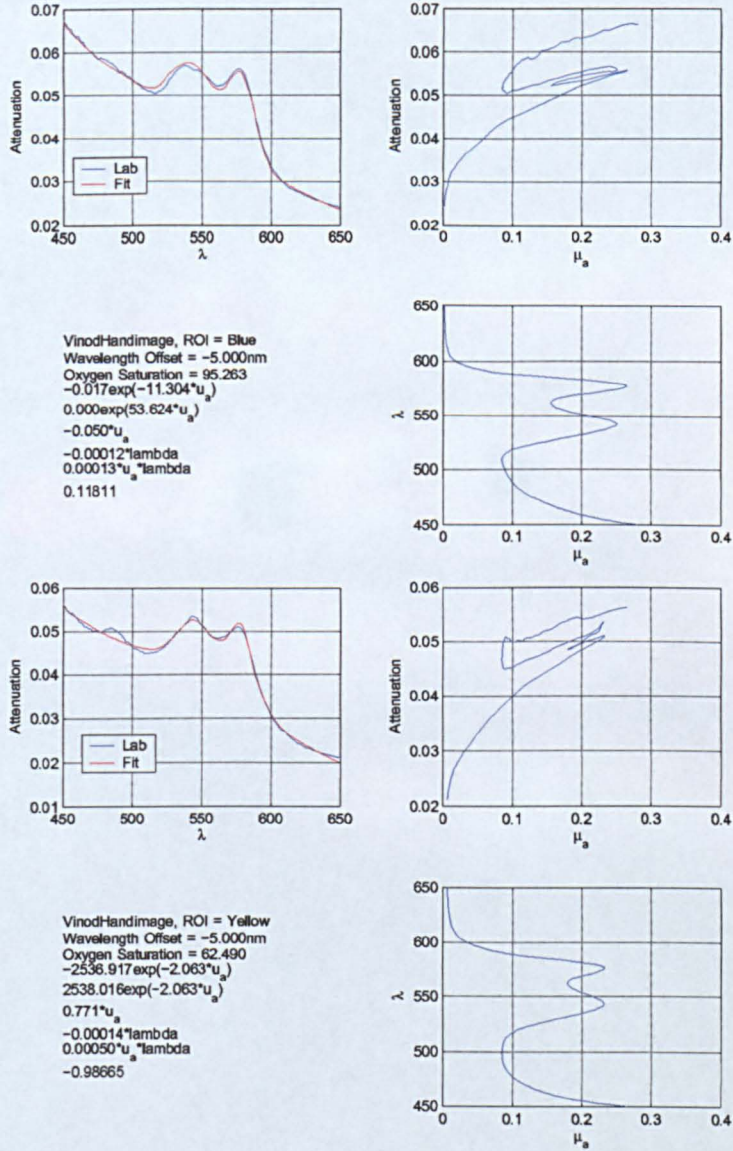


Figure 5.10: Analysis of Vinod’s regions of interest Blue and Yellow

Figure 5.11: Vinod’s hand image showing region of interest

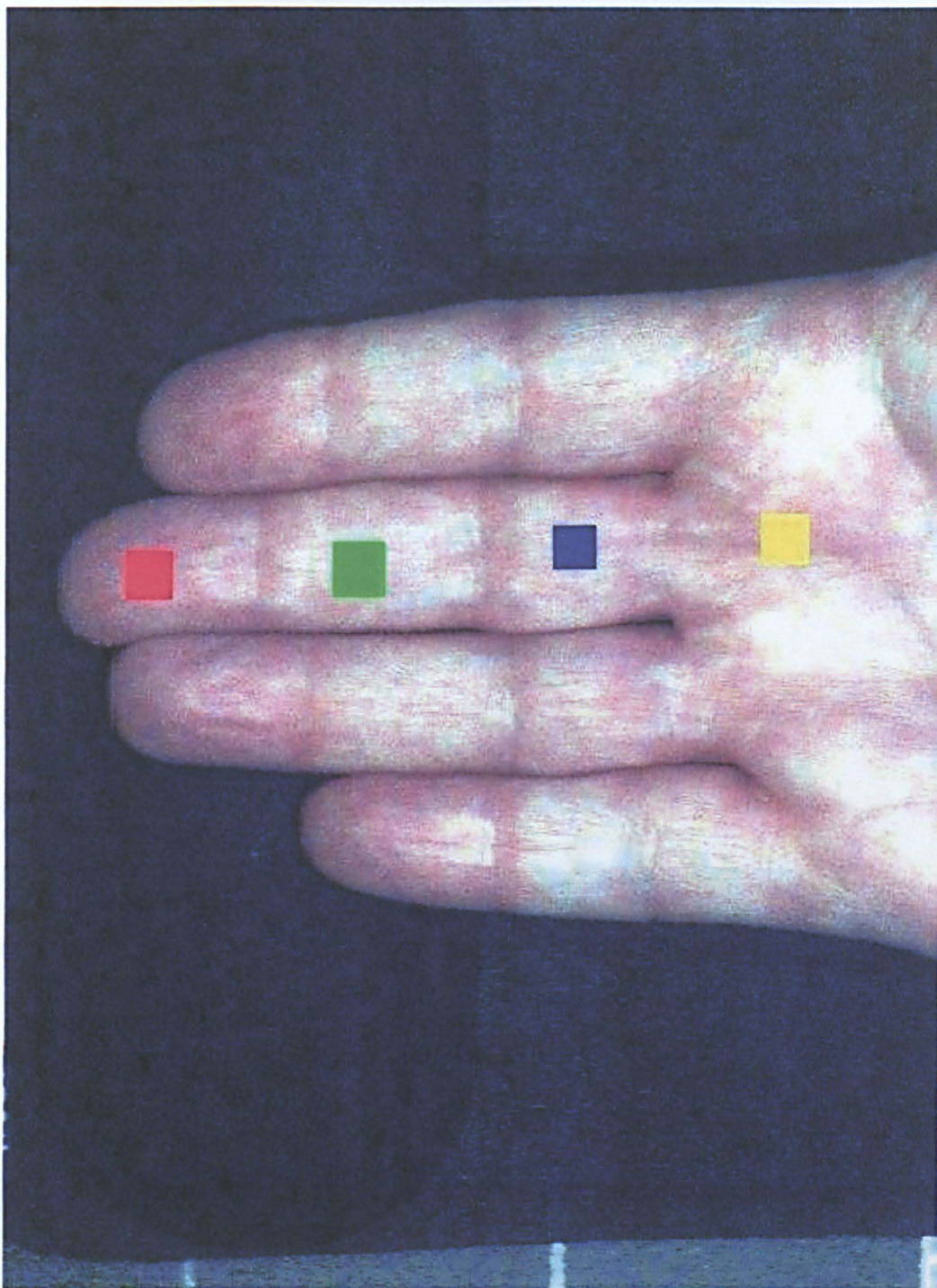


Figure 5.11: Paul's hand image showing regions of interest

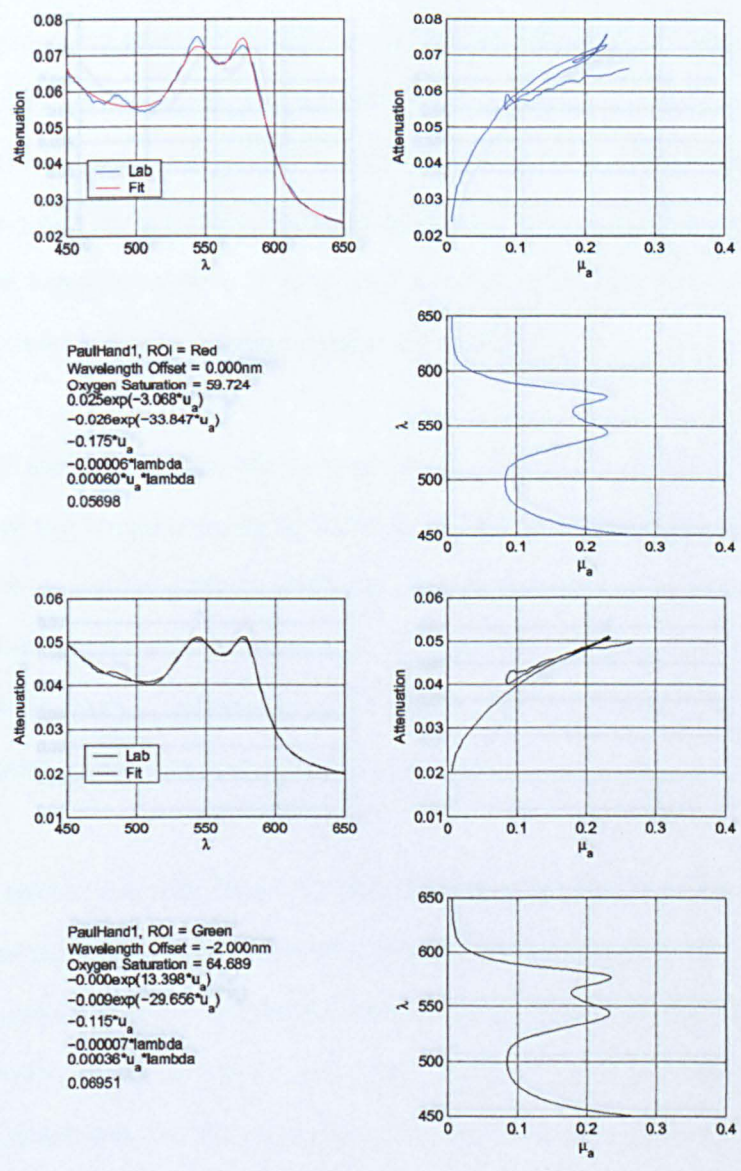


Figure 5.12: Analysis of Paul’s hand image regions of interest Red and Green

5.8.1 Results and Discussion

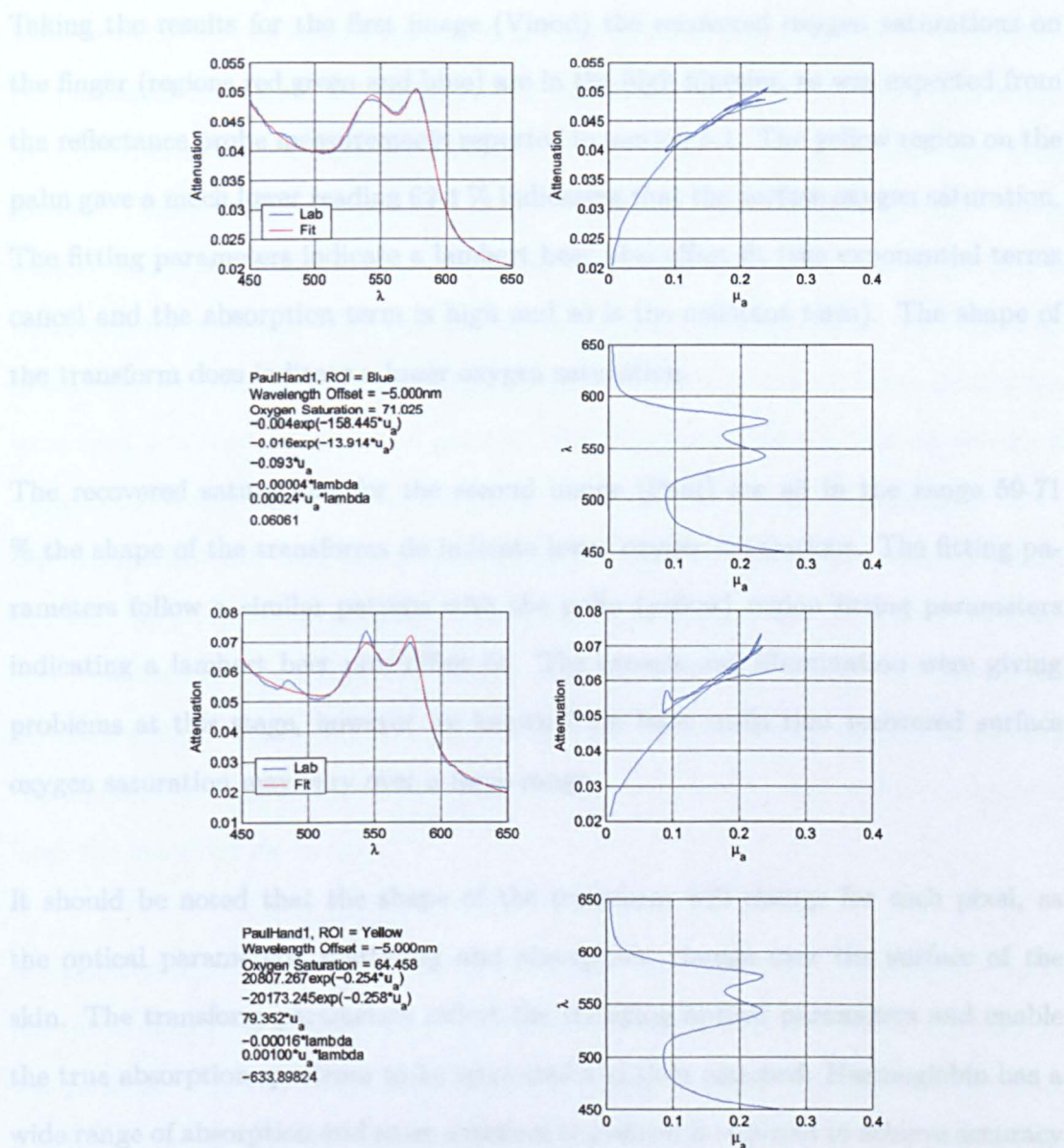


Figure 5.13: Analysis of Paul's hand image regions of interest Blue and Yellow

5.6.1 Results and Discussion

Taking the results for the first image (Vinod) the recovered oxygen saturations on the finger (regions red, green and blue) are in the high nineties, as was expected from the reflectance probe measurements reported in section 5.1. The yellow region on the palm gave a much lower reading 62.4 % indicating that the surface oxygen saturation. The fitting parameters indicate a Lambert Beer plus offset fit (the exponential terms cancel and the absorption term is high and so is the constant term). The shape of the transform does indicate a lower oxygen saturation.

The recovered saturations for the second image (Paul) are all in the range 59-71 % the shape of the transforms do indicate lower oxygen saturations. The fitting parameters follow a similar pattern with the palm (yellow) region fitting parameters indicating a Lambert Beer plus offset fit. The camera and illumination were giving problems at this stage, however we know from later trials that recovered surface oxygen saturation may vary over a large range.

It should be noted that the shape of the transform will change for each pixel, as the optical parameters, scattering and absorption, change over the surface of the skin. The transform parameters reflect the changing optical parameters and enable the true absorption spectrum to be recovered and then matched. Haemoglobin has a wide range of absorption and so an excellent transform is required to achieve accuracy of the wide range of scattering and absorption encountered.

5.7 Az Trial

The Provision camera's faults hardware and software were corrected by Provision and AstraZeneca setup a full scale trial to test the usefulness of oxygen saturation maps as a bio marker and to compare the results with laser doppler imaging. The Trial involved taking images at set time intervals (15 mins, 6, 24 and 48 hours). Each subject was injected with a pattern of uric acid crystals (fig 5.14) which produce a inflammatory response. The top site on each limb is injected with a 1.25 mg dose of uric acid crystals and treated with an anti-inflammatory cream, three treatments were used in a random and blind pattern. The four lower sites are used to provide a calibration or dose response curve (0,0.313,0.625,1.25 mg uric acid crystals).

The images, at each time point were taken first with a laser doppler system, which provides both doppler and monochrome images and the with the hyperspectral camera. Analysis of the hyperspectral images provided the image (figure 5.15) and oxygen saturation (figure 5.16). These were then compared with the laser doppler image and the planimetry (measuring the size of the response, which is assumed to be circular from the monochrome image).

It should be noted that this trial involved both arms and legs requiring the camera to be moved for each subject. This made it difficult to ensure that each image was in focus. The difficulty is due the the scanning nature of the provision camera, which can require a number of scans to correct the focus, hence the fuzzy appearance of image 5.15

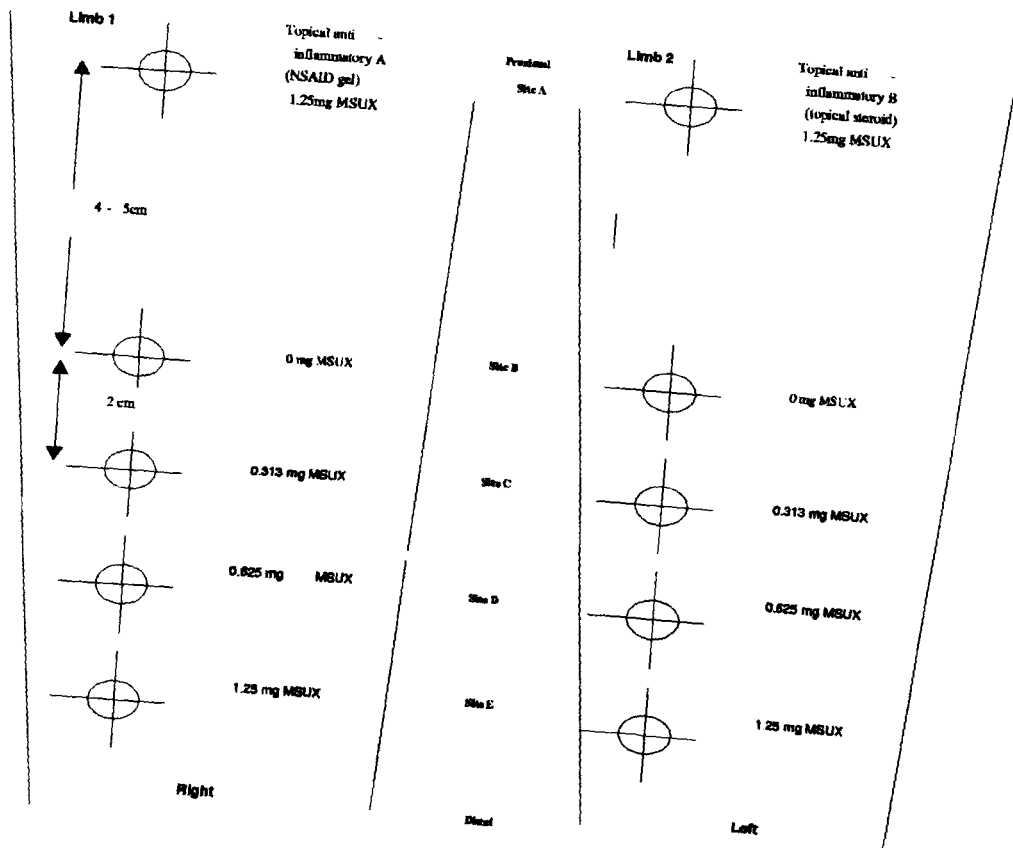


Figure 5.14: Trial Spec



Figure 5.15: Trial image subject 7 after 8 hours showing region of SO₂ Map

5.8 Results and Discussion

AstraZeneca are seeking a fast response to their new drug development pipeline to identify and quantify the response to different treatments. The use of the response measured by planimetry, is difficult to assess in a clinical trial. It provides an indication of the size of response, but it is difficult to compare between subjects. Laser doppler has been used to measure the response to different treatments in subjects.

Laser doppler has been used to measure the response to different treatments in subjects. It provides an indication of the size of response, but it is difficult to compare between subjects. Laser doppler has been used to measure the response to different treatments in subjects. It provides an indication of the size of response, but it is difficult to compare between subjects.

The SO_2 maps (Figure 5.16) show the response to different treatments in subjects. The SO_2 maps (Figure 5.16) show the response to different treatments in subjects. The SO_2 maps (Figure 5.16) show the response to different treatments in subjects. The SO_2 maps (Figure 5.16) show the response to different treatments in subjects.

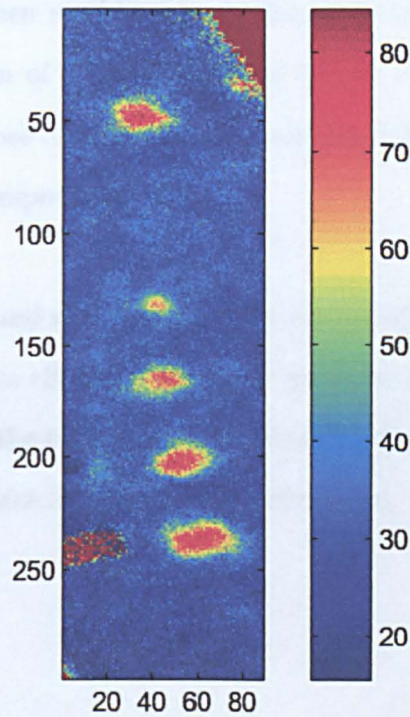


Figure 5.16: SO_2 Map of region of trial image subject 7 after 8 hours

5.8 Results and Discussion

AstraZeneca are seeking a fast reliable bio marker technology to enable them to identify and quantify the response to anti-inflammatory treatments. The size of the response measured by planimetry, is difficult to assess, subjective and while it provides an indication of the size of response it is difficult to quantify and compare between subjects. Laser doppler has been used for some time, it measures a mass, velocity product and gives an indication of the inflammatory response, but the scan time is long approximately 5 mins it dose differentiate the response sizes but the images contain other clutter such as the response of veins.

The SO_2 maps (figure 5.15), agreed well with the laser doppler images and were clearer and thought by the AstraZeneca clinical team to be superior to them. AstraZeneca are sufficiently impressed with the technique to continue funding development and to seek a partner in the development of a diagnostic instrument.

Chapter 6

Mathematics Underpinning the model

6.1 Introduction

This chapter looks at the mathematics which underpin the dual exponential model and extend the fitting equation to three and then four exponential terms. It also examines a series solution to the attenuation integral and compares this solution to the exponential fit.

6.2 Simplest case

The simplest model for $s(t)$ is an equal probability of detecting a photon at all path lengths up to a maximum t_2 , as shown in figure 6.1, this simplifies the Attenuation integral to equation 6.1.1.

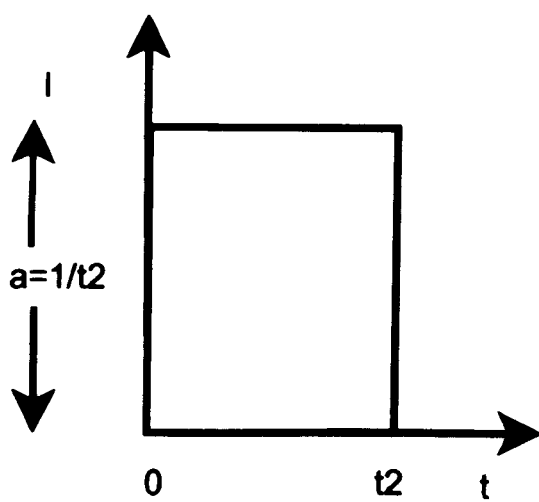


Figure 6.1: A simple unit Intensity TPSF

$$A = -\ln \left(\int_0^{t_2} \frac{e^{-\mu_a ct}}{t_2} dt \right) \quad (6.2.1)$$

$$A = -\ln \left(\frac{-1}{\mu_a ct_2} [e^{-\mu_a ct}]_0^{t_2} \right) \quad (6.2.2)$$

$$A = -\ln \left(\frac{1}{\mu_a ct_2} (1 - e^{-\mu_a ct_2}) \right) \quad (6.2.3)$$

$$A = \ln \mu_a ct_2 - \ln (1 - e^{-\mu_a ct_2}) \quad (6.2.4)$$

Expanding $\ln(1 - x)$

$$A = \ln \mu_a ct_2 + e^{-\mu_a ct_2} - \frac{e^{-2\mu_a ct_2}}{2} \dots \quad (6.2.5)$$

A fitting equation is formed from the first two exponential terms, these have a dependant relationship of one half, however this is relaxed to make their relationship independent. This modification allows the fitting algorithm to compensate for the higher order terms and the effects of scattering (shape of the TPSF), which is investigated in section 6.3.

$$A = ae^{b\mu_a} + a_2e^{b_2\mu_a} + c + d \ln \mu_a \quad (6.2.6)$$

Where the linear term introduced in chapter 4 is replaced by the log term $d \ln \mu_a$, this improves the accuracy of the fit, reducing the worst error by 20 % at low μ_a

values, this is due to the log term going to $-\infty$, eliminating the effect of the larger exponential terms and so increasing the freedom of the fitting equations.

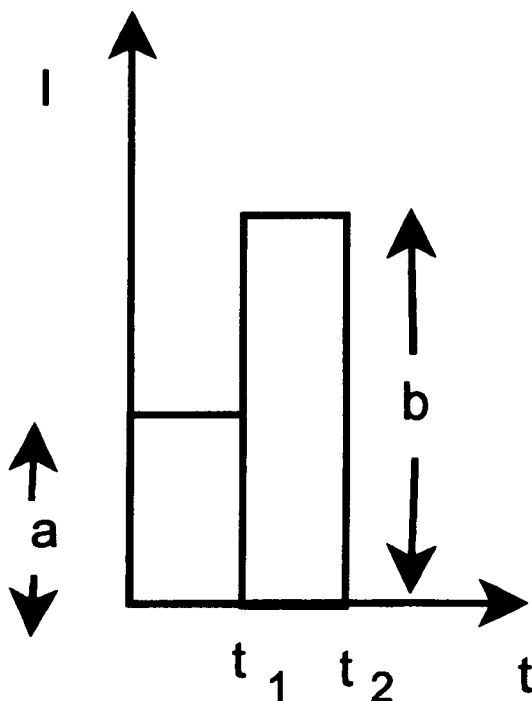


Figure 6.2: A TPSF composed of two blocks

6.3 The effect of the shape of the TPSF

The next case involves a TPSF with two intensities, as shown in figure 6.2, intensity (a) from $t = 0$ to $t = t_1$ and intensity (b) from $t = t_1$ to $t = t_2$. The Attenuation integral is then equation 6.3.1. We are using this case to examine the effect of the shape of the TPSF on the fitting equation.

$$A = -\ln \left(a \int_0^{t_1} e^{-\mu_a ct} dt + b \int_{t_1}^{t_2} e^{-\mu_a ct} dt \right) \quad (6.3.1)$$

$$A = -\ln \left(\frac{-1}{\mu_a c} (a - ae^{-\mu_a ct_1} + be^{-\mu_a ct_1} - be^{-\mu_a ct_2}) \right) \quad (6.3.2)$$

$$A = -\ln \left(\frac{-1}{\mu_a c} (a + (b - a)e^{-\mu_a ct_1} - be^{-\mu_a ct_2}) \right) \quad (6.3.3)$$

$$A = - \left[\ln \left(\frac{-a}{\mu_a c} \right) + \ln \left(1 + \frac{(b - a)}{a} e^{-\mu_a ct_1} - \frac{b}{a} e^{-\mu_a ct_2} \right) \right] \quad (6.3.4)$$

Expanding $\ln(1 + x)$

$$A = - \left[\ln \left(\frac{\mu_a c}{a} \right) + \frac{(b - a)}{a} e^{-\mu_a ct_1} - \frac{b}{a} e^{-\mu_a ct_2} \dots \right] \quad (6.3.5)$$

Equation 6.3.5 has the same form as equation 6.2.5 demonstrating that this exponential form is valid for the approximate TPSF shown in figure 6.2., all the figures in previous chapters used two exponentials as shown in 6.2.5 and 6.3.5. In section 6.4 the effect of including three and then four exponential terms is examined.

6.4 The accuracy of the fitting equation

The mathematics of multi-block TPSF's quickly becomes complicated, and so having demonstrated that the fitting equation does not change form with TPSF shape and that provided μ'_s is constant and photon extinction is ignored, the equation may be expected to fit a range of μ_a values, the accuracy may be tested using Monte Carlo data. Initially a fitting equation with two terms was used then this was increased to three and finally four terms.

figure 6.3 shows the error and fitting parameters for the two exponential term fit:-

$$A = ae^{-b\mu_a} + a_2e^{-b_2\mu_a} + c + d\log(\mu_a) \quad (6.4.1)$$

The maximum fitting error is approximately $\pm 0.05 \%$, this is just slightly less than the error for the fitting equation used in all the experimental work as shown in figure 4.4, the experimental fitting equation uses a linear coefficient for μ_a . Figure 6.3 also shows that the parameters change smoothly with μ'_s which is desirable for a stable fitting process.

Figure 6.4 shows the fitting error and parameters for a three exponential fitting equation the error has reduced to $\pm 0.015 \%$, however coefficient a_3 has a large spike at low μ'_s .

Figure 6.5 shows the fitting error and parameters for a four exponential fitting equation the error has reduced to $\pm 0.0015 \%$, however coefficients a_3 and a_4 have large spikes at low μ'_s , and some of the other coefficients do not change smoothly with μ'_s .

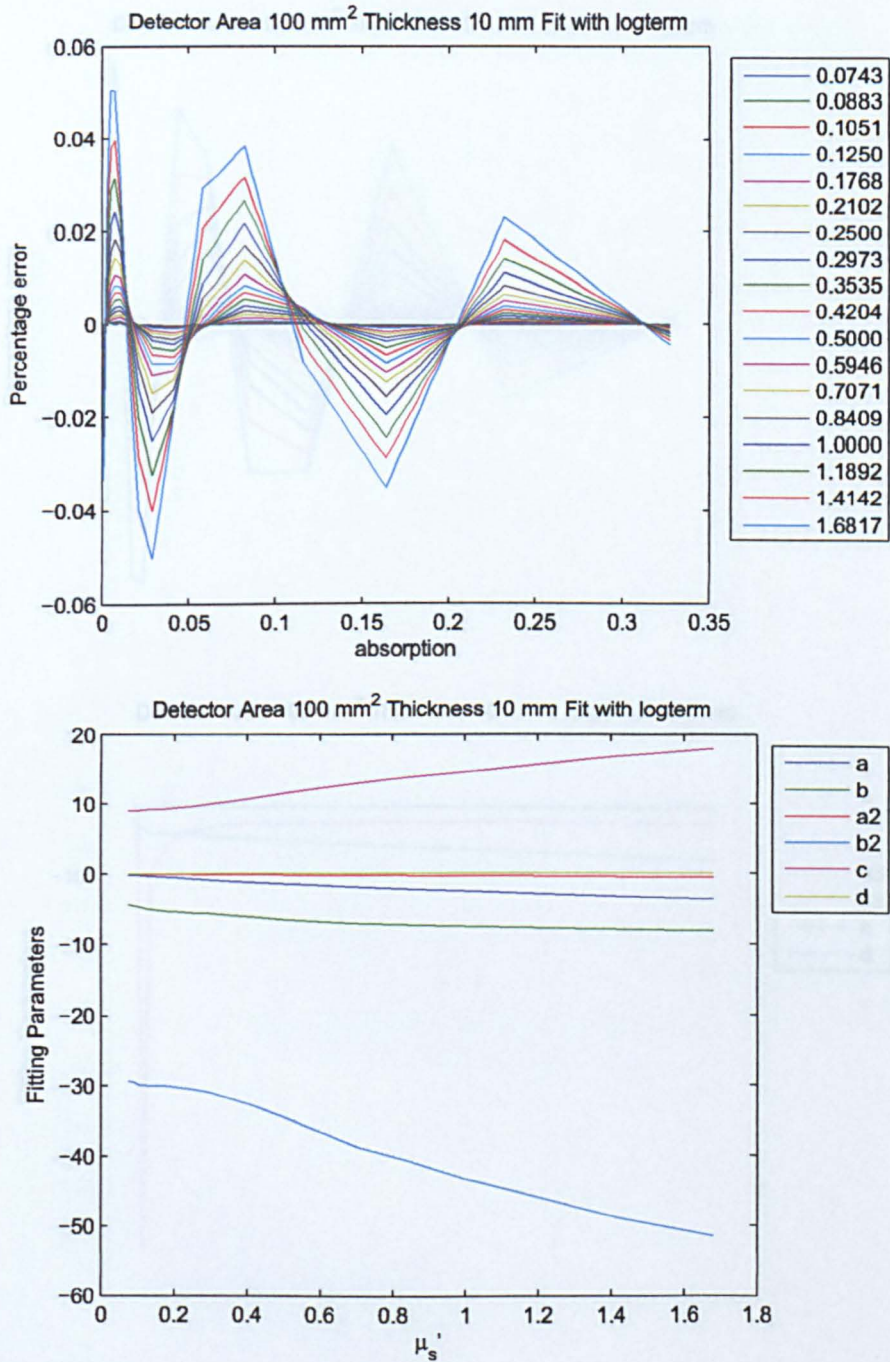


Figure 6.3: Error in fit with $A = ae^{-b\mu_a} + a_2e^{-b_2\mu_a} + c + d\log(\mu_a)$, over the absorption range μ_a 0 – 0.3 mm⁻¹ v scattering coefficient μ'_s 0.0743 – 1.6817 mm⁻¹

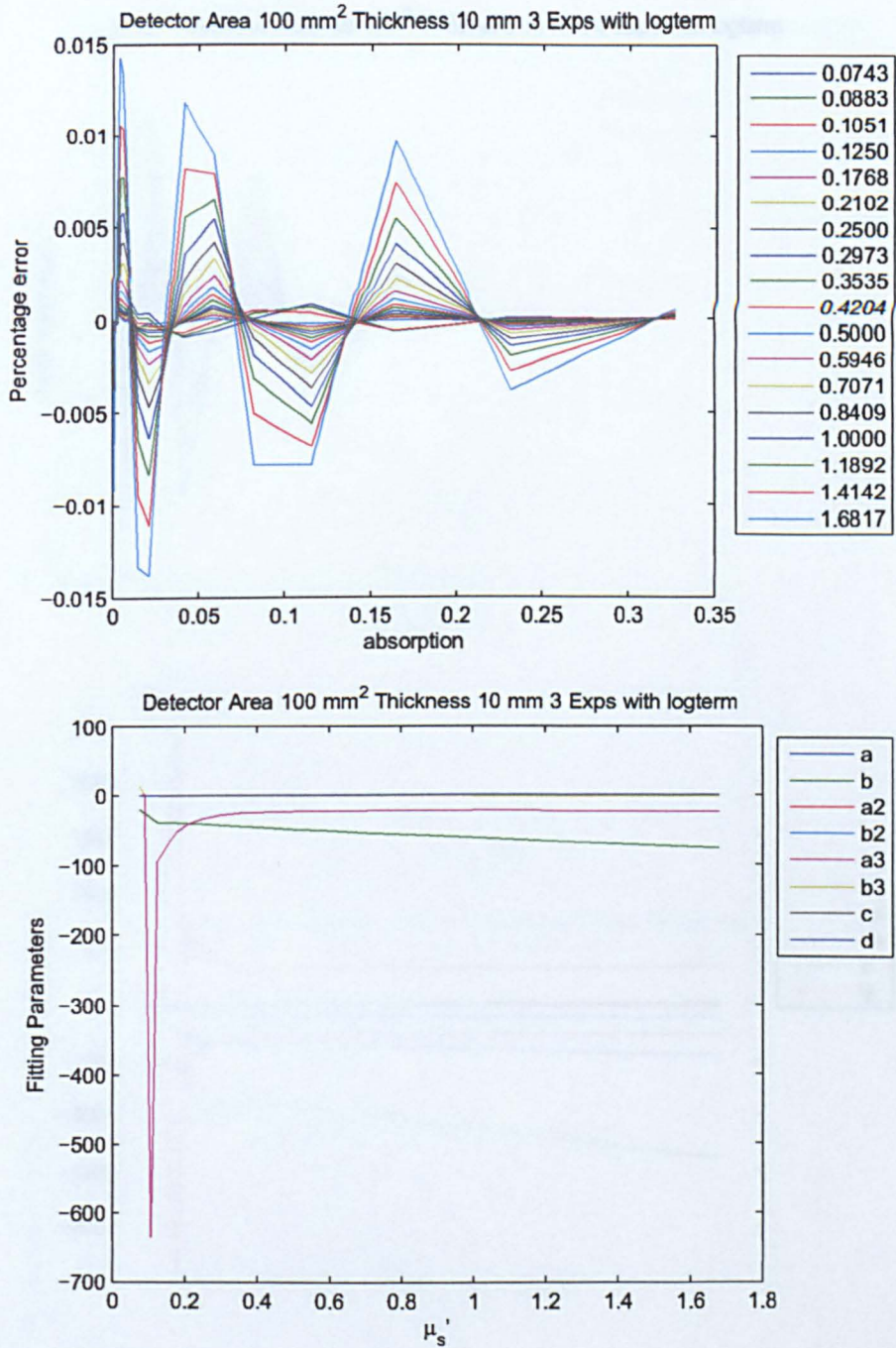


Figure 6.4: Error in fit with $A = ae^{-b\mu_a} + a_2e^{-b_2\mu_a} + a_3e^{-b_3\mu_a} + c + d\log(\mu_a)$, over the absorption range μ_a 0 – 0.3 mm⁻¹ v scattering coefficient μ_s 0.0743 – 1.6817 mm⁻¹

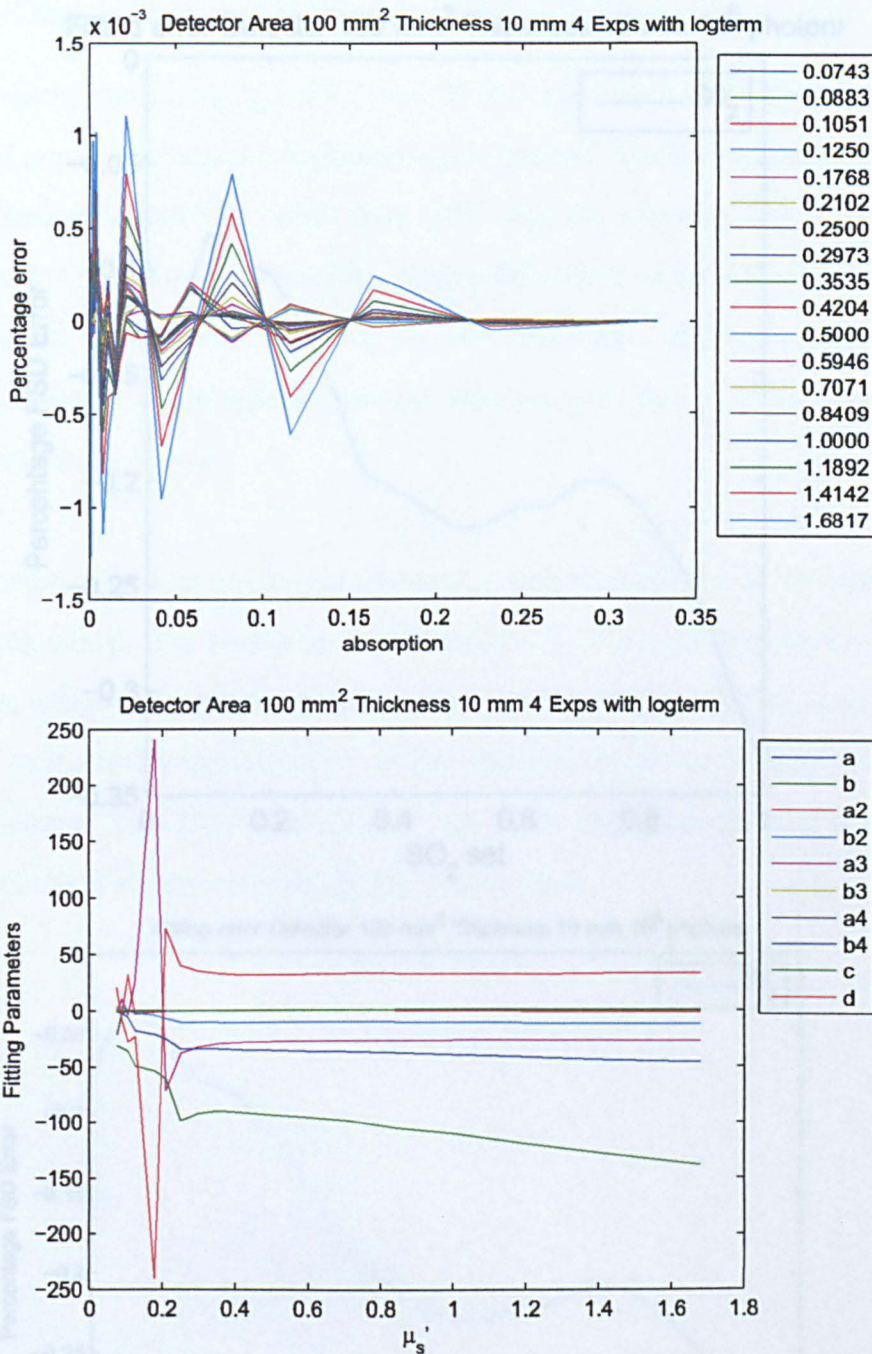


Figure 6.5: Error in fit with $A = ae^{-b\mu_a} + a_2e^{-b_2\mu_a} + a_3e^{-b_3\mu_a} + a_4e^{-b_4\mu_a} + c + d\log(\mu_a)$, over the absorption range μ_a 0 – 0.3 mm⁻¹ v scattering coefficient μ_s 0.0743 – 1.6817 mm⁻¹

Figure 6.5: Error in SO₂ with (a) $A = ae^{-b\mu_a} + a_2e^{-b_2\mu_a} + a_3e^{-b_3\mu_a} + a_4e^{-b_4\mu_a} + c + d\log(\mu_a)$ and (b) $A = ae^{-b\mu_a} + a_2e^{-b_2\mu_a} + a_3e^{-b_3\mu_a} + a_4e^{-b_4\mu_a} + c + d\log(\mu_a)$

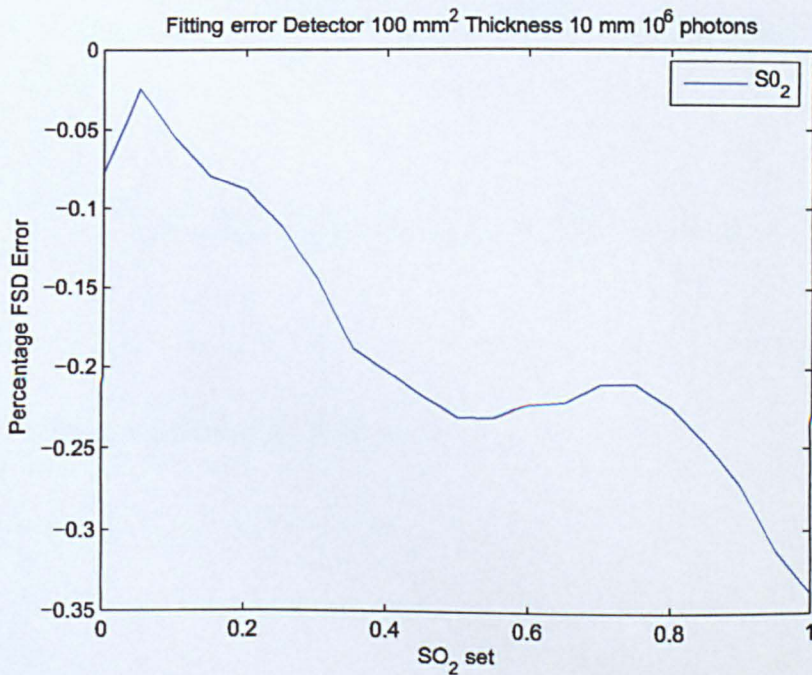
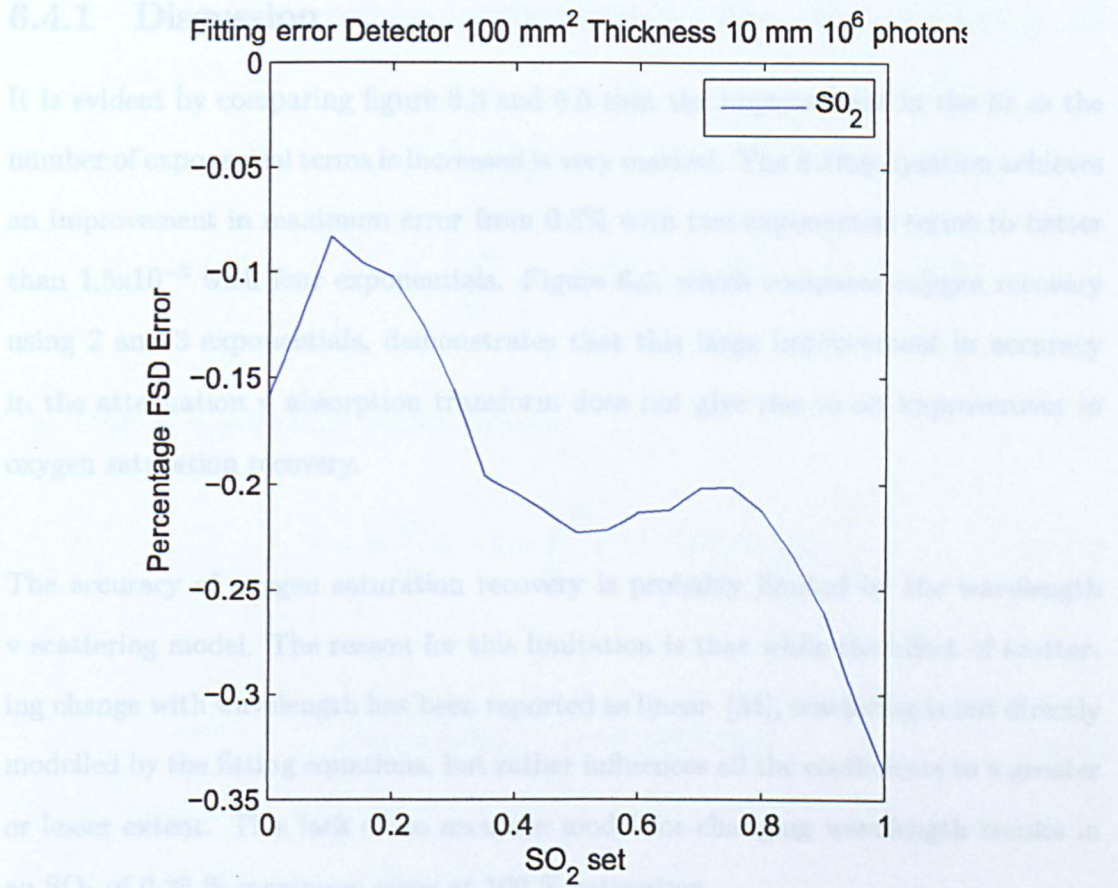


Figure 6.6: Error in SO_2 with (a) $A = ae^{-b_1\mu_a} + a_2e^{-b_2\mu_a} + c + d\log(\mu_a) + f(\lambda)$ and (b) $A = a_0e^{-b_1\mu_a} + a_1e^{-b_2\mu_a} + a_2e^{-b_3\mu_a} + c + d\log(\mu_a) + f(\lambda)$

6.4.1 Discussion

It is evident by comparing figure 6.3 and 6.5 that the improvement in the fit as the number of exponential terms is increased is very marked. The fitting equation achieves an improvement in maximum error from 0.8% with two exponential terms to better than 1.5×10^{-3} with four exponentials. Figure 6.6, which compares oxygen recovery using 2 and 3 exponentials, demonstrates that this large improvement in accuracy in the attenuation v absorption transform does not give rise to an improvement in oxygen saturation recovery.

The accuracy of oxygen saturation recovery is probably limited by the wavelength v scattering model. The reason for this limitation is that while the effect of scattering change with wavelength has been reported as linear [34], scattering is not directly modelled by the fitting equations, but rather influences all the coefficients to a greater or lesser extent. This lack of an accurate model for changing wavelength results in an SO₂ of 0.35 % maximum error at 100 % saturation.

6.5 An alternative approach to the dependency of A on μ_a

The Attenuation may also be defined from:

$$I = a \int_0^{\infty} e^{-\mu_a ct} \text{TPSF}(t) dt \quad (6.5.1)$$

The TPSF is a probability density function

$$A = \ln \frac{I_0}{I} = -\ln \left[a \int_0^{\infty} e^{-\mu_a ct} \text{TPSF}(t) dt \right] \quad (6.5.2)$$

$$A = \ln a - \ln \left[\int_0^{\infty} e^{-\mu_a ct} \text{TPSF}(t) dt \right] \quad (6.5.3)$$

$$A = \ln a - \ln \left[\int_0^{\infty} \left(1 - \mu_a ct + \frac{\mu_a^2 c^2 t^2}{2} - \dots \right) \text{TPSF}(t) dt \right] \quad (6.5.4)$$

$$A = \ln a - \ln \left[1 - \mu_a c \langle t \rangle + \frac{\mu_a^2 c^2}{2} \langle t \rangle^2 \dots \right] \quad (6.5.5)$$

Taking the Series expansion for $\ln(1+x)$

$$A = \ln a - \left[1 - \mu_a c \langle t \rangle + \frac{\mu_a^2 c^2}{2} \langle t^2 \rangle - \dots \right] \frac{(-\mu_a c \langle t \rangle + \mu_a^2 c^2 \langle t^2 \rangle)^2}{2} \dots \quad (6.5.6)$$

Gathering up the terms will provide a power series transform, as written in 6.5.7.

$$A = a_1 + a_2 \mu_a + a_3 \mu_a^2 + a_4 \mu_a^3 + a_5 \mu_a^4 \dots \quad (6.5.7)$$

6.5.1 Fitting the power series

Having derived this new form for the Attenuation v absorption transform, it is interesting to see how well it fits the Monte Carlo data. Taking the power series form fitting equation, the Monte Carlo data was with a 12 term power series (figure 6.7), here are first the 6 power terms of a twelve term fit.

$$A = 0.735 + 9.6 \mu_a - 1.9 \mu_a^2 + 6 \mu_a^3 - 14.2 \mu_a^4 + 20 \mu_a^5 - 13.9 \mu_a^6 \dots \quad (6.5.8)$$

Figure 6.7 compares the fit obtained with two exponentials to that obtained with a twelve term power series. The fits match in terms of maximum error however the power series performs better above $\mu_a > 1.0$, it is interesting to note that in the range of our model $\mu_a < 0.3$ it requires 12 terms to match the 2 exponential model.

An explanation as to why this is may be the case is illustrated in figure 6.8. The ratio of the terms calculated and plotted and with the exception of the ratio of the first and second terms the result was a constant, this means that the coefficients are not independent but dependant as would be expected if the terms were in fact an exponential series.

It should be noted that a twelve term power series will match a wide range of curves and consequentially does not make a good fitting equation.

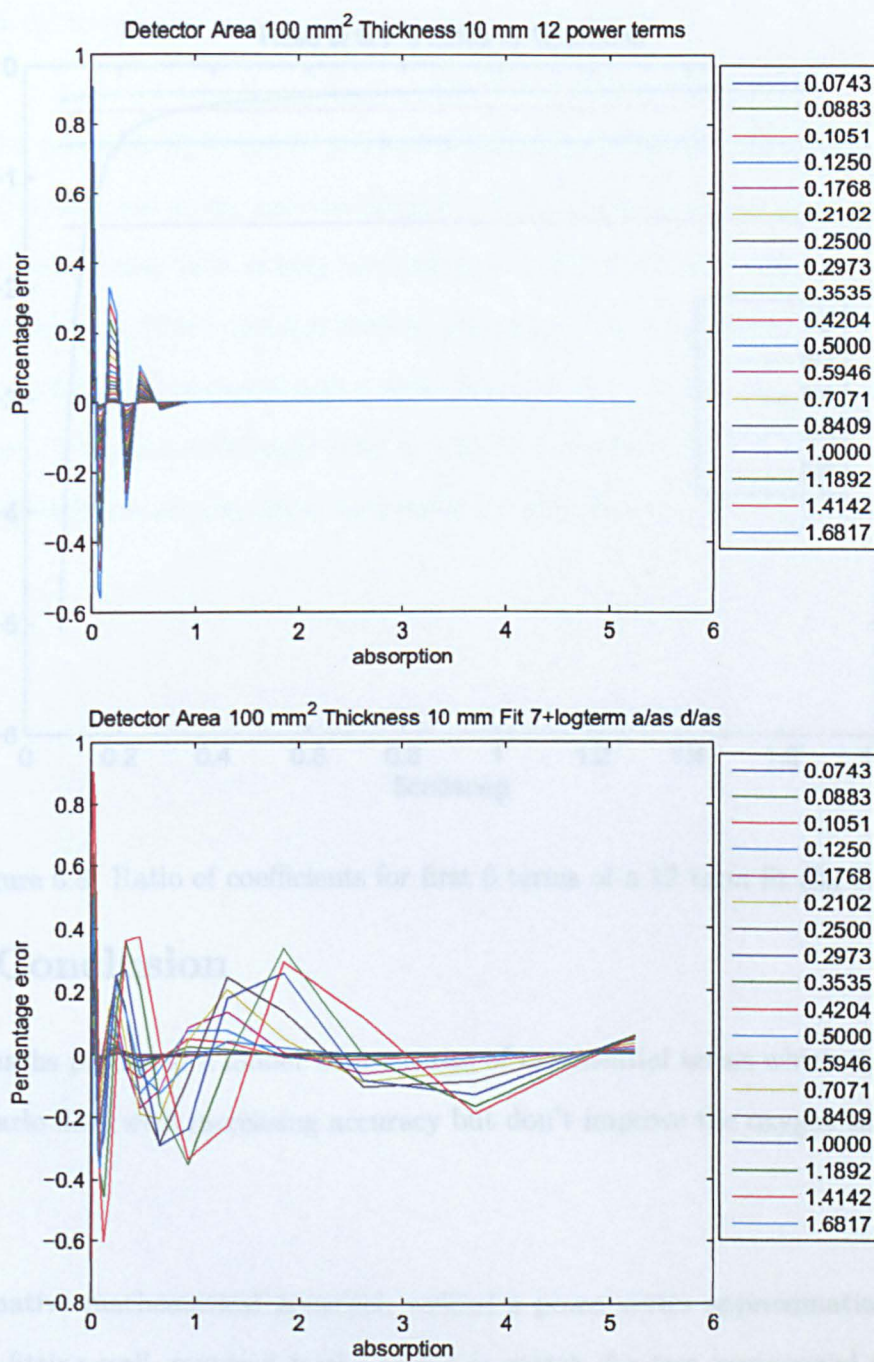


Figure 6.7: Error in fit with (a) 12 term series, and (b) $A = ae^{-b\mu_a} + a_2e^{-b_2\mu_a} + c + d\log(\mu_a)$, over the absorption range μ_a 0 – 0.3 mm^{-1} v scattering coefficient μ'_s 0.0743 – 1.6817 mm^{-1}

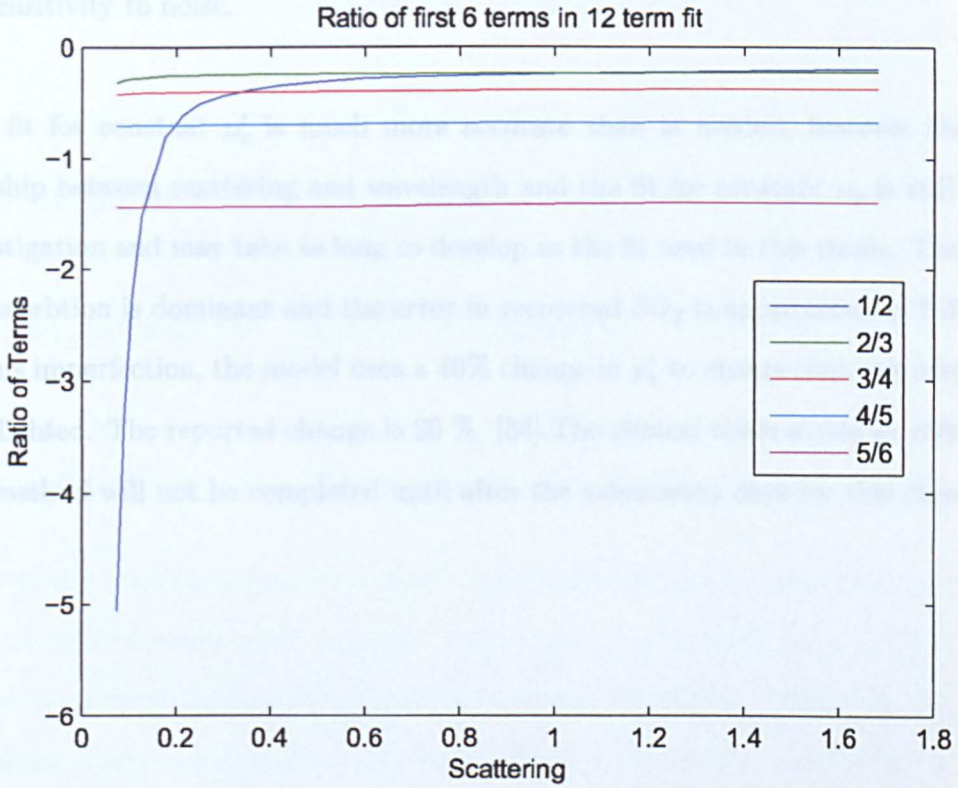


Figure 6.8: Ratio of coefficients for first 6 terms of a 12 term fit (fig 6.6)

6.6 Conclusion

Simple maths produced a model with a series of exponential terms which match the Monte Carlo data with increasing accuracy but don't improve the oxygen saturation recovery.

An alternative mathematical approach yielded a power series approximation which although fitting well, required twelve terms to match the two exponential term fit. The fitting equation was not used due to its flexibility, can match many curves, and

its sensitivity to noise.

The fit for constant μ'_s is much more accurate than is needed, however the relationship between scattering and wavelength and the fit for constant μ_a is still under investigation and may take as long to develop as the fit used in this thesis. The effect of absorption is dominant and the error in recovered SO_2 is approximately 0.4% due to this imperfection, the model uses a 40% change in μ'_s to ensure that any errors are highlighted. The reported change is 20 % [34]. The clinical trials aimed at validating the method will not be completed until after the submission date for this thesis.

Chapter 7

Discussion and Future Work

7.1 finding the Transform

Most of the work presented is involved with the modelling the scattering and absorption of light in media such as tissue. The object of this work being to develop an accurate mathematical equation to fit the Attenuation surface which may be plotted by Monte Carlo experiments. The scattering and absorption coefficients of tissue change with the coordinates examined at the microscopic scale and so this model is required to perform spectrophotometry and hence quantify the ratios of the leading chromophores, that is the various species of haemoglobin.

The work began with many Monte Carlo runs to plot an accurate surface model. The search for an equation (transform), led to the examination of the work of Lubbers and from there the approximations published by Kohl. Kohl's work provided a useful insight into the characteristics of the moments of the TPSF and helped develop an understanding of the transform which would be needed. The Kohl equations enabled the early spectrophotometry which determined the need for a more accurate transform. The results from the early work were within 2 % in ideal conditions using

modelled data, from here the search for a better transform began.

It was decided to search for a transform that would perform well over a wide range of scattering and absorption coefficients, this would enable the work to be applied to other scattering media with differing ranges of coefficients, this has yet to be investigated.

The transforms used in this thesis were developed by attempting to improve on the Kohl approximations by careful consideration of the form of the first four moments of the TPSF. This led to adding the ratio of the third and fourth moment to Kohl's approximation with an improved result. The noise inherent in the Monte Carlo data made this line of research difficult to follow but see chapter 6 for more information.

The theoretical research, the attempt to integrate the attenuation equation was proceeding in parallel and yielded the result in chapter 6.1 but no transform as yet. The transform used in all the experimental work (4.3.1) was found directly from consideration of the moments relationship with absorption and provided more accurate spectrophotometry with modelled data and in vivo data now that an accurate Spectrometer had become available.

The Ocean Optics USB200 Spectrometer and industrial quality reflectance probe enabled the early reflectance photometry which confirmed the method, but left a need for comparative studies to check the results. This work is planned and ethical approval is being sought. The trial will involve patients with low sats (low SO_2

readings) and healthy subjects and will compare the spectrophotometry with partial pressure and pulse oximetry.

The mathematical analysis finally bore fruit and the theoretical understanding of the transform is presented in Chapter 6, it can be seen that while slight improvements are possible from adding extra terms to the transform, it is at the price of considerable increases in complexity. The solutions presented in chapter 7 may enable an improved compensation for the scattering v wavelength factors and lead to a more uniform improvement in performance.

7.2 The Hyper-spectral Camera

This work is the result of an on-going collaboration with AstraZeneca Ltd. AstraZeneca had purchased a provision Hyper-spectral and were using it to determine whether haemoglobin could be used as a bio marker in trials using irritation assaults, on the arms and legs of healthy volunteers. They are very interested in this technique and, in turn we are interested in their work and the camera. The instrument (see chapter 5) enabled full spectrum images to be taken from arms and legs which we were able to produce oxygen saturation maps. The maps compare favorably with images taken using a laser doppler instrument.

7.3 Further Work

The validation of the oxygen saturation maps has proved a major challenge. Haemoglobin, if left exposed to the air becomes saturated with oxygen. So far a tissue phantom, in which we can set the oxygen saturation of a blood sample has not been discovered.

In collaboration with the Queens Medical center a trial is *been developed with first* healthy subjects and then subjects with low oxygen sats, some of these individuals routinely have sats of 80 % and some times as low as 70 %. The trial will compare, capillary blood samples, pulse oximeter data and hyperspatial images. Pulse oximeter provide an indication of core stats, but as these are measured at an extremity, care has to be taken to ensure that circulation has not shutdown at the extremity. The capillary blood samples give the best chance of validation, but are, of course single point data. To ensure an image of core oxygenated tissue a hyperspectral image of the underside of the tongue will be taken.

The transform could also be developed, not primarily, to increase accuracy but to enable the mapping of the changes in scattering coefficient. A long term objective would be to correct the measured attenuation for scattering to enable smaller concentrations of other absorbers to be identified.

The Hyper-spectral camera, requires a scanner to provide a complete image, this limits the frame rate to 90 seconds per frame. A lower resolution "Real Time" camera could be developed using a bundle of fibres to replace the scanner, the fibres would be arranged in a square at one end to capture an image but a line at the

other end to interface with the Inspector, this arrangement would enable an image to be taken in a few milliseconds. This new instrument could be used with microscope, endoscope or in reflection or transmission to study transient oxygen saturation.

The other field of opportunity is work with other haemoglobin species and other absorbers in different media, The food industry has a sustained interest in measuring levels of fats and other absorbers in their products. Agriculture is interested in sugar levels in fruit, to monitor ripeness and for quality control purposes. [46]

Bibliography

- [1] Demet G Talip A Nevzat U Serhat O Gazi O. The evaluation of cerebral oxygenation by oximetry in patients with ischaemic stroke. *Journal of Post Graduate Medicine*, 46:70–74, 2000.
- [2] Staniforth AD Kinnear WJ Starling R Cowley AJ. Nocturnal desaturation in patients with stable heart failure. *Heart*, 80:633–4, December 1998.
- [3] Hay WW Jr Thilo E Curlander JB. Pulse oximetry in neonatal medicine. *Clinical Perinatol*, 81:441–72, September 1991.
- [4] Scheufler O Exner K Andresen R. Investigation of tram flap oxygenation and perfusion by near-infrared reflection spectroscopy and color-coded duplex sonography. *Clinical Perinatol*, 113:141–155, January 2004.
- [5] Professor A.C. Brown. Respiration physiology: Blood gas transport: Oxygen transport. "www.acbrown.com".
- [6] G Dougherty N J Barnett and S J Pettingerg. A prototype instrument combining laser doppler flowmetry and reflection pulse oximetry. *Clin. Phys. Physiol. Meas.*, 13(2):105–114, 1992.
- [7] Fantini S Francheschini MA Maier JS and gratton E. Frequency-domain multi-source optical spectrometer and oximeter. *Procedures of the Society of Photo-Optical Instrumentation and Engineering*, 2326(4):108–1166, 1994.

- [8] Zijlstra WG. *Fundamentals and application of clinical oximetry, 2nd edition.* van Gorcum, Assen, 1953.
- [9] Nilsson NJ. Oximetry. *Physiol. Rev*, 490:1–26, 1960.
- [10] Yoshiya I and Shimada Y. *Non-invasive spectrophotometric monitoring of arterial oxygen saturation, In Non-invasive fetal and neonatal physiological measurements*, chapter 7. Academic Press, London, 1983.
- [11] Paula DeJohn. Legal, technology wars mark oximeter market. *Hospital Materials Management*, 27(7):1, July 2002.
- [12] Anonymous. Mississippi idn favors forehead sensors for more accurate pulse oximetry. *Hospital Materials Management*, 29(3):4, March 2004.
- [13] Nijland R Nierlich S Jongsma HW Nijhuis JG Oeseburg B Springer K Mannheimer P. Validation of reflectance pulse oximetry: An evaluation of a new sensor in piglets. *Journal of Clinical Monitoring*, 13(1):43–49, January 1997.
- [14] Webster JG (Ed.). *Design of Pulse Oximeters.* IoP Publishing, 1997. ISBN 07503 0467 7.
- [15] Anonymous. Pulse oximetry device under contract with amerinet promises more sensitive data. *Hospital Materials Management*, 25(35):7, May 2000.
- [16] C Dean Kurth and William S Thayer. A multiwavelength frequency-domain near-infrared cerebral oximeter. *Phys. Med. Biol.*, 44:727–740, 2004.
- [17] Nicolas Boalth a Jesper Wandrup b Lasse Larsson c Peter A Frischauf a Finn C Lundsgaard A Willy L Andersen A Niels-Henrik Jensen A Rolf Singer A Carl P Troldborg A Gitte Lunding. calibration-free new dry-chemistry and optical technology for near-patient testing. *Clinica Chimica Acta*, 307:225–233, 2001.

- [18] Thierry Guiberteau and Daniel Grucker. Dynamic nuclear polarization imaging in very low magnetic fields as a noninvasive technique for oximetry. *Journal Of Magnetic Resonance*, 124:263–266, October 1997.
- [19] Crowe JA and Damianou D. The wavelength dependence of the photoplethysmogram and its implication to pulse oximetry. *Proc. of the 14th Annual International Conference of the IEEE Engineering in Medicine and Biology Society*, pages 2423–2424, 1992. ISBN 0-7803-0785-2.
- [20] Mahajan A Lee E Callom-Moldovan A. Intraoperative use of forehead reflectance oximetry in pediatric patients. www.anestech.org/Publications/Annual2004/Mahjan.pdf.
- [21] M.G. Sowa J.R. Payette B. Abdulrauf M.F. Stranc Mansfield, J.R. and H.H. Mantsch. Tissue viability by multispectral near infrared imaging:a fuzzy c-means clustering analysis. *IEE Transactions Medical*, 6:1011–1018, 1998.
- [22] Lewis EN Levin IW. Zuzak KJ, Schaeberle MD. Visible reflectance hyperspectral imaging: characterization of a non-invasive, in vivo system for determining tissue perfusion. *Anal Chem*, 74.
- [23] William E. Charash M.D. Ph.D. 1 Noah A. Rosen, M.D. and M.D. Erwin F. Hirsch. Near-infrared spectrometric determination of blood ph. *Journal of Surgical Research*, 106:282–286, 2002.
- [24] Lubbers DW and Wodick. The examination of multicomponent systems in biological materials by means of a rapid scanning photometer. *Applied Optics*, 8:1055–1062, May 1969.

- [25] Lubbers DW and Wodick. *Oxygen measurements in biology and medicine Absolute reflection photometry applied to the measurement of capillary oxy-hamoglobin saturation of the skin in man*, chapter 7, pages 85–110. Payne and Hill, 1957.
- [26] Lubbers DW Hoffman J and Heise HM. Applicability of the kubelka-munk theory for the evaluation of reflectance spectra demonstrated for haemoglobin-free perfused heart tissue. *Phys. Med. Biol.*, 43:3571–3587, 1998.
- [27] Loyalka S K and Riggs C A. Invers problem in diffuse reflectance spectroscopy; accuracy of kulbelka-munk equations. *Applied Spectroscopy*, 49:1107–10, 1995.
- [28] Cope M Arridge, SR and DT Delpy. The theoretical basis for the determination of optical pathlengths in tissue. *Physics in Medicine and Biology*, 37.
- [29] Pittman RN and Duling BR. A new method for the measurement of percent oxyhemoglobin. *J. Appl. Phys.*, 38:315–320, 1975.
- [30] Patterson MS Chance B and Wilson BC. Time resolved reflectance and transmittance for non-invasive measurement of tissue optical properties. *Applied Optics*, 28(12):2331–2336, June 1989.
- [31] Kohl M Watson R and Cope M. Optical properties of highly scattering media determined from changes in attenuation, phase, and modulation depth. *Applied Optics*, 36(1):105–115, 1997.
- [32] Oregon Medical laser Clinic Extinction tables. www.omlc.ogi.edu.
- [33] Julie Bykowski George Zonios and Nikiforos Kollias. Skin melanin, hemoglobin, and light scattering properties can be quantitatively assessed in vivo using diffuse reflectance spectroscopy. *Am J Physiol Heart Circ Physiol*, 117:14521458, 2001.

- [34] Wai-Fung Cheong Scott A Prahl and Ashley J Welch. A review of the optical properties of biological tissues. *IEE Journal of Quantum Electronics* Volume 12 December, pages 2116–2185, 1990.
- [35] Lagarias JC JA Reeds MH Wright and PE Wright. Convergence properties of the nelder-mead simplex method in low dimensions. *SIAM Journal of Optimization*, 9:112–147, 1998.
- [36] Ocean Optics Ltd. <http://www.oceanoptics.com/products/usb2000.asp>.
- [37] Ultraspectral Inc. Hyperspectral Imaging for Environmental Intelligence. <http://www.ultraspectral.com>.
- [38] Surface Optics Corporation. <http://www.SurfaceOptics.com>.
- [39] Raymond E. Hanna. Long wavelength hyperspectral imaging applications. *Lockheed Martin Fairchild Systems*, <http://www.dtic.mil/ndia/night/Harra.pdf>.
- [40] Mark T. Gladwin Richard O. Cannon III Ira W Levin Karel J Zuzak, Michael D Schaeberle. Non-invasive determination of spatially resolved and time-resolved tissue perfusion in humans during nitric oxide inhibition and inhalation by use of a visible-reflectance hyperspectral imaging technique. *Journal of the American Heart Association*, 104:2905–2910, 2001.
- [41] E Neil Lewis Karel J Zuzak, Michael D Schaeberle and Ira W Levin. Visible reflectance hyperspectral imaging: Characterization of a noninvasive, in vivo system for determining tissue perfusion. *Anal. Chem.*, 74:2021–2028, 2002.
- [42] Richard O Cannon III Karel J Zuzak, Mark T Gladwin and Ira W Levin. Imaging hemoglobin oxygen saturation in sickle cell disease patients using noninvasive visible reflectance hyperspectral techniques: effects of nitric oxide. *Am J Physiol Heart Circ Physiol*, 285:1183–1189, 2003.

- [43] Institute for Technology Development. <http://www.pvtech.org>.
- [44] Specim Oy / Spectral Imaging ltd. <http://www.cri-inc.com/>.
- [45] Inc. CRI. <http://www.cri-inc.com/>.
- [46] the US Agricultural Research Service Lasers test the sweetness of fruit, Renfu Lu.
<http://optics.org/articles/news/11/5/23/1>.